DEMAND MODELLING OF HORIZONTAL ELECTRIC WATER HEATERS

Yu-Chieh (Jessie) Yen neé Liu
School of Electrical and Information Engineering
University of the Witwatersrand
Johannesburg

A thesis submitted to the Faculty of Engineering and the Built Environment, University of the Witwatersrand, Johannesburg, in fulfilment of the requirements for the degree of Doctor of Philosophy.

Johannesburg, 2021

Declaration

I declare that this thesis is my own, unaided work, other than where specifically acknowledged. It is being submitted for the degree of Doctor of Philosophy in the University of the Witwatersrand, Johannesburg. It has not been submitted before for any degree or examination in any other university.

Signed this 26 day of May 2021

Yu-Chieh Yen

Yu-Chieh (Jessie) Yen neé Liu
School of Electrical and Information Engineering
University of the Witwatersrand
Johannesburg

Acknowledgements

I would like to thank Prof. Ken J. Nixon and Prof. Willie A. Cronjé for their guidance and supervision throughout the duration of this work. Special thanks goes to Mr. Mark Goossens and his team for their assistance in the Genmin Laboratory at Wits University. Special thanks are also extended to my research collaborator, Prof Wei-Hua Ho for his counsel and enthusiasm for the work.

This work is based on the research supported in part by the following:

- Alstom Chair for Clean Energy Systems Technology (ACCEST),
- The National Research Foundation of South Africa (unique grant no: 98241), and
- The Department of Higher Education and Training (DHET).

I would also like to thank my colleagues and friends from the School of Electrical & Information Engineering and the greater Wits University community. I have gained so much in the conversations and counsel of such great companionship through my years at Wits; it has truly been a privilege.

I would also like to thank my friends and general support systems for their constant words of encouragement and overall moral support; and who remind me that there is indeed a life outside of this work.

Finally, thank you to my very supportive family who have given me all the opportunities to embark on this journey. A special word of thanks to my amazing husband, Yu-Ting (Tim) Yen, whose unwavering love, support, patience, and continued belief in my abilities has made this work possible. You are my rock.

Abstract

The thesis presented extends and contributes to research in demand-side management for the purpose of power utility planning and load forcasting applications and addresses the challenge of predicting the cumulative effects of Electric Water Heater (EWH) load due to transient heat recovery processes experienced by the thermal storage. Although previous work in this area has produced models that estimate water heating load through various abstractions of the thermal energy storage, there has not been an investigation into the transient response of the heat recovery process evident in the horizontal EWH typical to South African installations, which is computationally inexpensive for scaling to simulations with large populations. In the research presented, a multi-node model for a typical 150 ℓ, 3 kW EWH with 24 layers at fixed heights and variable volumes, and the mixing processes due to circular convection and inlet turbulence are modelled through different heat transfer coefficients affecting specified layers in relation to the element position. Measurement obtained over a range of draw scenarios (varying volumes and flow rates) are used to validate the multi-node model. Single-draw events are considered for ideal case validation and a double-draw event is considered to indicate a realistic usage profile. It is shown that the cumulative effects of the load profiles for a large range of population and demand intervals produce a predicted peak demand within 20%, time to peak of 5% and total energy within 15%. In addition, the multi-node model is shown to produce better peak demand predictions than a binodal model with a simple thermal abstraction.

This model and approach therefore represents a novel and valuable contribution to the development of load models for EWHs with transient characteristics, which enables low computational modelling of variable water heating load to produce a more accurate prediction of cumulative peak parameters for grid loading simulations.

Contents

List of Figures

List of Tables

Glossary

Binodal model Abstraction of a tank volume into two nodes with homogeneous temperatures in each node, which assumes perfect stratification (also known as ”two-node model”).

Hysteresis The switching of tank states based on different temperature paths.

Load aggregation Modelling technique of adding together of signals over a finite time frame to determine a total load (or power demand) at a specific instance in time.

Loadshedding Centrally controlled reduction of power supply to parts of the grid resulting in scheduled periods of no power to a region.

Multi-node model Abstraction of a tank volume into N nodes with homogeneous temperatures in each node, which allows for a temperature gradient for stratification.

One-node model Abstraction of a tank volume with one homogeneous temperature.

Primary replacement The element operation in ON state in response to a draw event.

Ripple control Direct control of EWH circuit from a centralised source. This is a switch upstream from the built-in thermostat.

Standing loss Energy losses to the ambient when no water is drawn from a thermal system (also referred to “standby loss”).

Steady-state The continuous heating and cooling of an EWH in the absence of a draw event, often characterised by a “saw-tooth” curve of the thermostat temperature.

Subsequent replacement The element operation(/s) in ON state following the primary replacement which occur before steady-state ON operations.

Thermal stratification The separation of regions in a body of water that results in a temperature gradient with higher temperatures at the top and colder temperatures at the bottom.

Thermocline The region of a thermally stratified body of water that has the greatest temperature gradient (or "mixing" of temperatures).

VC9006 Compulsory specification for hot water storage tanks for domestic use.

Acronyms

1D One-dimensional

2D Two-dimensional

3D Three-dimensional

ADMD After Diversity Maximum Demand

ASHRAE American Society of Heating, Refrigerating and Air-Conditioning Engineers

CFD Computational Fluid Dynamics

CHP Combined Heat and Power

DR Demand Response

DSM Demand-Side Management

EWH Electric Water Heater

HVAC Heating, Ventilation, and Air Conditioning

IDM Integrated Demand Management

MEPS Minimum Energy Performance Standard

NRCS National Regulator for Compulsory Specifications

RTD Resistance Temperature Detectors

SANS South Africa National Standard

SDG Sustainable Development Goals

TCL Thermally Controlled Load

TES Thermal Energy Storage

ToU Time of Use

TRNSYS Transient System Simulation Tool

UN United Nations

Chapter 1

Introduction

This chapter introduces the topic of this thesis, providing the argument and research question for the work. The layout of this document is also presented in terms of its chapters and appendices.

This thesis addresses the topic of demand modelling for a domestic thermally-controlled EWH in horizontal orientation and investigates the cumulative effects of the base model for load forecasting. This is important because horizontally-oriented EWHs produce transient element switching due to heat recovery, which commonly available load models do not capture. Current load models simplify the thermal storage abstraction, which result in a single element replacement event during heat recovery that is more suitable for modelling EWH in vertical orientation. This has implications on predicting power demand and Demand-Side Management (DSM) strategies for the grid in South Africa, where horizontally-oriented tanks are dominant.

EWHs are typically installed in the roof space of households where the horizontal orientation allows for easier piping structures and no additional supports are required. While the ratio of horizontal and vertical installations is largely unknown, it is estimated that the horizontal orientation could be as much as 95%. From an energy consumption perspective, Yen et al. (2017) show that the horizontal orientation is less energy efficient than the same tank in vertical orientation by approximately 33% during steady-state operation. This suggests that the consumer would save on electricity costs with a vertically-oriented tank.

From a power demand perspective, Yen et al. (2019) note that comparisons produced a maximum aggregated demand ratio (P_{aggrH}/P_{aggrV}) of 0.8 (for the same hot water service and a typical peak time interval of 4 hrs). In an extreme scenario, the maximum aggregated demand ratio of 0.58 was produced. This means that the vertical orientation produces a $24-70\%$ over-estimate of maximum demand than the horizontal. This suggests that load control strategies using currently available load models could over-estimate maximum demand in a population that is predominantly horizontal.

South Africa is a Paris Agreement signatory and has developed a National Development Plan that align with the United Nations (UN) Sustainable Development Goals (SDG) (SA National Planning Commission, 2020). Interventions including EWHs have been identified as a strategy toward reaching sustainable goals in the current South African energy regulation. The EWH is the largest electrical load in the domestic setting, accounting for approximately $33-50\%$ of energy consumption (Popoola and Burnier, 2014). It is estimated that there are 5.4 million EWHs in South Africa which accounts for 2 940 MW during peak loading (Eskom, 2013). If EWHs are to be used for load forecasting or DSM initiatives, appropriate load models for horizontally oriented EWH are required. To consider the cumulative effect of large populations, the model will also need to be computationally inexpensive. The multi-nodal approach to simulating the thermal storage is proposed for resolving the transient switching required for horizontal load models, which can be scaled for utility application.

Therefore, this thesis addresses the question of:

> *Can a multi-node model be used to predict element switching in a horizontally-oriented EWH post draw event to produce better peak demand predictions for system loading on a grid in comparison to load models with simpler abstractions?*

The following two objectives are derived from the question: (i) the horizontal load model should be able to predict the element switching due to draw replacement to resolve subsequent events observed in measurements due to the dynamic response for heat recovery, (ii) the predicted cumulative peak demand for the aggregated system should produce better performance than a binodal model (with a simplified thermal abstraction) developed for horizontal EWH.

Successful completion of this work will address the gap that exists for demand modelling of horizontally-oriented EWH with an element switching profile that adheres to the heat recovery cycle not addressed by energy-based models. This will provide confidence in modelling cumulative system effects such as peak demand predictions due to stochastic domestic hot water usage with variable draw parameters. It will also provide the required base model for the comparison of domestic water heating technologies for decision makers in formulating energy-related policy.

The scope of this work considers the EWH heating element operating normally through its built-in bimetallic thermostat control; no external control is applied to the unit, although control strategies are discussed in the context of DSM. Only a horizontally orientated EWH model is considered in this work. Any angle of orientation between 0° and 90° is not considered.

This thesis is structured as follows:

A **background** and brief literature survey is presented in *Chapter 2*. The contextualisation of thermal storage in sustainability goals is discussed. A brief overview of the South African utility scenario and the role for the EWH is provided for the local context. The EWH is discussed in more detail, in terms of its components, operation and thermal storage performance. Abstracted thermal models are discussed and how they are linked to load models with a final discussion on potential applications.

The **approach** in *Chapter 3* outlines the problem statement, highlighting the difference between horizontal and vertical element switching profiles. The parameters affecting this difference are investigated and discussed. The hypothesis for this work is presented with posited mechanisms. The roadmap for developing a horizontal EWH is discussed with all design decisions included for the experimental scenarios, and modelling strategy for the thermal abstraction and to determine aggregated system effects.

The **characterisation** of load profiles of draw events from an EWH is presented in *Chapter 4*. The steady-state durations of the element states are processed by using a probability density function to characterise the range of times in each state. Draw characteristics of durations in element states are determined by comparison with steady-state counterparts.

The horizontal EWH **model development** is presented in *Chapter 5*. This chapter details the calculation of thermal layers and the interaction of heat between the layers for each of the tank operating states. A set of parameters is presented and results are validated in the following chapter.

The simulated **results** are **validated** against experimental draw events in *Chapter 6*.

This chapter demonstrates the model performance of the element switching events through single-draw events and a double draw event. The efficacy of the model is discussed and analysed.

The impact of the model output is discussed in *Chapter 7* through **aggregation** techniques. The method is described and the resulting load profiles are discussed in terms of cumulative peak attributes (power demand and time to peak) and total system energy. The performance is compared to a load model with a simpler abstraction. The opportunities for DSM are discussed.

The findings and future work are summarised in *Chapter 8*. The thesis will be concluded by a final evaluation of the research objectives to reconcile the research question where a **concluding** statement will be made for this thesis.

Appendix A describes the **experimental setup** used, where the system design is discussed in terms of the testing platform and the EWH under test. The calibration of the temperature sensors used in the experiments is also presented.

Topics on **additional background theory** detailing hot water use and the thermal stratification effects of tank geometry are presented in *Appendix B*.

The **model design decisions** are described in more detail in *Appendix C*. This appendix explores the models produced by different number of layers, provides further details for the calculation of layer parameters.

Chapter 2

Background

The role of a Thermal Energy Storage (TES) as a strategic device for sustainability goals is discussed in *Section 2.2*. The EWH in the context of South African energy regulations and its participation on the electrical grid for demand-side management is discussed in *Section 2.3*. The EWH is discussed in *Section 2.4* in terms of its components and operational states. The abstraction of thermal storage and associated thermal stratification will be discussed in *Section 2.5*. Finally, applications of load models are presented in *Section 2.6*.

2.1 Introduction

Following from signing the Paris agreement 2015 for adoption of the UN Sustainable Development Goals (SDG), countries are setting zero emissions (or net zero) goals in a unified attempt to address climate change at policy level (Climate Change News, 2020). Countries that have implemented policies to reach net-zero goals by a declared year include Denmark (2050), France (2050), Hungary (2050), New Zealand (2050), Sweden (2045), United Kingdom (2050), Counties or districts with similar goals include California (2045) and Oxforshire (2030) (Oxfordshire County Council, 2019). Notably, South Africa has published a policy document detailing plans towards net zero by 2050 (SA Department of Environmental Affairs, 2020).

As the world moves towards the depletion of natural energy sources such as fossil fuels, there is a global interest in moving to more sustainable energy solutions (Schlör et al., 2012). This move towards sustainability has led to the development of renewables (such as wind, solar, photovoltaics) and better solutions in storage of energy (Hall, 2008). A summary of existing and predicted future energy storage technologies is presented by Baker (2008), which details electrical storage and Thermal Energy Storage (TES) used for Heating, Ventilation, and Air Conditioning (HVAC) applications. The domestic Electric Water Heater (EWH) is a widely distributed TES unit that occupies households countrywide, and therefore presents several opportunities for interventions towards sustainability goals.

This chapter contextualises the role of the TES discussed in *Section 2.2* and the EWH, towards sustainability efforts. Issues relating to the EWH and power grid in the South Africa are discussed in *Section 2.3* for local contextualisation. The EWH is presented in more detail in *Section 2.4* in terms of its components, operational and energy storage capabilities. The current body of research on thermal and load models are discussed *Section 2.5* and the extended application of these models is presented in *Section 2.6*.

2.2 Role of Thermal Storage Towards Sustainability

In the context of sustainability efforts and net-zero ambitions, thermal storage systems present attractive opportunities for optimising demand capacity on the grid (Vrettos et al., 2012). Thermal storage can realise passive savings through the designs of the systems (renewable or energy efficient sources for heat energy production), and can be used as a deferrable load; i.e. time of use can be asynchronous to its energy draw from the electrical grid. This presents an opportunity for control strategies for maximum demand reduction and time of use load-shifting.

Simple designs for thermal storage systems include a heating element and thermal insulation which reduces heat losses to the environment. Developments in thermal storage to realise passive gains exist in the development of TES media and cool storage media (Hasnain, 1998a,b), and the use of renewable resources (Hohne et al., 2019). Solar thermal developments have provided the ability for heat production through solar radiation using collector arrays or cathode tubes with the option for auxiliary electrical element back-up to top up heat for cloudy days. Developments in heat pump systems allow for electrically-connected water heaters to achieve high heat gains. Both these technologies have the potential to reduce the electrical burden on the grid for hot water production.

Utility-level control on grid-connected loads has great potential in demand-side management or demand response strategies (Boivin, 1995). This allows utilities to prevent deferrable loads (such as water heaters) from using energy during periods that the grid experiences insufficient supply and instead defer or shift the load to off-peak periods. The ability to control deferrable loads can also be used to reduce maximum demand, which would benefit the utility from delayed cost augmentation to the grid. This also presents opportunities for any excess supply produced by renewables, where excess power can be absorbed by responding deferrable loads. The consumer could benefit from these schemes with time-of-use tariff incentives.

Ericson (2009) demonstrate the deployment of a load control strategy on 475 households in Norway for water heaters rated at 2 kW. It is shown that an average consumption reduction of 0.5 kWh/h per household during controlled periods was achieved with a payback effect in the following hour of up to 0.28 kWh/h. Beute and Delport (2006) determined that the After Diversity Maximum Demand (ADMD) of controllable load due to water heaters of $0.2 - 1.3\,kW$ per water heater, considered at a South African municipality-level.

The managed loads at demand-side include the use of intelligent controls or "smart" capabilities. Consumer-side feedback systems are an important component to the success of demand-side interventions (Hargreaves et al., 2010, 2013). Ericson (2009) stresses that successful implementation of intelligent devices requires national standards and best practises to be followed for enabling the interworking and compatibility of systems.

2.3 The South African Context

The energy usage for domestic hot water service in South Africa accounts for approximately $33 - 50\%$ of household energy consumption, which is approximately 7% of national demand (Hohne et al., 2019, Popoola and Burnier, 2014). According to StatsSA (2016), there is an estimated total of 16.9 million households in South Africa (p. 55), where 4.7 million households claimed ownership of a EWHs under household goods (p. 81). It is not uncommon for households to have multiple EWHs, so the total number of EWHs participating on the grid is estimated to be larger than 4.7 million, and this is in line with the 5.4 million reported by Eskom (2013). Domestic water heaters in South Africa are primarily electric-element storage tanks.

South Africa has set a National Development Plan with goals that align with global efforts to towards sustainable development (SA National Planning Commission, 2020). In an effort to achieve national passive energy savings in the domestic water heating sector, the National Regulator for Compulsory Specifications (NRCS) enacted a regulation in 2016 through VC 9006 for Minimum Energy Performance Standard (MEPS) for domestic water heaters. An allowable standing loss of 1.38 kWh/day (Class B insulation level) was changed from previous unregulated designs with typical standing loss of 2.59 kWh/day. This is expected to realise 3.82 TWh of savings by 2030 (McNeil et al., 2014). The implementation of the regulation also had the effect of widespread non-compliance and served as a market disadvantage the solar thermal designs, which needed to comply with the same Class B regulation, despite the majority of heat energy supplied by renewable solar (Terblanche, 2018). Detailed in the net zero plan, solar water heating has been identified as a goal for five million units deployed by 2030 (SA Department of Environmental Affairs, 2020).

The implementation of MEPS using the available South Africa National Standard (SANS) 151 test procedures presented the limitation of using standing heat loss tests for energy regulation, which was uniformly applied to storage tanks with any electrical element utilisation. The use of the standing loss test, was deemed to be an insufficient metric for overall energy use (Lutz and Yen, 2020). The enactment of Class B on electric element water heaters is a significant step to achieving passive savings in the domestic water heating sector. However, more work needs to be done in convincing standards working groups and regulators of the energy gains achieved in solar thermal systems (with auxiliary element) and heat pump connected systems.

The opportunities for demand-side management is considered in the context of the status of the power grid. Between 1990 to 2007, grid expansion policies led to the wide-spread electrification of 5 million households (Bekker et al., 2008). The growth in electrification resulted in the growth of appliance ownership and increasing electrical demand (Forlee, 1996). Two new coal-fired power stations (Kusile and Medupi) were commissioned in 2007 to increase supply, with an expected capacity of 4 800 MW each.

The utility implemented a loadshedding strategy to address supply issues in 2008 (Eskom, 2020). Loadshedding involves the turning off large regions affecting residential, commercial and industrial loads on a rotational pre-defined schedule. The stages of severity were catergorised as Stage 1, Stage 2 and Stage 3, which represents a required load of 1 000 MW, 2 000 MW and 3 000 MW respectively to be shed.

Loadshedding was re-implemented intermittently in the next decade with an increased severity in the first quarter of 2019. Factors that influenced the inability to supply power to meet demand included, increase in utility debt, incomplete Kusile and Medupi builds, lost capacity from the Cahora Bassa line in Mozambique due to hazardous weather and political unrest caused by plans to split the utility. The severity increased with Stage 4 added to the schedule, requiring 4 000 MW to be shed from the grid. The highest severity implemented was Stage 6, which occurred in December 2019.

Eskom (2013) estimates that there are approximately 5.4 million EWHs in operation in South Africa, which have an estimated contribution of 2 940 MW to the evening peak load on the grid. This correlates to the load required to shed for Stage 3, indicating there is good opportunity for DSM initiatives around EWHs.

South Africa has implemented ripple control on water heaters since the 1950's (Beute and Delport, 2006). From 2006, additional methods such as radio and power line communication were expected to be implemented for load control and control systems with two-way communication were considered to include tampering notifications and state-of-charge for water heaters. Ripple control remains the dominant EWH load control mechanism used by the utility through the Integrated Demand Management (IDM) division, and it remains a volunteer programme for end-users. The programme is met with mixed success; many sources report bridged or tampered relays that are no longer in operation, while some municipalities report a system that remains functional and intact (Kempton Express, 2013).

The Johannesburg utility, City Power, reported that ripple control enables up to 100 MW of capacity, which has assisted during periods of loadshedding (BusinessTech, 2020). They report the deployment of 40,000 additional units, which is expected to further aid with reducing peak power demand. They also report a 70 MW capacity for load-limiting through smart meters, which automatically turns off a household if a power threshold is reached. The long term load-limiting capacity is expected for 775 MW through the deployment of 330,000 smart meters.

According to ee Publishers (2015), City Power introduced Time of Use (ToU) tariffs for domestic consumers which integrate with the deployment of smart meters. This presents the enabling environment to incentivise consumers to own devices or controllers that allow for cost-saving use of their deferrable loads. Refer to *Appendix B.2.5* for a further discussion on ToU tariffs.

Other hot-water service devices such as solar water heaters, gas water heaters and heat pumps are not considered in this work. The use of these other devices are considered more expensive (upfront cost) and small market share in South Africa (McNeil et al., 2014). According to StatsSA (2016), there are 354 594 households that are using solar systems as energy sources, which is approximately 2.5% of the total households (p. 79). These technologies are also mostly independent (or use significantly less energy) from the electric grid, and therefore are out of scope for this work.

To attempt to meet sustainability goals and reach ambitions of correctly utilising thermal storage units as flexible, deferrable loads, there is a need to have a model that can reliably predict the cumulative demand requirements from TES for grid-related strategies. The majority of South African domestic water heaters are supplied by EWH. There is a need for a model that will provide policy makers, regulators and standards bodies with TES models that can assist in decision-making processes and to reliably implement changes that can realise national and sustainable deveolopment goals.

2.4 The Electric Water Heater

An EWH is a service device that supplies a user with hot water, has an electrical element as a heat source and includes a storage tank; it is otherwise known as a "geyser" in South Africa. The term "geyser" is often used for any hot water service device, which usually refers to electric water heaters, but could also be used to describe solar water heaters, i.e. "solar geyser".

The EWH is made of several key components: tank vessel (made up of an inner and outer casing with built-in insulation), inlet and outlet ports, an element (a heat exchanger in the form of an electrically-connected element coil), a flow diffuser, a thermostat and a thermoprobe, as shown in *Figure 2.1.*

A major factor affecting the thermostat control inside an EWH tank is the position of the element in relation to the internal thermodynamics of the water, as discussed by Delport (2005). Another influencing factor may be the position of the thermoprobe in relation to the element. Many South African EWH tanks are designed with a dual-mounted feature (either horizontally or vertically).

In the following subsections, the operational states of the EWH are discussed in

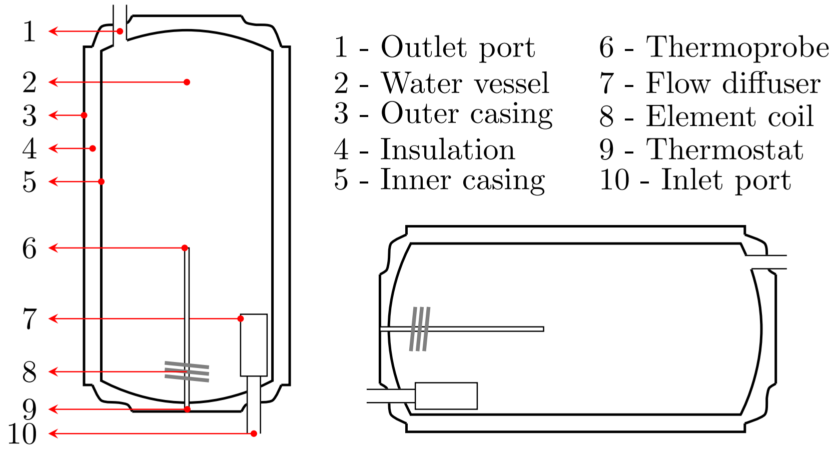

Figure 2.1: Schematic of the EWH tank in vertical orientation (left) and horizontal orientation (right).

Section 2.4.1. The thermal performance of the EWH as an energy storage device is discussed in the form of thermal stratification in *Section 2.4.2* and standing losses in *Section 2.4.3*. Finally, consumer-end hot water use is discussed in *Section 2.4.4*.

2.4.1 Operational States

An EWH is a Thermally Controlled Load (TCL) which means that the tank temperature is maintained around a hysteresis set-point controlled by a bi-metallic strip. The thermostatically-controlled states of a typical EWH (with no transient features) are shown in *Figure 2.2*.

In the absence of a draw event ($q = 0$) the EWH will enter into steady-state operation where the tank is maintained around its hysteresis. This is characterised by a “saw-tooth” curve. If the tank is in heating mode, H, the element is in ON state ($P = P_E$) then the temperature at the thermostat, T_t, increases. As the temperature reaches the upper hysteresis limit, T_{hystU}, the element switches to OFF state ($P = 0$) and the tank enters cooling mode, C. As the temperature reaches the lower hysteresis limit, T_{hystL}, the element switches to ON state ($P = P_E$) and the tank enters heating mode, H, again to restart the cycle.

A draw event can occur at any time during steady-state operation. Illustrated in *Figure 2.2*, a draw event is initiated as the temperature reaches the upper limit and transitions into cooling mode. As water is drawn from the tank ($q = q_{fixed}$), the temperature reduces rapidly. As the temperature passes the lower hysteresis limit,

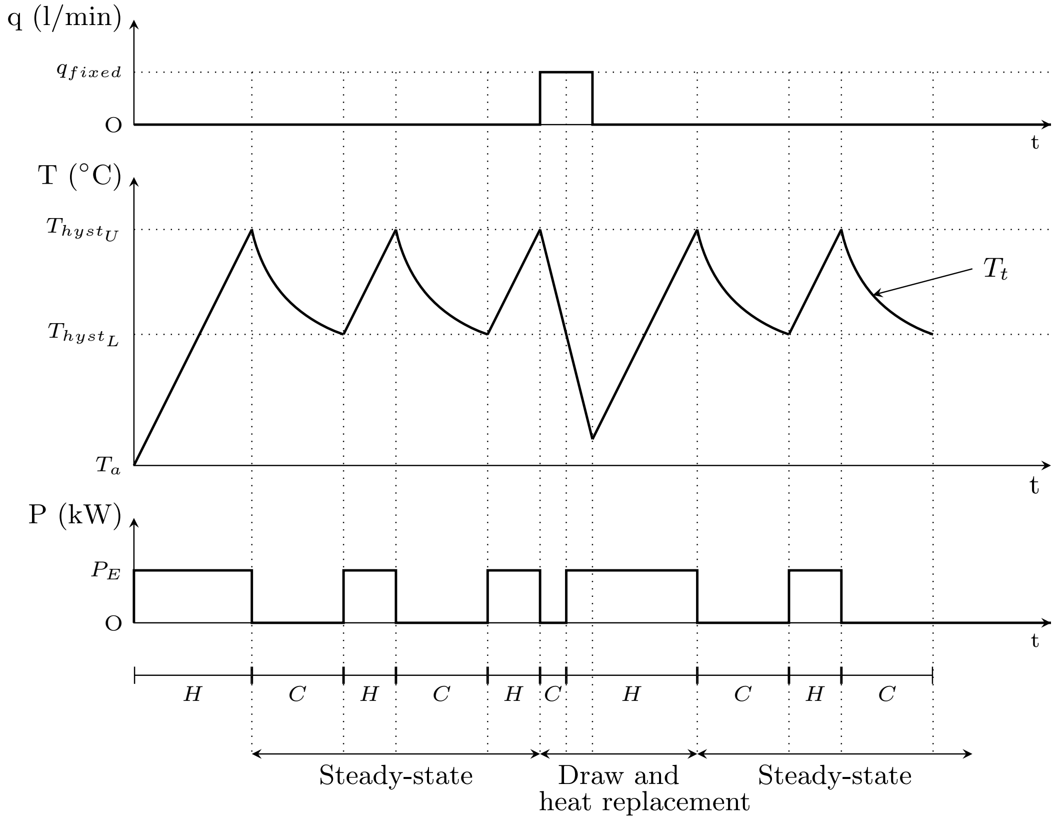

Figure 2.2: EWH states based on a single sensor temperature measurement at the thermostat, T_t, and subsequent element operation for heat recovery represented by P_E.

the element switches to ON state and the tank enters heating mode. However, the temperature only starts to increase when the draw event ends ($q = 0$).

When the element switches to ON state to replace heat drawn from the tank, this results in load demand that contributes to the electric grid. Since the element has a fixed power rating, the amount of time the element operates defines the replacement energy to the system. Steady-state energy replacement events usually operate for short periods of time (in the range of minutes) and are separated by long periods (in the range of hours), depending on the thermal insulation of the system and the ambient temperature. The duration of draw event energy replacements can vary (as will be shown later, depending on tank orientation), but are usually longer than steady-state events.

2.4.2 Thermal Stratification

Thermal stratification occurs in a water volume when hot water is drawn and cold water refills the tank in a constant volume system. This stratification is the separation of temperature regions in the tank resulting in a gradient of temperatures where there are colder regions at the bottom and hotter regions at the top. The mixed temperature gradient is known as the thermocline. This separation occurs because of buoyancy effects. Tanks that have a diffuser (or baffle) control the water flow from the inlet to reduce turbulence and mixing to ensure a small thermocline, thus keeping the hot regions closer to the set temperature. According to American Society of Heating, Refrigerating and Air-Conditioning Engineers (ASHRAE), it is estimated that most tanks have usable hot water extraction of 60% to 80% before cold water dilution (mixing from the thermocline) (ASHRAE, 2003). Better designs may exceed 90% hot water extraction. The useful energy from the system is known as exergy.

In the case when a partial volume draw takes place, the thermocline will appear along the height of the tank. If the temperature gradient is fairly constant along all sides of the tank, the Three-dimensional (3D) geometry of the tank volume could be abstracted to a One-dimensional (1D) model. The temperature gradient represents the temperature of regions of water in the tank at respective heights. Young and Baughn (1981) studied the temperature gradient of a tank in horizontal orientation with measurements along the length of the tank and concluded that the gradients along the length were comparable. This indicates that a 1D model approach can also be used for a horizontal tank with long end. Fernández-Seara et al. examine changes in temperature profiles in a vertical tank due to heating and cooling (Fernández-Seara et al., 2007a), and changes in temperature profiles resulting from dynamic flow through the system (Fernández-Seara et al., 2007b). The 1D temperature profiles are used to quantify energy, exergy and stratification number. Haller et al. (2009) and Han et al. (2009) produce a summary of methods that characterise thermal stratification to measure the performance of storage tanks.

Tank geometry is expected to play a role on the thermal stratification of a tank, specifically, the change in temperature gradient. It is posited that greater diffusion occurs with a greater surface area of the interacting cold and hot regions, i.e the base of horizontal tank has a greater area than vertical. This concept is examined by Eames and Norton (1998) through simulations of a tank model to describe the flow characteristics based on storage geometry with different inlet/outlet positions, which is further discussed in *Section 3.2.1*. Additional discussion on stratification effects due to tank geometry is presented in *Appendix B.2*.

The 1D model allows for the simplification of the thermal volume into one dimension based on the temperature gradient, even for an elongated geometry such as a horizontally oriented tank. Therefore, stratification can be modelled using a multi-node model, further discussed in *Section 2.5.3*.

2.4.3 Standing Losses

The standing losses of a thermal system is the heat lost to the system due to ambient temperature (otherwise defined as steady-state operation in *Section 2.4.1*). This quantity is also known as “standby loss” (ASHRAE, 2003). The tank remains in equilibrium during steady-state, therefore the standing loss can be quantified by the observation input energy for steady-state replacement events over time in the absence of a draw event.

The maximum standing loss rating for manufactured EWHs is based on the SANS 151 (2013) standard. For a 150 ℓ cylinder, the typical standing loss over 24 hours is 2.59 kWh. This is shown in *Equation 2.1*, by adding the element cycles over a 24 hour period where E is the standing loss energy (kWh), P_E is the rated power of the element (kW) and t_{ON_T} is the total duration of time that the element is in ON state measured in hours (hr) within a 24 hour period. This standing loss measure determines the quality and thickness of the built-in insulation of the manufactured product.

$$E = P_E \times t_{ON_T} \tag{2.1}$$

Yen et al. (2017) investigate the difference in standing losses on an EWH in horizontal and vertical orientation with different levels of additional insulation. The findings show that vertical standing losses were up to 33% less than the horizontal orientation.

2.4.4 Hot Water Usage

The hot water usage has a direct impact on the electrical load demand of the EWH on the grid. Two important factors are the volume of water used, and the correlated time of use. Pearlman and Mills (1985) produce a comprehensive study on hot water usage profiles in Canadian households, which are still referred to in ASHRAE (2003)

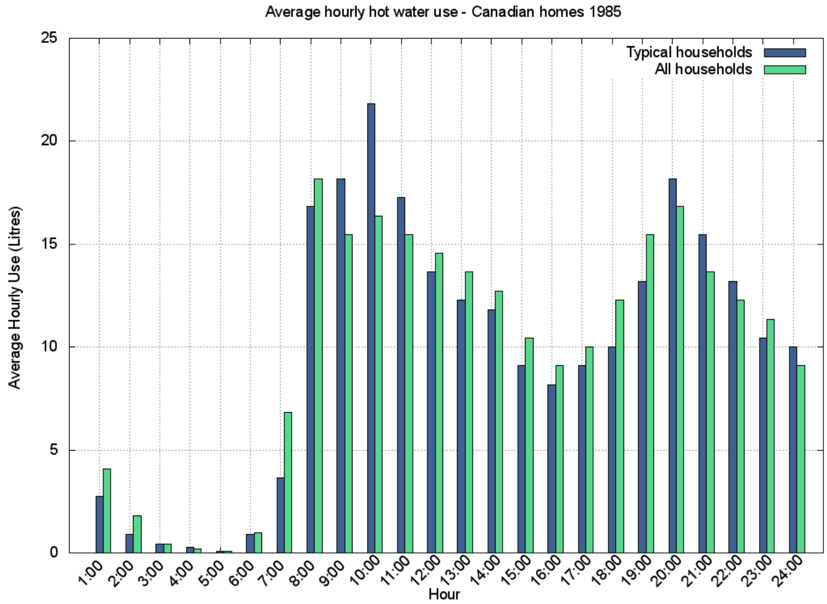

Figure 2.3: Hot water usage profiles (adapted from (Pearlman and Mills, 1985)).

standards. They determine that the average family consumes 239 ℓ/family/day. The hot water usage profiles are presented in *Figure 2.3*.

From a South African perspective, Meyer and Tshimankinda (1996) demonstrate hot water consumption of domestic users which vary based on living conditions. They produce estimated hot water consumption of South African domestic users based on monthly measurements over a year for different types of households. The high density and low density averages of measured hot water consumption for each type of household are as follows:

- Traditional houses is $5.0 - 6.3\,\ell$/person/day (Meyer and Tshimankinda, 1996).
- Apartments is $21 - 83.6\,\ell$/person/day (Meyer and Tshimankinda, 1998).
- Townhouses is $61.5 - 88.6\,\ell$/person/day (Meyer and Tshimankinda, 1998).

Meyer and Tshimankinda did not extend their study to time correlated profiles. Lane and Beute (1996) advocate the use of a Gaussian probability density function to model the random use of hot water in a population. Refer to *Appendix B.1* for consumer requirements for hot water, including temperatures and calculated flow and volume parameters.

This means that single hot water events are not disaggregated and therefore typical hot water usage profiles per user with time-correlated probabilities could not be

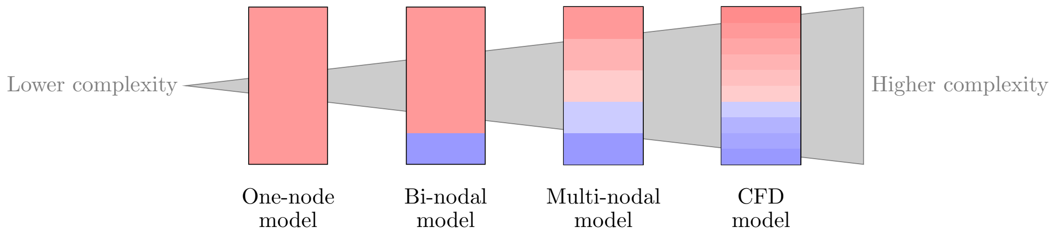

Figure 2.4: EWH models in order of complexity. Cross-section of vertical EWH models.

determined for South African households. This represents an opportunity for future work to ensure that this gap can be filled for consideration in EWH standards and energy regulations.

2.5 Existing Models

Load models are derived from thermal models (or changes to temperature gradients) in the tank due to actions on a tank such as draw events, as shown in *Equation 2.2*. The energy that needs to be restored into the system is determined by a change in temperature, ΔT with an associated volume of water, V, where ρ is the density of water and c_p is the specific heat of water. For the system to restore the energy drawn, the element with rated power P_E is turned into ON state and the duration, t_{ON} is determined. This assumes no losses to the environment, the heat is confined to the storage volume, element perfectly converts electrical energy to heat energy and that the energy entering the tank mixes throughout the volume to produce a homogenous temperature.

$$\begin{aligned} E &= \rho c_p V \Delta T \\ t_{ON} &= \frac{E}{P_E} \end{aligned} \tag{2.2}$$

The heat energy stored inside the tank can be modelled in several ways as shown in *Figure 2.4*. Most existing research refers to vertical tanks due to installation differences in other countries, as also illustrated in *Figure 2.4*. The trade-off in complexity of the models is often attributed to computational processing. The simpler the model, the easier it is to produce many instances of a tank and manipulate loads for modelling electrical demand on the grid. Models with higher complexity have a focus on internal mechanisms of the tank, including mixing and thermal stratification. These models will be discussed in the context of load modelling, where the heat replaced by the element is considered. While there are many studies that are relevant, only a few are mentioned for each model type.

Such abstracted models are roughly described in the form of the one-node model (*Section 2.5.1*), binodal model (*Section 2.5.2*), multi-node model (*Section 2.5.3*) and multiphysics solvers (*Section 2.5.4*).

2.5.1 One-Node

The key assumption made for the one-node model is that the storage tank holds one homogeneous temperature for the whole volume of water and therefore ignores stratification effects. For a draw event, some models simulate the drawing of energy from the storage tank as a full draw of the tank, therefore heating the tank up from ambient as presented by Palensky et al. (2008). Some models attempt to represent partial draws by mapping the trajectory of the representative tank temperature through known Markov states of the tank, as presented by Lu et al. (2005).

Dolan et al. (1996) provide a more complex model by using a first-order differential equation to describe the changes in tank temperature. Rautenbach and Lane (1993) also presents a more comprehensive model by abstracting the tank to represent only the thermostat temperature and devises a two-dimensional controller based on a linear differential equation to account for changes in temperature. This method is based on curve fitting, and would require a new set of coefficients with changes in inlet temperature.

2.5.2 Binodal Model

A binodal model (or two-node model) splits the tank into two homogeneous nodes which accounts for partial draw events from the system, and assumes perfect stratification between hot and cold portions (i.e. no mixing between nodes). The variable size of the volumes for each node changes due to the volume of water drawn from the tank, where the height of the lower node represents a perfect thermocline. *Figure 2.5* demonstrates an example of the binodal structure of the model. At the initial time ($t = 0$), the tank is full of hot water at the same temperature; both red segments are the same temperature. At time $t = t_d$, a volume of V_d is drawn out of the tank

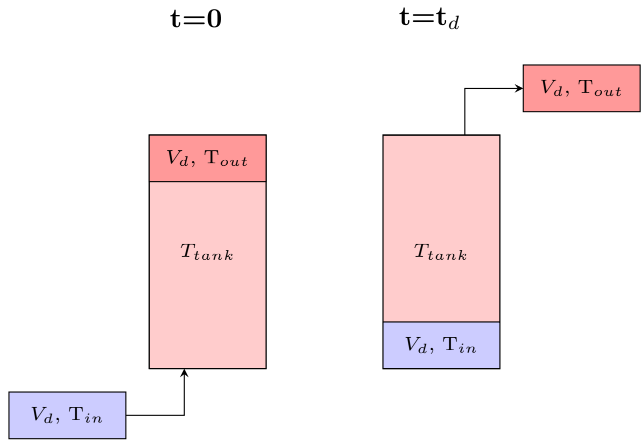

Figure 2.5: Binodal model or binodal model that abstracts the tank to two perfectly homogeneous regions.

from the top with outlet temperature, T_{out}. The same volume of cold water at the inlet temperature, T_{in}, is displaced into the tank from the bottom inlet.

The binodal model treats these two segments as seperate homogenous nodes in the tank and therefore allows for the required energy replacement to be easily determined. This simple model is also used in demand-side management where the heat replacement into the system considers only the displaced volume of cold water. Kondoh et al. (2011) present a binodal model for a two-element vertical tank.

A horizontally oriented tank using a binodal model approach was developed by calculating the node volmes using the horizontal tank geometry (Nel et al., 2016, Nel, 2015). *Equation 2.4* and *Equation 2.4* show the heat transfers for the upper and lower node in the tank.

$$cm_{upper}\dot{T}_{upper} = -\frac{1}{R_{upper}}\left[T_{upper} - T_{ambient}\right] - \frac{1}{R_{thermocline}}\left[T_{upper} - T_{lower}\right] \quad (2.3)$$

$$cm_{lower}\dot{T}_{lower} = -\frac{1}{R_{lower}}\left[T_{lower} - T_{ambient}\right] - \frac{1}{R_{thermocline}}\left[T_{lower} - T_{upper}\right] + E_{input} \quad (2.4)$$

The final term in *Equation 2.4* shows that the element energy is added into the lower node; the model logic indicates a conditional statement for element operation using the effective temperature of the two nodes. Therefore, this means that energy input in the system will occur in a single event to replace heat after a draw. Therefore, the energy based modelling used in the binodal model approach has limitations for determining time-correlated load demand.

Some binodal models expand to consider the thermocline between the nodes to reduce the degree of stratification. Leeuwner et al. (2017) extend the horizontal model by Nel (2015) with a parameter for internal nodal thermal resistance that determines the heat transfer through the thermocline.

2.5.3 Multi-Node

A multi-node model accounts for thermal stratification inside the tank. It accounts for a better representation of the temperature gradient that occurs in the tank. This is discussed in *Section 2.4.2*. This model separates the tank into individual layers of a water volume that is attributed a homogeneous temperature. This can be viewed as a 1D model along the height of the tank.

Young and Baughn (1981) first concluded that a 1D model is a good approximation for a tank in horizontal orientation. Alizadeh (1999) extend their work in horizontal tanks to investigate the decay of thermal stratification inside the tank using a multi-node model during full draw events. The work also presents mixing models during draw events. Farooq et al. (2015) present a grey-box multi-node model for a vertically oriented tank to predict the dynamics of the temperatures in each layer after a draw event.

Multi-nodal approaches comprise of thermodynamic modelling using a set of 1D partial differential equations. Vrettos et al. (2012) implement *Equation 2.5* where x denotes the position along the vertical axis, t denotes time, V is the vertical water velocity in the tank during draws, a is the diffusivity, k is the heat loss coefficient, T_a denotes ambient temperature and ϵ_{eff} accounts for the turbulence of the tank.

$$\frac{\partial T}{\partial t} + V\frac{\partial T}{\partial x} = a\epsilon_{eff}\frac{\partial^2 T}{\partial x^2} - k(T - T_a) + Q(x,t) \tag{2.5}$$

In addition, natural convection is modelled with the calculation of buoyancy forces (*Equation 2.6*) and viscous forces (*Equation 2.7*). The resultant displacement from the competing forces would determine the degree of mixing with the upper layers. Turbulent flow is modeled using Reynold's numbers that affect the water density.

$$F_i^b = min\left[0, gm_i\frac{\rho_{ref} - \rho_i}{\rho_{ref} + \rho_i}\right] \tag{2.6}$$

$$F_i^v = -bU_i \tag{2.7}$$

The approach by Kleinbach et al. (1993) is shown in *Equation 2.8.*

$$
\begin{aligned}
M_i C_f \frac{dT_i}{dt} &= \alpha_i \dot{m}_{heat} C_f (T_{heat} - T_i) + \beta_i \dot{m}_{load} C_f (T_{mains} - T_i) \\
&+ \delta_i \gamma_i C_f (T_{i-1} - T_i) + (1 - \delta_i) \gamma_i C_f (T_i - T_{i+1}) \\
&+ \epsilon \dot{Q}_{aux,i} - (1 - \epsilon) U A_{fl,i} (T_i - T_f l) - U A_i (T_i - T_{env})
\end{aligned}
\tag{2.8}
$$

where α_i is 1 if fluid flows from heat source, β_i is 1 if a returns from load, $\gamma_i = \dot{m_{heat}} \sum_{j=1}^{i-1} \alpha_j - \dot{m_{load}} \sum_{j=1+1}^{N} \beta_j$, γ_i is 1 if $\gamma_i > 0$ and δ_i is 0 if $\gamma_i \leq 0$ and ϵ is 1 if the auxillary is on and 0 if off.

Transient System Simulation Tool (TRNSYS) is a widely used modelling tool that incorporates multiple layers to simulate stratification in the tank (Klein et al., 2009). The tool incorporates the base model defined by Kleinbach et al. (1993). It also extends its application in multi-zone buildings. It has up to 100 homogeneous (or fully mixed) nodes that represent equal volume segments and can simulate up to two heating elements.

Other approaches consider the thermal storage as homogenised volumes assumed as solid nodes. Yen et al. (2018b) investigate an energy balance of a vertical tank based on volume segmentation in preparation for multi-node models.

2.5.4 Multiphysics Solvers

A multi-physics solver is useful in simulating the physical processes that occur in the tank due to flow dynamics within a 3D geometry, commonly referred to as Computational Fluid Dynamics (CFD). Commercial multi-physics packages include ANSYS Fluent[1] and COMSOL[2]. This is useful in diffuser design to promote laminar flow into the tank and reduce mixing of thermal layers. CFD models are computationally intensive and therefore are not ideal for aggregated load modelling.

Nicotra et al. (2018) evaluate the accuracies of two hot TES in a system with a micro-Combined Heat and Power (CHP) (65 – 75°C) and a heat pump at (45 – 65°C) for a 1D model in MATLAB[3], an assymetric Two-dimensional (2D) model in

[1]ANSYS Fluent website: `https://www.ansys.com/products/fluids/ansys-fluent`
[2]COMSOL website: `https://www.comsol.com/`
[3]MATLAB website: `https://au.mathworks.com/products/matlab.html`

COMSOL and develops their own reduced model to increase accuracy without the computational overhead.

2.6 Model Applications

Models are useful tools in predicting the behaviour of a system in an operational state. Thermal models predict the change in temperature gradients in a storage, which could assist in better understanding the development of a thermocline with implications of better preservation of hot and cold layers. These models could provide insight into the energy efficiency of a system, which could have implications on the development of amendments of standards and manufactured designs.

Thermal models can also be extended to load models. This combination of models is useful in building applications, where Heating, Ventilation, and Air Conditioning (HVAC) solutions are applied. This is discussed further in *Section 2.6.1*, which discusses the uses for single unit modelling of thermal systems. Load models can be used in a system-wide simulation that could assist in load forecasting and planning of an electrical grid and could be applied for DSM purposes. This is discussed further in *Section 2.6.2*.

2.6.1 Single Item Modelling

Single item modelling is useful when a specific application is required and accuracy has importance. An example of this is in building applications, where the sizing of components is important in the design phase. Thermal and load models are especially useful in combination for HVAC solutions and can assist with the integration of renewables into buildings (existing or new). These models are also very useful for cost-analysis of implemention of new solutions.

Arteconi et al. (2013) use TRNSYS to simulate DSM configurations for space heating using heat pumps and a thermal energy storage solution. Campos Celador et al. (2011) also use TRNSYS to investigate the predicted energy and exergy efficiencies of three thermal models of a CHP plant.

2.6.2 Aggregated Load Prediction for Demand-Side Management

Load aggregation is a technique used to determine the cumulative load contribution of an individual device or unit within a greater population of concurrently operating devices. This is achieved by stacking load profiles and summing the total power demand from each unit at each time step within an operational period (usually 24-hours) to produce an aggregated load profile. The time of use for each unit is relevant in a 24-hour load profile where large interconnected systems are considered, especially with the requirement of power utilities to supply against expected demand, such the electrical loading on the grid. This could be expanded to load control strategies for managing power demand through deferrable loads.

Approaches for load aggregation start with a base thermal or load model; often a simplified model ignoring stratification. There are several ways to use the base model to replicate more systems on the grid, often with randomness built in, either through Monte Carlo simulations, use of Gaussian probability density functions or Markov chains. The goal of load aggregation is to determine system characteristics such as peak demand or to test the effects of Demand Response (DR) or DSM strategies.

Lane and Beute (1996) produced a mathametical model that estimates the demand from a population of EWH based on a Gaussian probability density function. A $50\,\ell$ draw is considered with varying element sizes and temperature set points. Rautenbach and Lane (1996) used the devised two-dimensional model developed by (Rautenbach and Lane, 1993) in a multi-objective control strategy (similar to ripple control) to produce aggregated load profiles examining the effects of flat rate, end-user comfort and not exceeding maximum stored energy. Zhang et al. (2012) developed an aggregate model for a heterogeneous population of thermostatically controlled loads to evaluate the transients on the system caused by demand response. Dolan et al. (1996) used their model to aggregate many EWHs using a rejection type Monte Carlo simulation technique to assess the predicted impact of DSM strategies. Cheung et al. (2017) compared the two methods, based on the works of Nel et al. (2016) and Lu et al. (2005), in an aggregated system and showed the differences in predicted load that could occur in the models used.

None of these methods consider stratification and many of have limited capabilities to control flow rate or volumes of draw events. Vrettos et al. (2012) claim to be the first to demonstrate the effect of different control strategies for a frequency controlled model of a EWH population, accounting for dynamic processes within the tank for variable draw. However, the consideration for the transient effects in a horizontal tank still need to be investigated.

2.7 Conclusion

In this chapter, the load from an EWH has been placed in the context of the sustainability initiatives for ambitions towards net-zero emissions. Domestic water heating in South Africa has been discussed in context to the power supply issues in the country, with the opportunities considered through energy policy and DSM considerations.

The EWH is discussed in its fundamental components and operational states. The thermal storage performance of the tank is discussed in terms of the thermal stratification and standing losses. The hot water usage is also briefly discussed. A range of models have been presented, from thermal models that allow for 1D abstraction of tanks to load models that determine the energy required to replenish heat into a system. Finally, applications for such models are discussed, from building applications to load forecasting.

The next chapter covers the approach taken for this work, taking into consideration the background and methods introduced in this chapter.

Chapter 3

The Research Approach

This chapter covers the approach taken for this thesis. The problem is identified in *Section 3.1* and the hypothesis is presented in *Section 3.2*. The research objectives are presented in *Section 3.3*. The research approach and corresponding design decisions are presented in *Section 3.4*. The chapter concludes in *Section 3.5*.

3.1 Problem statement

The existing thermostatically-controlled load models for Electric Water Heater (EWH) presented in *Chapter 2* are energy-based. These models predict the amount of energy

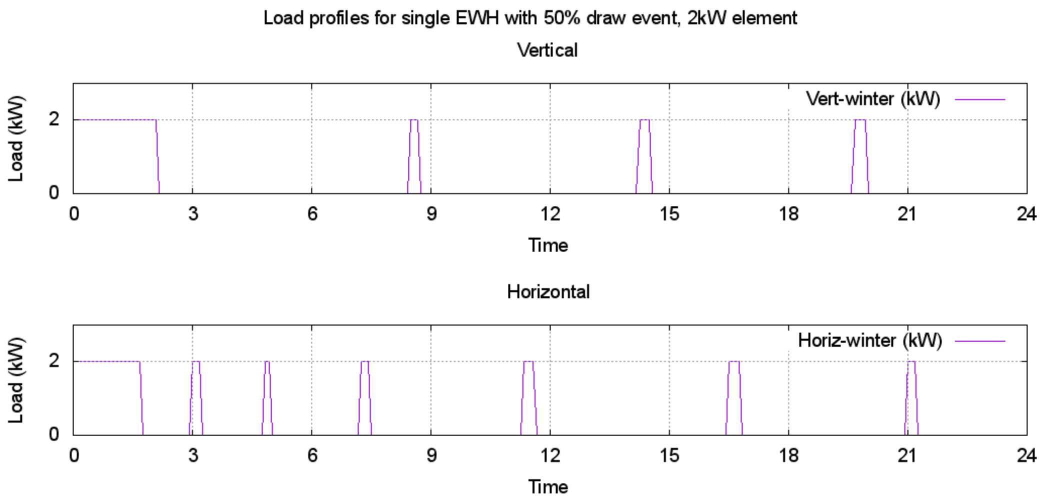

Figure 3.1: Measured load profile for a vertical (top) and horizontal (bottom) EWH for a 50 ℓ (50%) draw at 0 hrs (EWH with 2 kW element of 100 ℓ.

required for heat recovery after a draw-event and consists of a single replacement event that do not account for transient effects. These models hold true for EWHs in vertical orientation, but do not reflect the behaviour of an EWH tank in horizontal orientation. The difference in heat replacement profiles is shown in *Figure 3.1*, where a $50\,\ell$ draw event is taken from the same EWH in two separate instances while the tank is in vertical and horizontal orientation. The measured switching profile for the element due to heat replacement of a draw event is shown. Both experiments were performed in the same season with similar ambient temperatures.

In the vertical orientation, the element switches on for one element cycle to replace the energy drawn out and then the tank enters steady-state just before the 9-hour mark with a short, steady-state event. The three steady-state cycles in the vertical profile are evenly distributed in time, which shows that it takes only one element cycle to replenish drawn heat in the vertical orientation.

In the horizontal orientation, the element switches on for a relatively long period (but shorter than the vertical replacement period), but then switches three times over a period of several hours to replace the heat drawn out to finally reach steady-state just before the 12-hour mark (noon). Thereafter, there are three steady-state cycles that are evenly spaced. This indicates the transient element switching that occurs due to heat recovery post draw.

According to Yen et al. (2018a, 2019), if models only represent the single-event heat replacement for a draw event, the effect of this difference in element pattern could have significant load modelling effects in aggregated systems in South Africa. A notable load model produced for horizontally-oriented EWH is produced by Nel (2015), but it is binodal model which does not resolve the additional element events post draw; this is discussed later in this research work. Therefore, there is a need for a model that correctly describes the heat-replacement of a horizontally oriented tank.

3.2 Hypothesis

It is hypothesised that energy-based load models with simplified thermal abstractions do not sufficiently capture the cumulative EWH loading on the grid due to variable end-user draws. Improved maximum demand predictions are expected with a thermostatically-controlled model of an EWH that captures the horizontal

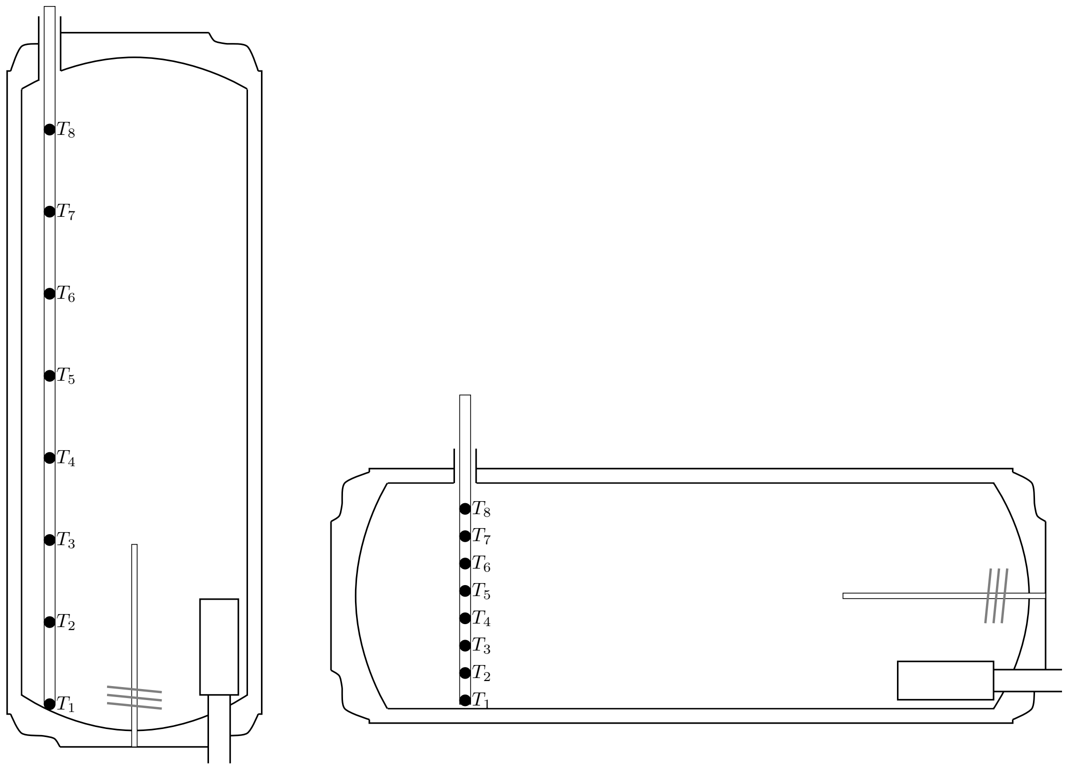

Figure 3.2: Temperature sensor placement in a vertical (left) and horizontal (right) 150 ℓ EWH, designed to resolve eight stratified layers within the tank (tank dimensions and sensor placement to scale).

orientation effects of the element switching profiles.

The important factors that lead to the difference in heat replacement profile of the horizontally mounted EWH are:

- tank geometry (which affects the thermal stratification during draw), and
- location of the thermoprobe and element.

This is shown in *Figure 3.2* where the tank in vertical and horizontal orientation are shown with a vertical sensor string along the height of the tank to measure temperatures in the tank at eight fixed heights to determine how the tank stratifies. The electrical element (and thermoprobe) in the vertical orientation is placed at the bottom of the tank, and therefore operates as soon as hot water is drawn and cold water fills in from the bottom of the tank. In this way, the tank in vertical orientation is able to replace heat in a single element operation. This is not the case in the horizontal orientation, where its position is approximately at the middle of the tank height. When cold water fills the tank during a draw event, and the thermoprobe is prompted to turn on the element, the element mostly heats up the layers above it due to the upward convection of heat. Therefore, this may be the reason why the element has several heat replacement cycles after a draw before steady-state is reached. For more on the experimental setup, refer to *Section 3.4.1*.

3.2.1 Stratification Effects of Tank Geometry

A CFD study was undertaken in collaboration with Prof Wei Hua Ho (affiliated with UNISA at the time of the study, more recently affiliated with Wits) to examine the qualitative effects of thermal stratification based on tank orientation. The CFD simulation was performed by the collaborator and the resulting simulation outputs were used to confirm the observed differences in thermal stratification in each tank orientation from experiments.

The same tank model has an initial starting temperature of 70°C (or 343 K) and it is subjected to a draw event of the full volume capacity at a fixed flow rate of $15\,\ell/\text{min}$. The evolution of the thermal storage in the tank is presented in *Figure 3.3*, with fixed time steps throughout the draw event, denoted t_1 to t_7.

The CFD simulation was modelled with an unstructured 3D mesh with no inflation in the mesh near the solid surfaces, as detailed boundary layer characterisation is not considered important for this application. The turbulence model used is the realisable k-epsilon with standard wall functions. The Boussinesq approximation is used with standard parameters in Fluent[1]. Mesh dependency is conducted and a time-step dependency of 0.1s is conducted.

A note should be made that the outlet ports for the tank in each orientation are different, based on the tank design. The simulations used the intended output ports designed for each orientation. The inlet is modelled as a cylinder that emits flow from all its surfaces inside the tank, therefore reducing the turbulent flow as a baffle would. The inlet is unchanged for both the vertical and horizontal simulations. There is no element nor ambient losses simulated.

The tank in vertical orientation is able to keep its hot and cold layers separate during the draw event, where a thin, well-defined stratification band is shown in the tank throughout the draw event. The tank in horizontal orientation, on the other hand, has more mixed layers, where the cold layer is not distinct and the stratification

[1]ANSYS Fluent website: `https://www.ansys.com/products/fluids/ansys-fluent`

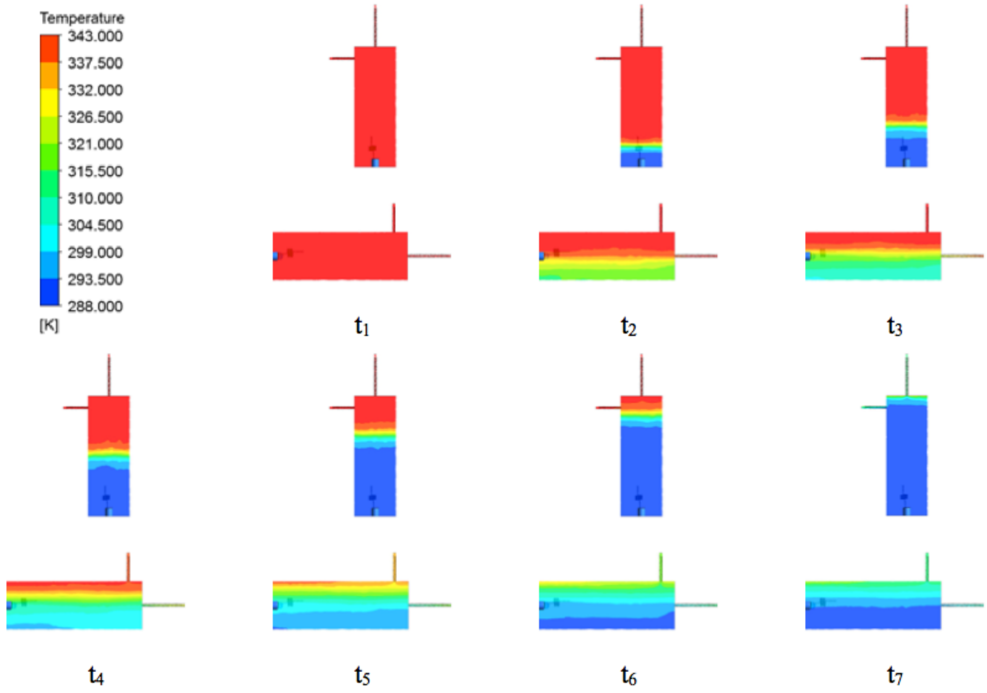

Figure 3.3: CFD time evolution comparison of hot water extraction at 15 ℓ/min for vertical and horizontal tank (in collaboration with Prof Wei Hua Ho).

band is large. The difference between the two orientations is easy to see from time step t_2, where the vertical has a distint blue (cold) and red (hot) region, and the horizontal orientation has half the tank mixed with cold water to produce a green hue (mixed).

It is theorised that this difference in stratification is due to the geometry of the internal tank. In the vertical tank, the layers are uniform, as the width or circumference of the tank is constant. The horizontal tank has a longer base, and the width of the tank increases towards the mid-height of the tank and the decreases back to a single strip.

Therefore, it is easy to see why vertical tanks are abstracted using the binodal model form, as there are two distinct regions in the tank, and the thermocline moves upwards without changing thickness. However, the binodal assumption appears to fail for the tank in horizontal orientation, and a multi-nodal approach may be more appropriate. These simulations also confirm that a 1D approach is appropriate for a horizontal tank, despite its elongated length.

3.2.2 Location of the Thermoprobe and Element

The difference in element operations for heat recovery has been established in *Section 3.2*, and *Section 3.2.1* provides some insight into the possible temperature stratification that occurs due to a draw through CFD simulation. Now the effects of the thermoprobe location and the element switching events for heat replacement of the tank are examined through a 150 ℓ draw of the tank in both horizontal and vertical orientation with a set of temperature sensors as shown in *Figure 3.2*. The expectation is to link the change in temperatures measured at fixed heights to element switching operations, to determine why the difference in heat replacement occurs.

The temperature and element measurements are presented in *Figure 3.4*. The flow rates are approximately 15 ℓ/min and the tests were operated in the same season where the ambient temperatures are comparable. This time scale shows the tank response for 24 hours after the initiation of a draw event. At this time scale, it is not possible to see the stratification effects of the tank during draw. The element operations show a similar profile to that presented in *Figure 3.1*, where the vertical EWH has one replacement event and the horizontal EWH has more than one, which verifies that this is a common trend. The results from *Figure 3.1* were taken from a different EWH than those presented in *Figure 3.4*.

For the tank in vertical orientation, shown in *Figure 3.4 (a)*, the element switches to ON state to replace heat from the draw event for a duration of 200 min. Thereafter, there are two steady-state events occuring around 670 min and 1 200 min. Sensors T_1 to T_8 operate between 25°C and 80°C, where $T_3 - T_8$ are clustered in the saw-tooth pattern (approximately all the same temperature). Temperatures measured by T_1 are approximately 10°C lower than the rest of the tank, which could be due to the fact the sensor is touching the base of the steel casing and therefore subjected to conduction losses. This is also the portion of the tank that is just below the element, which does not get heated as readily as other portions, due to convective heat transfer. The temperatures measured by T_2 are generally higher than the rest of the tank, which could be due to the fact that it is the closest sensor to the element. The thermoprobe cuts through several heights represented by temperature sensors (up to T_3 in the schematic in *Figure 3.2*) and therefore, it could be taking an average of several temperatures for the element switching function.

For the tank in horizontal orientation, shown in *Figure 3.4 (b)*, the element switches to ON state to replace drawn heat for a duration of 150 min, switches to OFF state

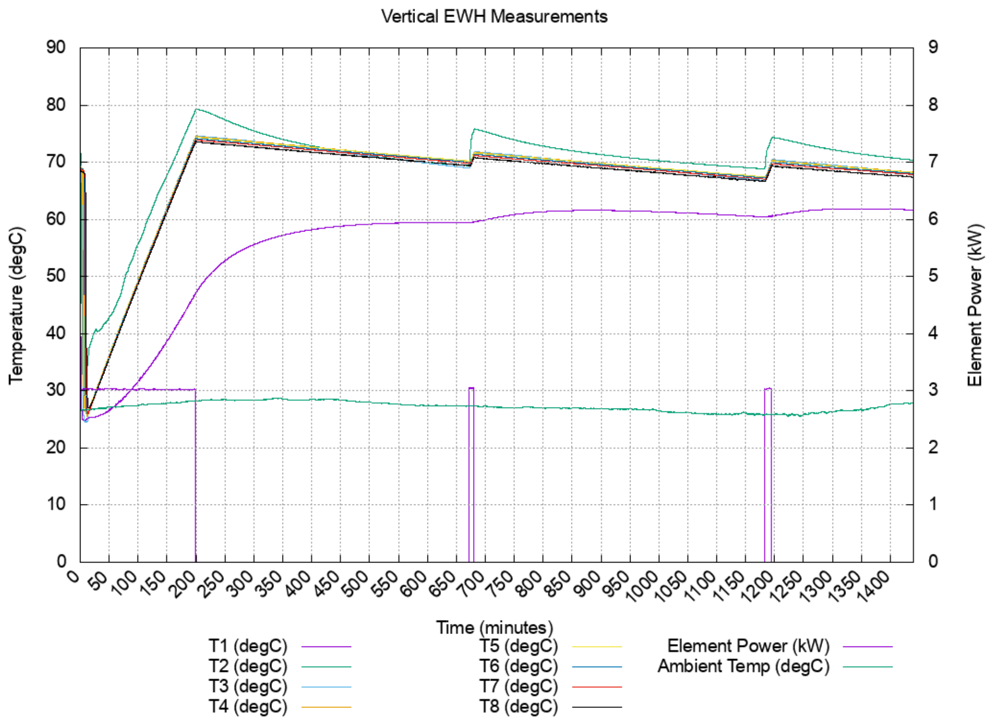

(a) Vertical Orientation.

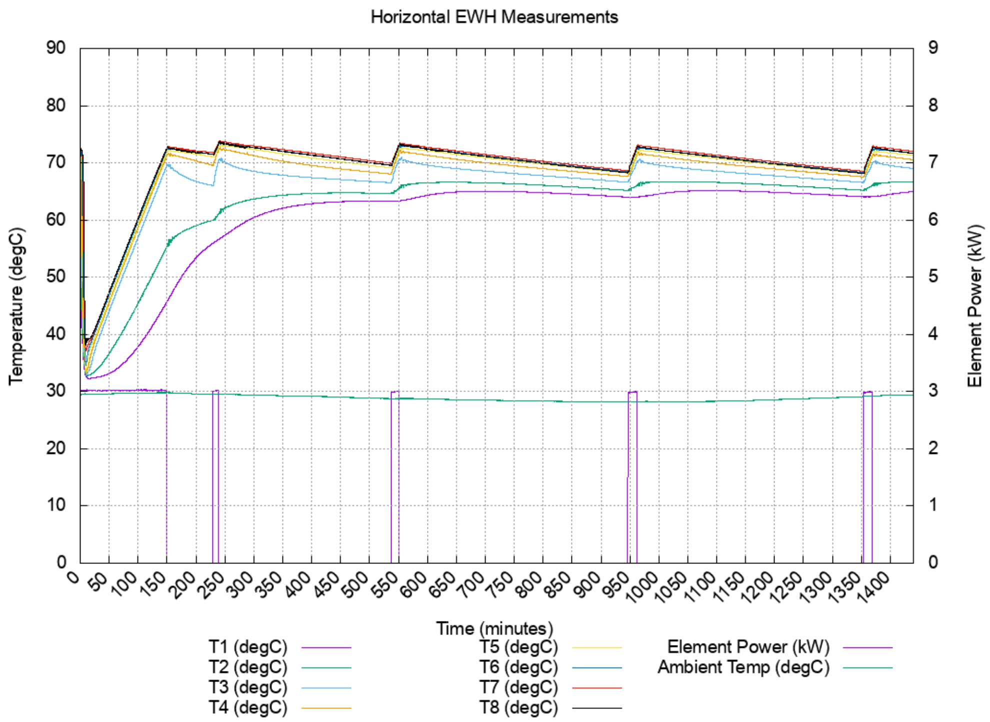

(b) Horizontal Orientation.

Figure 3.4: Temperature and element measurements for a 150 ℓ draw (100% capacity) for an EWH in (a) Vertical and (b) Horizontal orientation.

for a short period of time before switching to ON state again for a short period occuring at just under 250 min. These events are termed “primary replacement” and the “subsequent replacement”, as defined in *Section 4.1.* Thereafter, there are three element ON events that appear to be steady-state operation. When observing the temperatures measured in the tank, it is evident that sensors T_1 and T_2 remain colder than the rest of the tank. A well-defined saw-tooth or hysteresis is observed for T_3, where the maximum and minimum switching temperatures appear to be consistent, which indicates that the location of this sensor possibly matches the height of the thermoprobe. Sensors T_4 to T_8 are clustered at temperatures higher than T_3, where T_4 operates at a slightly lower temperature.

Therefore, it can be seen that the location of the thermoprobe and the element have a signficant effect on the temperature gradients and the resulting element operations due to the thermoprobe location. A common trend shown in both orientations is that regions above the element hold a higher temperature and generally have a smaller range of values. In regions below the element, there are significantly lower temperatures measured.

The switching temperatures read by the thermoprobe in vertical orientation are not clearly shown in the measurements (i.e. no layer that clearly switches between a lower threshold and upper threshold). It is therefore assumed that an average value is taken of the temperature regions it cuts. However, in the horizontal orientation, it is clearly seen that T_3 switches at fixed temperatures at upper and lower bounds, and therefore the height of T_3 is matched to the location of the thermoprobe. Therefore, a layer associated to this height is a good candidate for controlling the switching temperatures if a 1D multi-node model approach is taken.

The final observation made for the EWH in horizontal orientation is that sensors T_1 and T_2 do not reach their steady-state temperatures after the primary heat replacement event, which could be the reason why the temperature for T_3 reduces to its lower temperature bound to produce the subsequent element event occuring at approximately 250 min. The temperature gradient for T_3 on its first cooling phase decreases at a greater rate than its steady-state gradient, which suggests that the colder regions below it, shown by T_1 and T_2, may contribute to the greater rate in decreasing temperature. It is likely that this feature would need to be incorporated into the model for the subsequent element events to occur.

3.3 Research Objectives

The horizontally-oriented EWH produces transient element switching in the heat recovery of the tank post draw event, which is attributed to the tank geometry and location of the heating and control elements. This switching behaviour produces additional element replacement events, which are not captured by currently available load models for thermal storage tanks. Many load models published in literature abstract the thermal contents of a tank to produce a single heat replacement event; this modelling strategy is better suited for vertically-oriented EWH.

A multi-nodal model can produce thermal models with a high degree of stratification in a tank and therefore should resolve the transient switching events observed. This proposed multi-nodal model will be used as a base model to determine the cumulative system effects and evaluate whether it has a better performance than available models that have simpler thermal abstractions. The maximum demand is of particular interest because DSM strategies focus on this system factor.

Therefore, this thesis addresses the question of: *Can a multi-node model be used to predict element switching in a horizontally-oriented EWH post draw event to produce better peak demand predictions for system loading on a grid in comparison to load models with simpler abstractions?*

To answer the question, the following objectives are formulated:

1. To develop a thermostatically controlled load model with a multi-nodal approach for a horizontal EWH with element switching fidelity to resolve subsequent events for variable draw volumes and flow rates.
2. To predict peak demand for the aggregated system with better overall performance than a binodal model developed for horizontal EWH.

The following sections describe the methodology for how these objectives will be achieved and verified.

3.4 Methodology

This section presents the methodology taken to examine the hypothesis and research objectives. The experimental setup and procedure is discussed in *Section 3.4.1* and the choice of experimental scenarios for hot water draws is presented in *Section 3.4.2*. A discussion on the choice of modelling strategy is provided in *Section 3.4.3* and the subsequent application of the model to discuss the cumulative effects is provided in *Section 3.4.4*.

3.4.1 Experiment: Setup and Procedure

A typical 150 ℓ, 3 kW, dual-mountable EWH is considered. The measurements taken on the EWH are shown in *Figure 3.5*. There are 13 time dependant quantities, indicated by (t), that are sampled at a per second rate on individual channels on a measurement logger. A detailed schematic and discussion on the components used in the experimental setup is presented in *Appendix A*.

The temperature measurements are made using Resistance Temperature Detectors (RTD) or PT100s with Class A rating, which have a range of −50°C−500°C (refer to *Appendix A.2* for more on the calibration of these devices). For temperature sensors, T_1 to T_8, that are placed inside the tank, a temperature string was designed with fixed spacing of 55 mm, which approximates eight equi-distant measurements along the internal height (D_I). The sensors are encased in a steel casing with a thickness of 2 mm. The inlet temperature, T_{in}, is measured from the manifold with a RTD attached to the exterior of the copper pipe. The outlet temperature, T_{out}, is measured on the outlet pipe with a RTD attached on the pipe exterior. It is assumed that the differences in temperature of the external pipe and internal fluid at the inlet and outlet are negligible. The ambient temperature, T_a, is measured from a RTD attached to a metal structure on the testing platform.

The flow rate, q, is set at the inlet-side with a manually-operated flow control valve

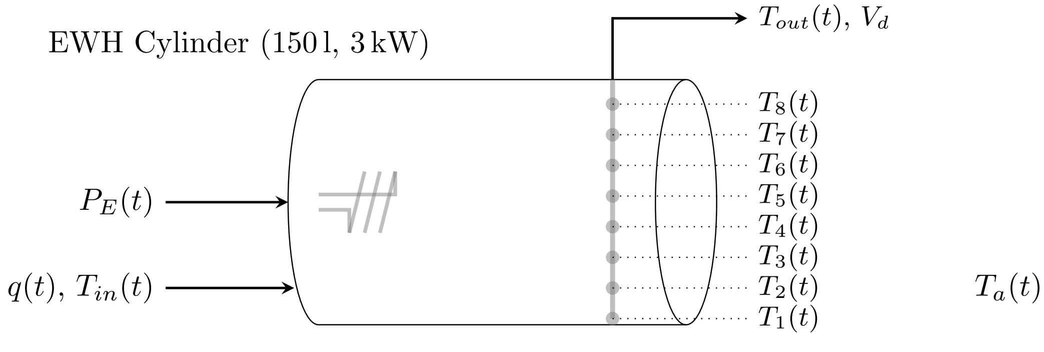

Figure 3.5: Sensor placement for measurements of a horizontal EWH.

and the volume drawn over time, V_d is dispensed in a separate container on the outlet-side and measured by a load cell. For recording purposes, the value provided for flow rate is the equivalent flow rate, which assumes that a fixed flow rate is used for the duration of the draw event. This equivalent flow rate is verified using the total dispensed volume, V_d. The flow rate is also measured using a flow meter, which provides a per-second time-stamp to indicate when a draw event occurs.

The element state switching is measured through a current transformer, which provides per-second time-stamps on a change of element state. The element has a fixed rating of 3 kW. The element is confirmed to be purely resistive, with no reactive power components associated to any measurements. Separate voltage supply measurements were not taken.

To ensure that test results are comparable, the experiments were run in the same season with relatively constant ambient temperatures. Each draw event was only initiated at the maximum temperature of the tank, i.e. after the element turns from ON state to OFF state for a steady-state element event. The procedure was as follows:

- While tank is in steady-state, once it reaches its maximum temperature and thermostat automatically switches the element to OFF state.
- A draw event of a fixed volume capacity is administered at a fixed flow rate. The element will automatically switch on to start replenishing heat into the system.
- Allow for 24 hours (or 1 440 min) of measurements to observe the element operations.

While this is a very controlled procedure for a draw event, which is by naturerespresents a stochastic event when in operation (i.e. a draw can happen anywhere in the steady-state cycle), it is used to ensure that starting tank temperatures are comparable and experiments can be compared to each other. To examine a realistic draw profile, a double-draw event is also considered.

3.4.2 Experimental Hot Water Draw Events

To characterise the element switching profiles for horizontal tank events, the difference between steady-state events and draw replacement events should be defined and quantified. This will provide the basis for using such terminology in describing the observed element events. The two measured quantities which indicate the tank status are the internal temperatures and the status of the electrical element. The thermostat height also needs to be determined and it is not as easy for the vertical orientation. The element switching events for the element are observed for the characterisation of tank status.

The element events associated with a draw event need to be differentiated from steady-state operations. The steady-state ON/OFF element operations are defined through the statistical analysis of many steady-state element events where the time durations in each event are used. Steady-state occurs independently of draw events and the time cycle variations due to ambient are within a constant range. Therefore, it is assumed that element events associated to heat replacement from a draw event would be differentiated by durations not equal to those of steady-state. From inspection, a further assumption that OFF durations for draw replacements would be shorter than the steady-state counterparts.

A range of experiments are presented that could be representative for load modelling purpose and linked to end-user hot water events (based on flow rate and draw volume). The considered model needs to incorporate variable response for flow rate and draw volume and therefore a wide range of possible draws is considered. The single draw event scenarios considered for testing the model examine a medium to large draw event from the tank to roughly simulate consumer-end usage of hot water. The relation of end-user hot water service to piped hot water from the storage tank is shown in *Figure 3.6* and shown mathematically in *Equation 3.1.* The mixed temperature at the end-user, T_{EU} and the corresponding flow rate q_{EU}, are dependant on the temperatures and flow rates on the hot water line (T_{HW}, q_{HW}) and cold water line (T_{CW}, q_{CW}). The volume of hot water drawn from the tank, V_{HW} is determined by multiplying the flow rate q_{HW} to the duration of the draw event, t_d, as shown in *Equation 3.2.*

$$T_{EU}q_{EU} = T_{HW}q_{HW} + T_{CW}q_{CW} \tag{3.1}$$

$$V_{HW} = q_{HW}\, t_d \tag{3.2}$$

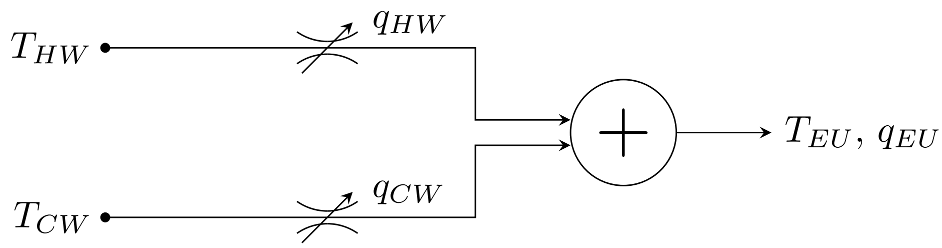

Figure 3.6: Hot and cold water mixing for end-user consumption.

Four draw event scenarios on the hot water line (V_{HW} and q_{HW}) are listed as follows:

- 50 ℓ draw at low flow rate (control)
- 50 ℓ draw at high flow rate (validation)
- 100 ℓ draw at low flow rate (validation)
- 100 ℓ draw at high flow rate (validation)

The flow rates used for the experiments refer to only the hot water pipe and not flow rates on the consumer side. The low flow rate is set at approximately 8 ℓ/min on the hot pipe, which simulates the mixing of 70°C hot water and 20°C cold water mixing to produce an output of 16 ℓ/min (for an average showerhead) at 43°C (the temperature appropriate for a bath or shower, according to ASHRAE (2003)). The high flow rate is set to 30 ℓ/min, which simulates a fully-opened tap on the hot pipe. Refer to *Appendix B.1* for further details on calculations.

The volume drawn from the EWH tank is 50 ℓ and 100 ℓ, which corresponds to 33% and 66% of the tank capacity. For a low flow output of 16 ℓ/min at 43°C, a 50 ℓ draw from the EWH approximates to a shower of a duration 6.8 min and a 100 ℓ draw approximates to a shower of duration of 13.6 min. A high flow scenario (30 ℓ/min) would simulate a bath, where only hot water is used to fill the tub. This is considered a less frequent occurance, but represents a boundary condition of the highest possible flow rate from the EWH. Since baths have a capacity of 80 ℓ, the 50 ℓ high flow draw would simulate a very hot bath, whereas a 100 ℓ high flow draw would overfill the tub.

Of the four scenarios, some represent realistic usage in a domestic situation, whereas others are there to provide a comparison point. For instance, the 100 ℓ high flow draw is considered for completeness of the study and is not intended to correspond to realistic use in a domestic environment. While the model will be tested against these scenarios, it is believe that there is a wide enough range in the choice of scenarios to determine whether the model parameters would hold for any choice of flow rates or draw volumes.

In addition, a double-draw scenario is tested to determine the performance of the model under non-ideal conditions. The double-draw scenario considered is two 25 ℓ draws with a 10 min separation at low flow rate. This could be representative of two very short showers within the same household.

The data collected from the system includes the heat recovery of the tank from the draw event and steady-state cycles up to 24 hrs after the draw initiation, as stated in *Section 3.4.1.* For each set of experimental parameters, the time durations in each element state is characterised to determine a variation for each element state duration. This is performed to ensure that a draw event at a specific flow rate, draw volume and ambient temperature produce results in element ON/OFF durations that can be matched with some confidence to a simulation with the same set of input parameters.

3.4.3 Model and Verification

The studies on horizontal tanks show that the temperature gradient is most prominent along the height of the tank, and the width of the long tank has little variation in its stratification of layers (Alizadeh, 1999, Eames and Norton, 1998, Young and Baughn, 1981). This is also confirmed in the CFD simulations discussed in *Section 3.2.1* that shows that the left hand side of the tank has a similar temperature gradient as the right hand side of the tank. Alizadeh (1999) shows this by measuring the tank in three locations along its width and concluded that after transient effects, all three locations reported comparable temperatures. Therefore, abstracting the tank, with no constraint on the length, to a 1D equivalent is possible, as per discussions in *Section 3.2.1.*

The multi-node model approach was chosen to model the stratification effects observed in the tank in an attempt to resolve the correct element switching profile post draw event. This approach is based on a model by Farooq et al. (2015) which predicts temperature changes in vertical tank due to a draw event. This concept is extended for this study to a horizontal tank with constant height segmentation into layers consistent with the temperature measurement string (shown in *Figure 3.7* is eight layers). The approach by Farooq et al. (2015) uses temperature measurements to

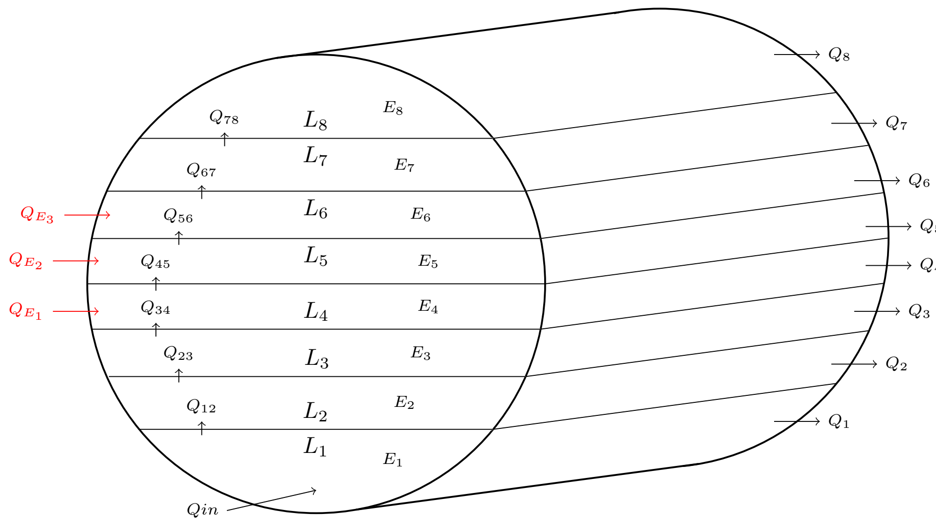

Figure 3.7: Proposed dynamic energy balance for horizontal tank.

Table 3.1: Comparison of models based on the computation time for and model fidelity for binodal model (BN), multi-node model (MN) and computation fluid dynamics (CFD).

Parameter	**BN**	**MN**	**CFD**
Computation time for draw event (s)	0.8	1.3	4 000 – 8 000
Computation time for 24-hr simulation (s)	3.7	30.9	N/A
Temperature fidelity	Fair	Good	N/A
Element switching fidelity	Inadequate	Good	N/A

determine the heat conduction coefficients between adjacent water layers (eg. U_{12}), and defines a different coefficient for each layer boundary. The heat introduced to the system is also distributed evenly throughout each layer. Key differences expected are as follows: (i) layer attributes adjusted according to horizontal geometry, (ii) fixed height layers, not fixed volume, (iii) identify layers directly affected by element, (iv) heat transfer coefficients linked to heat transfer processes, (v) heating and cooling tank states incorporated, with state switching logic.

Table 3.1 demonstrates the binodal model (BN), multi-node model (MN) and CFD comparisons made for simulating draw events and the corresponding computation times. The multi-node model performance is presented for 24 or (8×3) layer structure. The CFD implementation produced no comparable results for temperature fidelity as due to differences in tank sizing factors, and element switching as only draw simulations were considered. However, it could be assumed that there would be high temperature fidelity and therefore high fidelity for element switching. Computation times for each of the model simulations were performed on comparable processors.

For the multi-node model, the geometries are determined to represent the stratification of layers based on a fixed height of each layer. This means that the temperatures measured from T_1 to T_8 in the temperature string can be directly compared to temperatures in layers with a corresponding height. A comparison of 8, 16 and 24 total layers is presented in *Appendix C.1.* The total number of layers, N, is chosen as 24 or (8×3) layers. The larger number of layers allows for finer control on the height of the element-effected layers, which is an important feature for simulating the subsequent element operations.

Each of the layers are presented as nodes, for which heat transfer relationships need to be determined for each state: heating, cooling and draw state. The heat transfer co-efficients are determined heuristically based on one set of control data. The model and set of heat transfer co-efficients are validated against the other three experiments determined for load modelling purposes.

The simple models produce excellent performance in terms of computation time. However, it was also noted in *Section 3.2.1* that the one-node model or binodal model would not be a sufficient abstraction of the tank in horizontal orientation to resolve the additional element operations due to a draw event (subsequent draw replacement events). The multi-node model shows better promise for simulating nodes that hold lower temperatures as shown in T_1 and T_2 from *Figure 3.4 (b)*, with a reasonable computation time of 30.9 s to compute 24-hours for a single item.

An existing simulation tool, TRNSYS, will not be used due to its limitation of equal-volume nodes. The multiphysics CFD simulation presented in *Figure 3.3* had a simulation time of a single draw event that resulted in a computation time of $4\,000 - 8\,000$ s. It was not investigated further for several reasons: (i) long simulation durations, (ii) large computational resource overhead, (iii) losses and insulation not yet implemented, (iv) complicated element geometry and coding of logic. The long computation time for a single draw event was deemed unsuitable for application of aggregated loads and the work was discontinued in the early stages.

3.4.4 Application

Finally, the outputs from the multi-node model are applied in an aggregated system that determines the cumulative effects of maximum demand, time to peak and total system energy from a set of fixed draw events. The method used is defined by Yen et al. (2019) to determine the difference in power demand of a population of EWHs based on tank orientation if the same water service is produced on the user end. The method compares two element switching profiles that result from the same hot water draw (in volume and flow rate) but with different tank orientations (vertical and horizontal) and replicates that switching profile to produce aggregated load profiles for comparison.

This method is adjusted to aggregate the element switching profiles from the experiment and corresponding simulated load output, to compare the expected cumulative effects. This method is also used to compare the cumulative effects from a commonly used load model (binodal model to compare model prediction performance). The EWH population size and the peak time interval is varied to examine a large range of load modelling outcomes. The performance factors are discussed for the following criteria: predicted maximum demand, time to peak and total energy of system. The cumulative performance of the proposed base model is contextualised for the use of EWH load models for demand-side management strategies.

3.5 Conclusion

In this chapter, the key difference in element switching profile due heat recovery from a draw event is discussed for an EWH mounted in vertical and horizontal orientation. The horizontal orientation has several ON/OFF element operations before the tank reaches steady-state. Most load models in literature take a simplified thermal abstraction approach to replace heat in a single element operation for a calculated duration and then the tank enters steady-state. These models are representative of EWHs in vertical orientation, but do not adequately capture the transient effects of the horizontal orientation.

It is identified that the geometry of the horizontally oriented tank and the placement of the internal components, specifically, the element and thermoprobe, have an effect on the way a horizontally oriented EWH replaces heat from a draw. The several ON/OFF element operations occur due the fact that regions below the element heat up slower than regions above the element. The thermoprobe region, which could be approximated to the element region, therefore cools faster from the initial replacement event, causing the element to have several ON/OFF operations before steady-state is reached.

The research question is re-iterated with two objectives formulated to answer the question. The objectives are supported by a detailed methodology for the research approach. This is supported by design decisions that have been discussed and justified in relation to the choice of model, choice of experimental parameters and choice of methods.

A road map is provided for producing a model that can correctly reproduce the element ON/OFF operations of a horizontally oriented EWH. The status of the tank should be characterised based on durations in element status for steady-state and draw replacements. Four single-draw test scenarios are considered, one control and three for validation, encompassing different draw volumes and flow rates. A double-draw scenario is also considered to demonstrate the model performance for a realistic draw profile. A 1D multi-node model is considered, where the tank is segmented into 24 layers and heat transfer relationships of each layer should be defined for each tank state.

An application for aggregated systems using the proposed horizontal load model is discussed. A comparative study is conducted with a binodal model to evaluate the difference in cumulative sperformance. The method used to determine the aggregation effects compares a repeated element switching profile from measured experiments to the repeated simulated element output with varying EWH population and peak time interval. This method is used to validate the use of the model output to model peak demand and total energy.

The next chapter investigates the characterisation of the tank modes through the durations of the element in ON and OFF states to differentiate steady-state operations from draw event replacement.

Chapter 4

Characterisation of EWH Element Operations

This chapter covers the characterisation of element operations for the EWH in its steady-state operation and in draw replacement based on chosen experimental parameters. The terms required to define the element states and tank states are discussed in *Section 4.1*. The steady-state characterisation is presented in *Section 4.2*, which provides the framework for the heat recovery characterisation, presented in *Section 4.3*.

4.1 Definition of Terms

The tank can be characterised in its different states based only on the status of the heating element. The element in ON state indicates the drawing electrical power to heat up the tank. The element in OFF state indicates that no power is drawn from the grid, and the tank enters cooling state where temperatures start to decrease due to the standing losses.

The duration of the element in each state (t_{ON} and t_{OFF}) could also be used to determine which state the tank is operating in. The two major states defined based on the status of the heating element are: (1) steady-state and (2) draw replacement. *Figure 4.1* shows the element operations due to a draw event followed by steady-state operations. These element states are dependant on temperatures changes measured in the tank, in particular, the thermostat layer (not depicted in the figure).

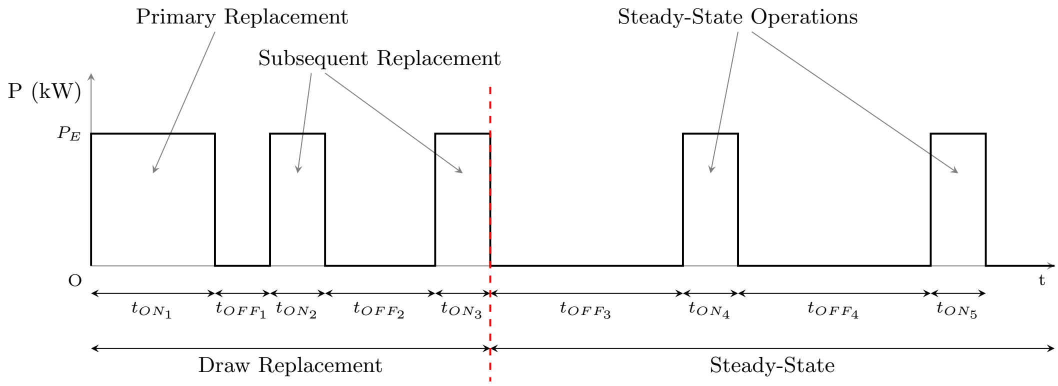

Figure 4.1: Definition of terms for draw replacement events (element operations due to a draw event) for a horizontally oriented EWH.

There are several factors affecting the durations of the element in each state, including: tank volume, element size, tank orientation, thermal insulation, temperatures, amoung other factors. Therefore, it should be noted that the values produced in this chapter cannot be directly compared with a different tank or the same tank operated under different situations.

The tank in steady-state occurs independently of a draw event. It is characterised by short t_{ON} durations (scale in minutes) and long t_{OFF} durations (scale in hours). The ambient temperature will have an effect on the t_{OFF} durations, where a higher ambient temperature increases the duration and a lower ambient temperature will reduce the duration. The steady-state characterisation for state durations is discussed in *Section 4.2*.

The draw replacement is the combination of element operations required to replace heat energy removed from the tank due to a draw event. As discussed in *Chapter 3*, the heat recovery in a horizontal tank is different to a vertical tank where the replacement cycles are split into a primary and subsequent events (shown in *Figure 3.1*). The primary replacement event is the first event that occurs with a relatively long duration, denoted t_{ON_1}. This is followed by two subsequent replacement events, t_{ON_2} and t_{ON_3} where the preceeding OFF event durations t_{OFF_1} and t_{OFF_2} are expected to be less than the steady-state counterparts. Depending on the type of draw event (flow rate and draw capacity), there can be one to three subsequent element events, until steady-state is reached. This schematic shows two subsequent element events. The draw replacement characterisation for element state durations is discussed in *Section 4.3*.

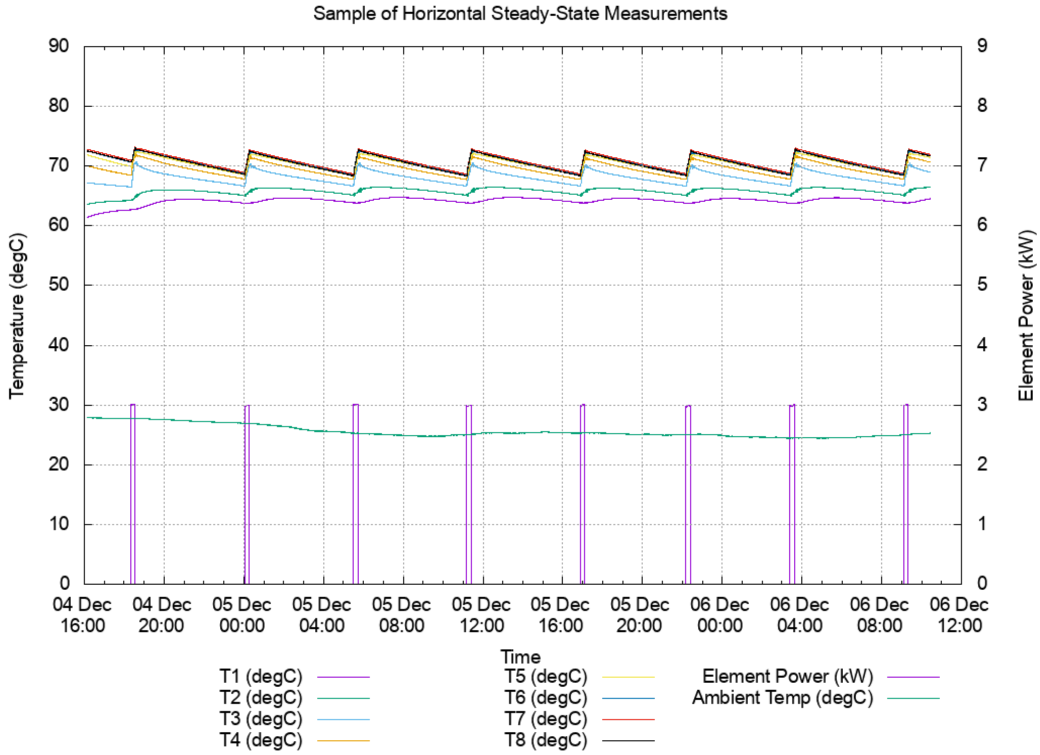

Figure 4.2: Steady-state measurements of a horizontal EWH.

4.2 Steady-State

The steady-state operation of the EWH comprises of the heating and cooling states of the TES where there is no mass exchange from the storage tank, that is, when water is not drawn from the tank. These heating and cooling states occur as a result of heat exchange of the tank to the environment (ambient temperature) and the controlled set point of the EWH to replenish lost energy due to "standing losses" (refer to *Figure 2.2* in *Section 2.4.1* and *Section 2.1* for definitions).

By tracking the temperature measured in the tank, the steady-state operation of the EWH is shown as a "saw-tooth" trend, as illustrated by temperature sensors $T_1 - T_8$ in *Figure 4.2*. The rate of heating is determined by the rating of the heating element. The rate of cooling is determined by the built-in insulation and the ambient temperature.

In this section, a characterisation of steady-state operation will be defined based on element state duration for the tank under test in a specific season, as outlined in *Section 3.4.2*.

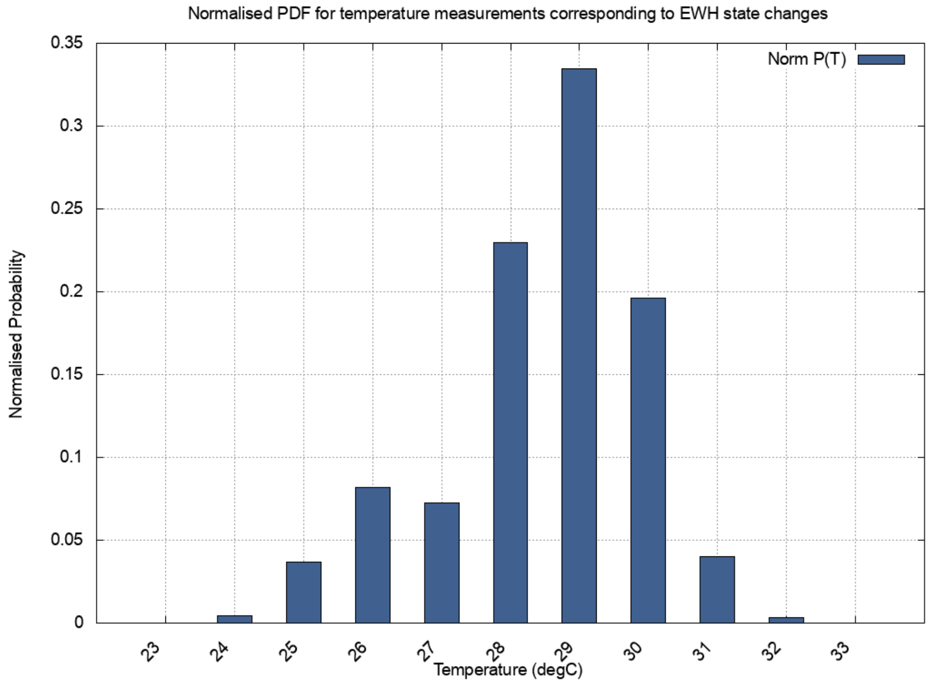

Figure 4.3: Normalised probability distribution function for sampled ambient temperature measurements for steady-state operation (total samples: 648).

4.2.1 Characterisation of Steady-State Operation

The EWH under test, as described in *Appendix A.1.2*, was operated in steady-state for several days within the summer season to obtain many switching events of the EWH. The ambient temperature is the primary variable affecting the steady-state operation of the EWH and is therefore measured to ensure that resulting ON/OFF durations can be correlated to ambient.

- 648 samples of ambient temperature; corresponding element switching,
- 317 samples of duration times in ON state,
- 308 samples of duration times in OFF state.

While ambient temperature measurements are taken at a 1 s sample rate (resulting in many more samples), the samples for ambient temperatures are taken from corresponding switching events for ease of processing. As shown in *Figure 4.2*, the ambient temperature does not vary much between steady-state element events, and therefore the assumption that temperature measurements corresponding to switching events

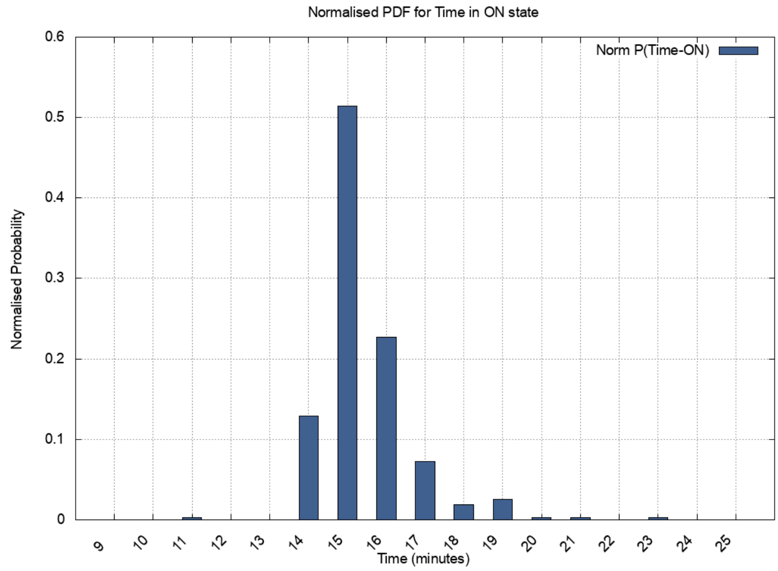

(a) Element in ON state, t_{ON} (total samples: 317).

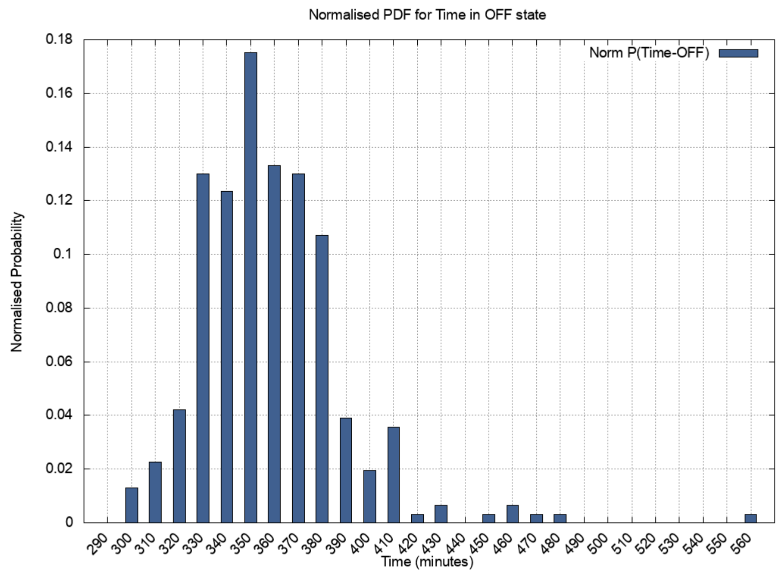

(b) Element in OFF state, t_{OFF} (total samples: 308).

Figure 4.4: Normalised probability distributions for sampled element state durations for steady-state operation.

would be a sufficient representation of ambient temperature variation during the time of experimentation is considered valid.

The normalised probability density distribution of the ambient temperature measurements corresponding to the switching events is presented in *Figure 4.3* for 648 samples. The bins are sized at 1°C per bin on the x-axis, and values on the graph represent the maximum of the bin. Ambient temperatures vary between 24°C and

32°C with a mean appearing in the 29°C bin contributing to 33% of the population and a standard deviation of ±1.4°C.

The durations of the element in ON state, t_{ON}, are presented in a normalised probability density distribution as shown *Figure 4.4 (a)*. There are a total of 317 samples in the dataset. Each bin size is 1 min on the x-axis, and values on the graph represent the maximum of the bin. The sample-set has a mean in the 15 min bin and contributes to 51% of the population. There is a standard deviation of ±1.18 min. The minimum appears in the 14 min bin with a single outlier in the 11 min bin. There is a longer tail in the distribution for durations greater than 15 min, with a maximum occuring in the 23 min bin.

The durations of the element in OFF state, t_{OFF}, are presented in a normalised probability density distribution as shown *Figure 4.4 (b)*. There are a total of 308 samples in the dataset. Each bin size is 10 min on the x-axis, and values on the graph represent the maximum of the bin. The sample-set has a mean in the 360 min bin and contributes to 17.5% of the population. There is a standard deviation of ±30 min. The minimum appears at 300 min bin. There is a single outlier at the 560 min bin. There is also a longer tail in the distribution for durations greater than 350 min, with a maximum occuring in the 480 min bin.

4.3 Draw Replacement

The element operations and the associated state durations for the draw replacement events associated to the heat recovery of four scenarios are examined in this section: (1) 50 ℓ low flow (in *Section 4.3.1*), (2) 50 ℓ high flow (in *Section 4.3.2*), (3) 100 ℓ low flow (in *Section 4.3.3*) and (4) 100 ℓ high flow (in *Section 4.3.4*). The summary on the characterisation of draw replacement element events is discussed in *Section 4.3.5*.

4.3.1 Characterise 50-Litre Draw: Low Flow

Three sets of tests are performed on a 50 ℓ draw at low flow (approx. 8 ℓ/min) and the measured results from the heat replacement activity of the element are presented in *Figure 4.5*. Tests were performed in the same season of the year with the same flow-control valve setting, but the test samples varied in the following manner:

- Sample 1 with flow rate (6.2 ℓ/min), average ambient temperature (26.9°C)

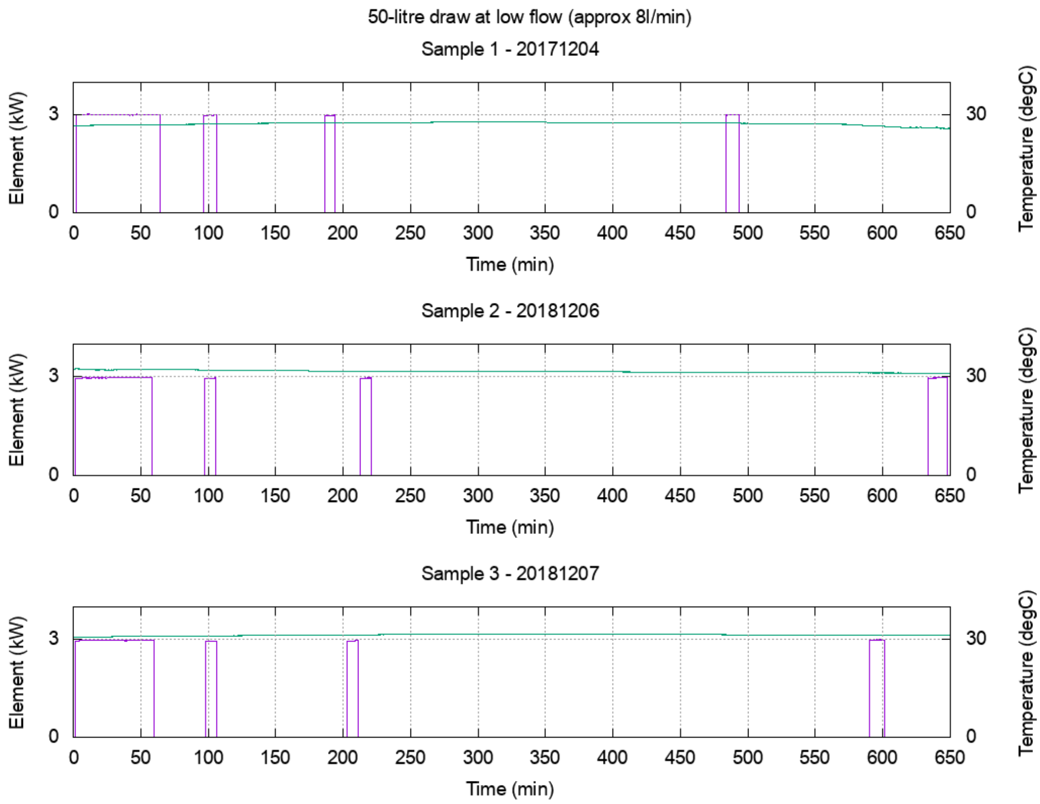

Figure 4.5: Measured element activity due to draw event of $50\,\ell$ at low flow (approx. $8\,\ell$/min) with accompanying ambient temperatures measured during each experiment.

- Sample 2 with flow rate ($9.0\,\ell$/min), average ambient temperature (31.5°C)
- Sample 3 with flow rate ($8.5\,\ell$/min), average ambient temperature (30.4°C)

By visual inspection of *Figure 4.5*, it can be seen that the primary heat replacement event (t_{ON_1}) has a duration of approximately 60 min with the first subsequent element event (t_{ON_2}) occuring at approximatley 100 min and the second subsequent replacement (t_{ON_3}) occuring at approximately 200 min. These three element events are considered the draw replacement events due to heat recovery of the tank, and appear to be quite consistent over the three datasets. The final element event in each sample (t_{ON_4}) is widely spaced from the draw replacement events and it appears to form part of steady-state operation.

The times that the element is in OFF state are labeled according to the preceeding ON event. Therefore, t_{OFF_1} is the period of time between events t_{ON_1} and t_{ON_2}. The variation on this time is dependant on the ambient temperature of each set of results; the higher the ambient temperature, the longer the duration. Each element

Table 4.1: Comparison of three samples of measured element event time comparisons for 50 ℓ draw at low flow (approx. 8 ℓ/min). All values expressed in minutes.

Element event	**Sample 1 (min)**		**Sample 2 (min)**		**Sample 3 (min)**	
	Start	t_D	**Start**	t_D	**Start**	t_D
ON_1	0	62.22	0	57.05	0	58.63
OFF_1	62.22	32.22	57.05	38.45	58.63	37.83
ON_2	94.43	9.8	95.5	8.65	96.47	8.38
OFF_2	104.23	80.08	104.15	106.75	104.85	96.4
ON_3	184.32	7.6	210.9	8.25	201.25	8.33
OFF_3	191.92	289.45	219.15	412.73	209.58	378.9
ON_4	481.37	10.13	631.88	14.1	588.48	11.45
OFF_4	491.5	331.15	645.98	406.42	599.93	353.48
ON_5	822.65	13.57	1 052.4	14.93	953.42	14.4

Table 4.2: Error margins determined for energy replacement of element activity for three samples of a 50 ℓ draw at low flow (approx. 8 ℓ/min). All values expressed in minutes.

Element Event	**Mean Average**	**Abs Max Error**	**Max Error (%)**
t_{ON_1}	59.3	2.92	4.92
t_{OFF_1}	36.17	3.95	10.92
t_{ON_2}	8.94	0.86	9.57
t_{OFF_2}	94.41	14.33	15.18
t_{ON_3}	8.06	0.46	5.72
t_{OFF_3}	360.36	70.91	19.68
t_{ON_4}	11.89	2.21	18.54
t_{OFF_4}	363.68	42.73	11.75
t_{ON_5}	14.3	0.73	5.13

event has an associated starting time and duration (t_D), as referenced in *Table 4.1*. Time of occurrance is dependant on the states that preceed it, and therefore cannot be easily characterised; although it is used for visual inspection. Therefore, the variation on each event will be considered for its duration. *Table 4.1* shows the times the element changes state (which can be matched to x-axis times presented in *Figure 4.5*) and the duration that the element is in each state (t_D).

The times in each state are averaged for each sample and the maximum error margin is determined and presented in *Table 4.2* as an absolute variation and a percentage of the average. The primary energy replacement event (t_{ON_1}) has an average duration of $59.30 \pm 4.92\%$ min. The element switches off and enters state (t_{OFF_1}) with an average duration of $36.17 \pm 10.92\%$ min. The first subsequent element replacement (t_{ON_2}) has an average duration of $8.94 \pm 9.57\%$ min, which is a lower duration than the steady-state durations with a mean of 15 min. The next cooling state (t_{OFF_2}) has an average duration of $94.41 \pm 15.18\%$ min, which is well below the duration of a steady-state cooling cycle with a mean of 350 min. The second subsequent element replacement (t_{ON_3}) has an average duration of $8.06 \pm 5.72\%$ min, which is very similar to the average duration of t_{ON_1}. The next cooling state (t_{OFF_3}) has an average duration of $360.36 \pm 19.68\%$ min, which is well within range of normal steady-state durations. The third subsequent element replacement (t_{ON_4}) can be classified as part of the replacement cycle or the steady-state, as its average duration is $11.89 \pm 18.54\%$ min, which matches an outlier in the steady-state dataset at approximately 11 min. Thereafter, definitive steady-state durations are observed in t_{OFF_4} with an average duration of $363.68 \pm 11.75\%$ min and t_{ON_5} with an average duration of $14.30 \pm 5.13\%$ min. These two events are not fully represented in *Figure 4.5* due to the length of time, but are included to show when steady-state occurs.

Therefore, the heat replacement element events can be characterised with a high degree of accuracy for the first three element events. The model will need to account for this element switching activity as a success criteria.

4.3.2 Characterise 50-Litre Draw: High Flow

Three sets of tests are performed on a 50 ℓ draw at a high flow rate (approx. 30 ℓ/min) and the measured results from the heat replacement activity of the element are presented in *Figure 4.6*. Tests were performed in the same season of the year (summer) with the same flow-control valve setting, but the test samples varied in the following manner:

- Sample 1 with flow rate (30.0 ℓ/min), average ambient temperature (28.8°C)
- Sample 2 with flow rate (30.0 ℓ/min), average ambient temperature (31.2°C)

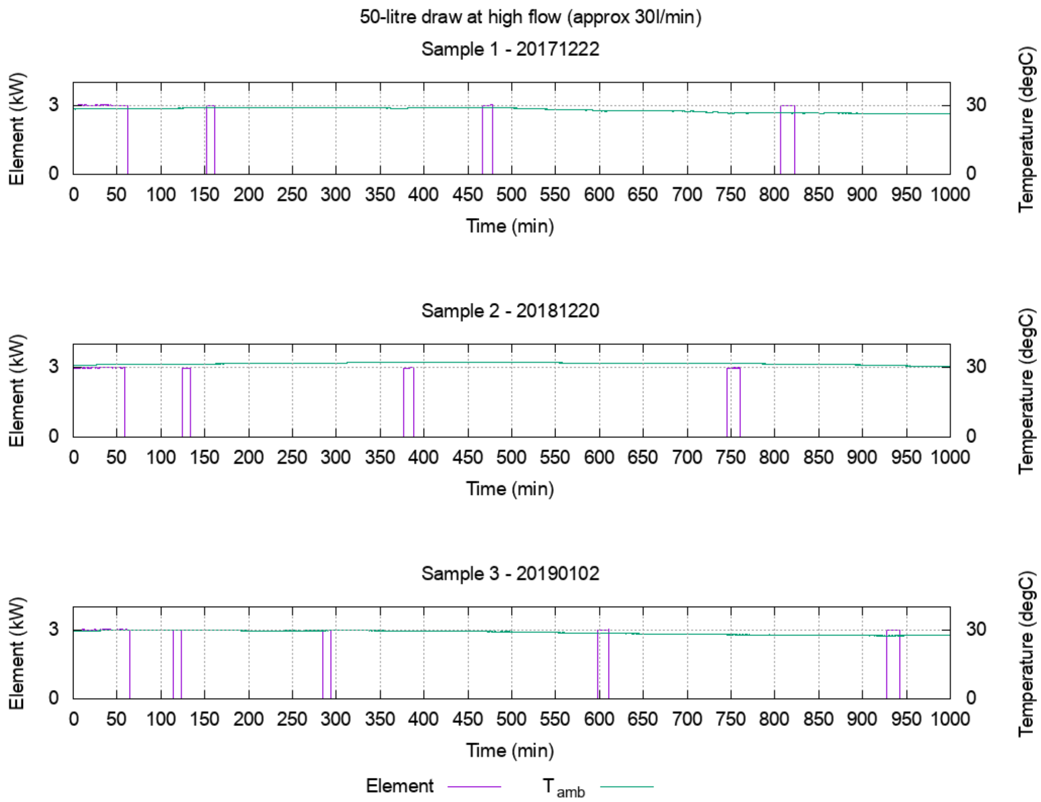

Figure 4.6: Measured element activity due to draw event of $50\,\ell$ at high flow (approx. $30\,\ell$/min) with accompanying ambient temperatures measured during each experiment.

- Sample 3 with flow rate ($30.0\,\ell$/min), average ambient temperature (29.1°C)

By visual inspection of *Figure 4.6*, it can be seen that the primary heat replacement event (t_{ON_1}) has a duration of approximately 60 min (but longer than the experiments with the same draw volume at low flow rate). The first subsequent element event (t_{ON_2}) occurs at approximatley $110-150$ min and the start of the second subsequent replacement (t_{ON_3}) has a large range of approximately $280-460$ min. As with the previous measured samples at different experimental conditions, these three element events are considered the draw replacement events for heat recovery, although Sample 1 appears to have entered steady-state earlier at t_{OFF_3}. The next element event in each sample (t_{ON_4}) is widely spaced from the draw replacement events and occurs in the range of $600-810$ min, steady-state for all samples. Sample 3 has an additional element event displayed (t_{ON_5}) just before 950 min.

Table 4.3 shows the times the element changes state (which can be matched to x-axis times presented in *Figure 4.6*) and the duration that the element is in each

Table 4.3: Comparison of three samples of measured element event time comparisons for 50 ℓ draw at high flow rate (approx. 30 ℓ/min). All values expressed in minutes.

Element	**Sample 1 (min)**		**Sample 2 (min)**		**Sample 3 (min)**	
event	**Start**	t_D	**Start**	t_D	**Start**	t_D
ON_1	0	61.95	0	58.33	0	63.72
OFF_1	61.95	89.68	58.33	65.68	63.72	50.15
ON_2	151.63	9.47	124.02	8.8	113.87	8.83
OFF_2	161.1	305.33	132.82	243.82	122.7	162.05
ON_3	466.43	11.55	376.63	11.05	284.75	8.97
OFF_3	477.98	328.17	387.68	357.85	293.72	304.12
ON_4	806.15	15.68	745.53	14.05	597.83	12.92
OFF_4	821.83	368.18	759.58	346.72	610.75	316.03
ON_5	1 190.02	15.72	1 106.3	14.92	926.78	14.85

Table 4.4: Error margins determined for heat replacement of element activity for three samples of a 50 ℓ draw at high flow (approx. 30 ℓ/min). All values expressed in minutes.

Element Event	**Mean Average**	**Abs Max Error**	**Max Error (%)**
t_{ON_1}	61.33	2.38	3.89
t_{OFF_1}	68.51	21.18	30.91
t_{ON_2}	9.03	0.43	4.8
t_{OFF_2}	237.07	68.27	28.8
t_{ON_3}	10.52	1.03	9.77
t_{OFF_3}	330.04	27.81	8.42
t_{ON_4}	14.22	1.47	10.32
t_{OFF_4}	343.64	24.54	7.14
t_{ON_5}	15.16	0.56	3.66

state (Δt). The times in each state are averaged for each sample and the maximum error margin is determined and presented in *Table 4.4* as an absolute variation and a percentage of the average. The primary heat replacement event (t_{ON_1}) has an average duration of $61.33 \pm 3.89\%$ min. The element switches off and enters state

t_{OFF_1} with an average duration of $68.51 \pm 30.91\%$ min. This large error is due to Sample 1 duration of 89.68 min which is out of range of Sample 2 and Sample 3. The first subsequent element replacement (t_{ON_2}) has an average duration of $9.03 \pm 4.80\%$ min, which is a lower duration than the steady-state durations with a mean of 15 min. The next cooling state (t_{OFF_2}) has an average duration of $237.07 \pm 28.8\%$ min, which is shorter than the duration of a steady-state cooling cycle with a mean of 350 min. This large error margin is due to Sample 1 entering steady-state early as previously discussed. The second subsequent element replacement (t_{ON_3}) has an average duration of $10.52 \pm 9.77\%$ min, which is not quite a steady-state event. The next cooling state (t_{OFF_3}) has an average duration of $330.04 \pm 8.42\%$ min, which defines the beginning of steady-state. The third subsequent element replacement (t_{ON_4}) demonstrates the first steady-state element cycle with an average duration of $14.22 \pm 10.32\%$ min. Thereafter, t_{OFF_4} has an average duration of $343.64 \pm 7.14\%$ min and t_{ON_5} with an average duration of $15.16 \pm 7.14\%$ min. The last element event is not fully represented in *Figure 4.8* due to the length of time for Sample 1 and Sample 2, but are included for completeness.

4.3.3 Characterise 100-Litre Draw: Low Flow

Three sets of tests are performed on a $100\,\ell$ draw at low flow (approx. $8\,\ell$/min) and the measured results from the heat replacement activity of the element are presented in *Figure 4.7*. Tests were performed in the same season of the year with the same flow-control valve setting, but the test samples varied in the following manner:

- Sample 1 with flow rate ($6.4\,\ell$/min), average ambient temperature (24.5°C)
- Sample 2 with flow rate ($8.9\,\ell$/min), average ambient temperature (25.4°C)
- Sample 3 with flow rate ($8.6\,\ell$/min), average ambient temperature (30.6°C)

By visual inspection of *Figure 4.7*, it can be seen that the primary heat replacement event (t_{ON_1}) has a duration of approximately 120 min with the first subsequent element event (t_{ON_2}) occuring just before 200 min and the second subsequent replacement (t_{ON_3}) occuring with high variation in the three samples around 400 min. The variation in these three t_{ON_3} events could be accounted for by difference in ambient temperatures. The final element event in each sample (t_{ON_4}) is widely spaced from the draw replacement events in the region of $650 - 800$ min.

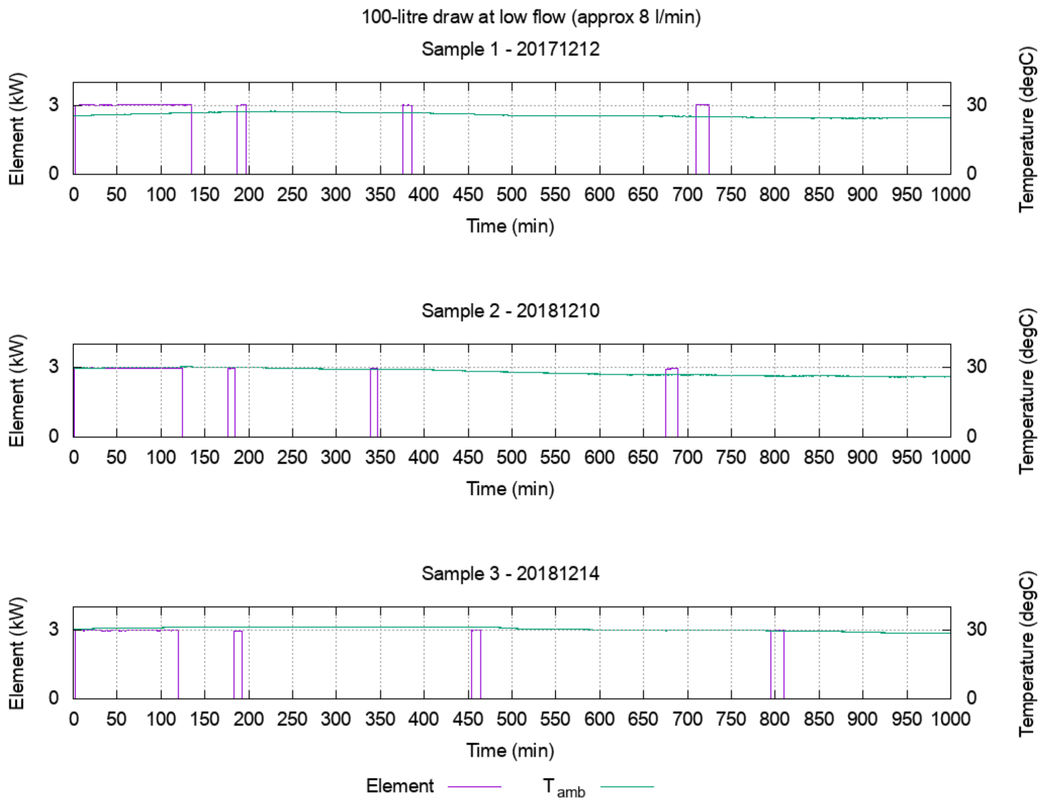

Figure 4.7: Measured element activity due to draw event of 100, ℓ at low flow (approx. 8 ℓ/min) with accompanying ambient temperatures measured during each experiment.

Table 4.5 shows the times the element changes state (which can be matched to x-axis times presented in *Figure 4.7*) and the duration that the element is in each state (Δt). The times in each state are averaged for each sample and the maximum error margin is determined and presented in *Table 4.6* as an absolute variation and a percentage of the average. The primary heat replacement event (t_{ON_1}) has an average duration of $124.43 \pm 6.84\%$ min. The element switches off and enters state t_{OFF_1} with an average duration of $55.68 \pm 15.38\%$ min. The first subsequent element replacement (t_{ON_2}) has an average duration of $9.35 \pm 8.91\%$ min, which is a lower duration than the steady-state durations with a mean of 15 min. The next cooling state (t_{OFF_2}) has an average duration of $198.21 \pm 32.01\%$ min, which is well below the duration of a steady-state cooling cycle with a mean of 350 min. The second subsequent element replacement (t_{ON_3}) has an average duration of $9.45 \pm 4.94\%$ min, which is very similar to the average duration of t_{ON_1}. The next cooling state (t_{OFF_3}) has an average duration of $327.57 \pm 1.1\%$ min, which is well within range of normal steady-state durations and a very low variation. The third subsequent element replacement (t_{ON_4}) can be classified as steady-state, as

Table 4.5: Comparison of three samples of measured element event time comparisons for 100 ℓ draw at low flow (approx. 8 ℓ/min). All values expressed in minutes.

Element event	**Sample 1 (min)**		**Sample 2 (min)**		**Sample 3 (min)**	
	Start	t_D	**Start**	t_D	**Start**	t_D
ON_1	0	132.95	0	122.87	0	117.48
OFF_1	132.95	51.38	122.87	51.42	117.48	64.25
ON_2	184.33	10.18	174.28	8.88	181.73	8.98
OFF_2	194.52	179.52	183.17	153.45	190.72	261.65
ON_3	374.03	9.35	336.62	9.08	452.37	9.92
OFF_3	383.38	323.97	345.7	327.97	462.28	330.77
ON_4	707.35	14.8	673.67	13.7	793.05	15.45
OFF_4	722.15	361.23	687.37	336.25	808.5	393.32
ON_5	1 083.38	18.28	1 023.62	14.93	1 201.82	15.35

Table 4.6: Error margins determined for heat replacement of element activity for three samples of a 100 ℓ draw at low flow (approx. 8 ℓ/min). All values expressed in minutes.

Element Event	**Mean Average**	**Abs Max Error**	**Max Error (%)**
t_{ON_1}	124.43	8.52	6.84
t_{OFF_1}	55.68	8.57	15.38
t_{ON_2}	9.35	0.83	8.91
t_{OFF_2}	198.21	63.44	32.01
t_{ON_3}	9.45	0.47	4.94
t_{OFF_3}	327.57	3.6	1.1
t_{ON_4}	14.65	0.8	5.46
t_{OFF_4}	363.6	29.72	8.17
t_{ON_5}	16.19	2.09	12.94

its average duration is $14.65 \pm 5.46\%$ min, although Sample 3 falls just under the steady-state classification. Thereafter, definitive steady-state durations are observed in t_{OFF_4} with an average duration of $363.68 \pm 8.17\%$ min and t_{ON_5} with an average duration of $16.19 \pm 12.94\%$ min. These two events are not fully represented in

Figure 4.7 due to the length of time, but are included to show when steady-state occurs.

4.3.4 Characterise 100-Litre Draw: High Flow

Three sets of tests are performed on a $100\,\ell$ draw at a high flow rate (approx. $30\,\ell$/min) and the measured results from the heat replacement activity of the element are presented in *Figure 4.8*. Tests were performed in the same season of the year with the same flow-control valve setting, but the test samples varied in the following manner:

- Sample 1 with flow rate ($30.0\,\ell$/min), average ambient temperature (28.8°C)
- Sample 2 with flow rate ($29.9\,\ell$/min), average ambient temperature (31.0°C)
- Sample 3 with flow rate ($30.0\,\ell$/min), average ambient temperature (31.6°C)

By visual inspection of *Figure 4.8*, it can be seen that the primary energy replacement event (t_{ON_1}) has a duration of approximately 120 min (but shorter than the experiments with the same drawn volume with low flow rate). The first subsequent element event (t_{ON_2}) occurs at approximatley 200 min and the second subsequent replacement (t_{ON_3}) occuring in the range of $450 - 500$ min. These three element events are considered the draw replacement events from the draw event, and appear to be quite consistent over the three datasets. Sample 1 has lower ambient temperatures and could account for the closer grouping of element events t_{ON_2} and t_{ON_3}. The final element event in each sample (t_{ON_4}) is widely spaced from the draw replacement events and consistently in the range of $850 - 900$ min.

Table 4.7 shows the times the element changes state (which can be matched to x-axis times presented in *Figure 4.8*) and the duration that the element is in each state (Δt). The times in each state are averaged for each sample and the maximum error margin is determined and presented in *Table 4.8* as an absolute variation and a percentage of the average. The primary heat replacement event (t_{ON_1}) has an average duration of $114.32 \pm 0.6\%$ min. The element switches off and enters state t_{OFF_1} with an average duration of $70.93 \pm 16.16\%$ min. The first subsequent element replacement (t_{ON_2}) has an average duration of $9.94 \pm 6.59\%$ min, which is a lower duration than the steady-state durations with a mean of 15 min. The next cooling state (t_{OFF_2}) has an average duration of $278.63 \pm 11.50\%$ min, which is shorter than the duration

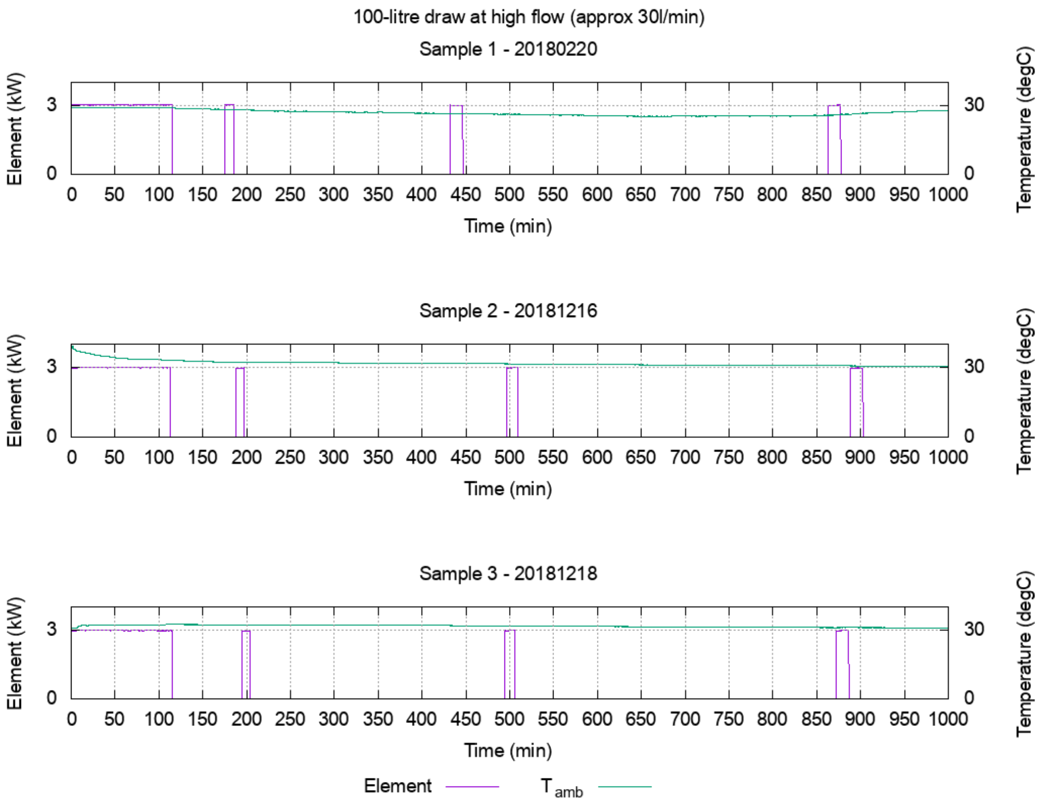

Figure 4.8: Measured element activity due to draw event of 100 ℓ at high flow (approx. 30 ℓ/min) with accompanying ambient temperatures measured during each experiment.

of a steady-state cooling cycle with a mean of 350 min. The second subsequent element replacement (t_{ON_3}) has an average duration of $13.01 \pm 10.21\%$ min, which cannot be characterised as a steady-state event. The next cooling state (t_{OFF_3}) has an average duration of $387.17 \pm 7.59\%$ min, which is defines the beginning of steady-state. The third subsequent element replacement (t_{ON_4}) demonstrates the first steady-state element cycle with an average duration of $14.46 \pm 1.11\%$ min, with a very low variation on the duration. Thereafter, t_{OFF_4} has an average duration of $360.61 \pm 3.13\%$ min and t_{ON_5} with an average duration of $14.62 \pm 5.32\%$ min. These last two events are not fully represented in *Figure 4.8* due to the length of time, but are included to show when steady-state occurs.

4.3.5 Characterisation Summary

The summarised variations of each element state for each of the draw scenarios is provided in *Figure 4.9*. The results from the three tests in each scenario is

Table 4.7: Comparison of three samples of measured element event time comparisons for 100 ℓ draw at high flow rate (approx. 30 ℓ/min) from *Figure 4.8 (a), (b) and (c).* All values expressed in minutes.

Element event	**Sample 1 (min)**		**Sample 2 (min)**		**Sample 3 (min)**	
	Start	t_D	**Start**	t_D	**Start**	t_D
ON_1	0	115	0	112.95	0	115
OFF_1	115	59.47	112.95	74.33	115	78.98
ON_2	174.47	10.6	187.28	9.67	193.98	9.57
OFF_2	185.07	246.58	196.95	299.28	203.55	290.02
ON_3	431.65	14.33	496.23	12.37	493.57	12.32
OFF_3	445.98	416.57	508.6	379.12	505.88	365.82
ON_4	862.55	14.3	887.72	14.58	871.7	14.5
OFF_4	876.85	351.72	902.3	371.9	886.2	358.2
ON_5	1 228.57	15.4	1 274.2	13.92	1 244.4	14.55

Table 4.8: Error margins determined for heat replacement of element activity for three samples of a 100 ℓ draw at high flow (approx. 30 ℓ/min) from *Table 4.7.* All values expressed in minutes.

Element Event	**Mean Average**	**Abs Max Error**	**Max Error (%)**
t_{ON_1}	114.32	0.68	0.6
t_{OFF_1}	70.93	11.46	16.16
t_{ON_2}	9.94	0.66	6.59
t_{OFF_2}	278.63	32.04	11.5
t_{ON_3}	13.01	1.33	10.21
t_{OFF_3}	387.17	29.4	7.59
t_{ON_4}	14.46	0.16	1.11
t_{OFF_4}	360.61	11.29	3.13
t_{ON_5}	14.62	0.78	5.32

represented by each point with error bars. The middle line represents the mean of the three tests and the upper and lower lines represent the absolute maximum error.

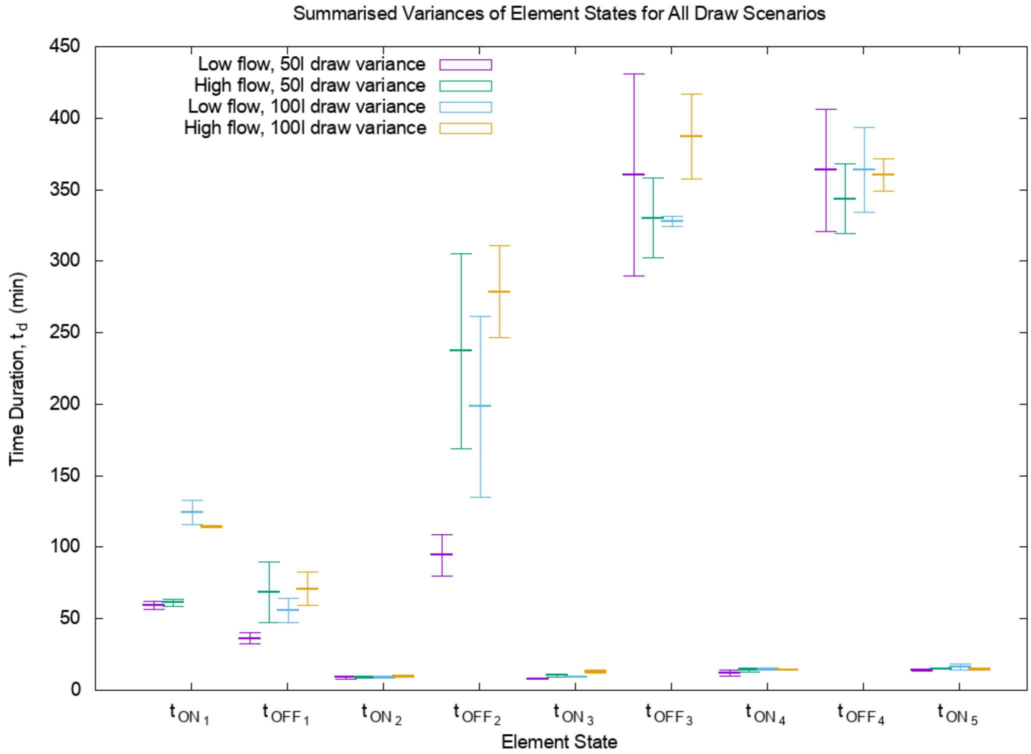

Figure 4.9: Summarised variances of each element state for each draw scenario.

Primary Replacement Event

The primary replacement event, t_{ON_1}, is the first element event that occurs due to a draw event. It occurs due to the changing temperature measured at the thermostat layer which triggers the element to switch to ON state.

For the $50\,\ell$ draw events (low flow rate and high flow rate), the durations of t_{ON_1} range between $57.05 - 63.72$ min, which is a very small range of values. This is indicated by the very small error bars in *Figure 4.9*. The high flow rate has a slightly higher set of values than the low flow rate, but more experiments would need to be performed to confirm if this is consistent. With the 3 kW element in ON state for the upper a lower durations, it equates to $2.9 - 3.2$ kWh of heat entering the system. If considering the ideal case for an EWH, where $50\,\ell$ is drawn at 70°C and inlet is 20°C, the heat energy drawn out is 2.9 kWh. This means the primary replacement accounts for $97.8 - 109.2\%$ of the ideal energy drawn.

For the $100\,\ell$ draw events (low and high flow rate), the durations of t_{ON_1} range between $112.95 - 132.95$ min, which is approximately double the duration of the $50\,\ell$ draws. The range of values is also much larger than the $50\,\ell$ draws. This large range is due to the low flow events, whereas the high flow rate events have a very small range. In contrast to the 50 ℓ draws, the low flow rate events appear to have overall higher durations in the primary replacement than the high flow rate. More experiments would need to be run to confirm this. With the 3 kW element in ON state for the upper a lower durations, it equates to $5.6 - 6.6$ kWh of heat entering the system. If considering the ideal case for an EWH, where 100 ℓ is drawn at 70°C and inlet is 20°C, the heat energy drawn out is 5.8 kWh. This means the primary replacement accounts for $96.8 - 113.9\%$ of the ideal energy drawn.

For both volumetric draws, approximately 100% of the energy is replaced in the primary replacement event. This is surprising, as it was expected to be less than the ideal case. However, there are regions of the tank that run hotter than others, indicating a greater temperature gradient, where upper regions appear hotter than lower regions. This could result in a delayed distribution of heat, which could account for requirement for the subsequent events.

Subsequent Replacement Events

The subsequent replacement events are the element ON events that occur after the primary replacement but preceed the steady-state events. For the purpose of this discussion, the OFF element events will also be discussed here. All the test scenarios at least have one subsequent element ON event (linked with its preceding OFF event), i.e. t_{ON_2} is preceded by t_{OFF_1}.

Subsequent replacement events are easily defined by checking that the OFF element events are not within range of the steady-state counterparts (defined in *Section 4.2.1*). More specifically, the durations for OFF element events for draw replacement can be defined as less than the durations of steady-state OFF events. While it is not discernible in *Figure 4.9*, the subsequent replacement ON events can also be used for characterisation since they have a shorter durations than the ON events for steady-state.

In all draw scenarios, there is definitely one set of subsequent replacement events t_{OFF_1} and t_{ON_2}, which all have durations lower than steady-state counterparts. A second subsequent event (t_{OFF_2} and $t_{ON_3} <$ steady-state values) was only guaranteed in the low flow scenarios (both 50 ℓ and 100 ℓ), whereas the high flow scenarios had some tests with a second subsequent event and others that entered steady-state earlier. By the t_{OFF_3} event, all scenarios have either reached or are very close to reaching steady-state values.

This means that there are processes inside the tank that govern the movement of heat in the tank that cannot be controlled through ambient temperature, draw volume and flow rate and to result in deterministic element ON/OFF durations. This is out of scope of this work and requires a deeper examination, either into the temperatures measured in correlation to element durations, greater control of experimental parameters or with a larger sample size.

4.4 Conclusion

In this chapter, the durations of the element state changes due to steady-state tank operation and draw replacement are defined to allow for differentiation of tank modes. The steady-state events for the element in ON state has a mean of 15 min, with a minimum of 14 min and a maximum of 19 min (outliers have been ignored). The duration for element in OFF state for steady-state has a mean of 350 minutes.

Four draw scenarios have been administered with three test instances presented for each scenario: 50 ℓ draw low flowrate, 50 ℓ draw high flowrate, 100 ℓ draw low flowrate and 100 ℓ draw high flowrate. It was found that the element operations for draw replacement can be defined as durations lower than the steady-state counterparts. The durations for the element in ON state, t_{ON}, have lower variations than the element in OFF state, t_{OFF}. The largest variations occur in element state t_{OFF_2}. The large variations in the durations means for each of these tests show that there is still much that needs to be done to properly characterise draw replacements in a horizontal tank.

Chapter 5

Model Development

This chapter covers the development of a thermal and load model for a horizontally oriented EWH and is introduced in *Section 5.1*. The sizing and calculation of the parameters of the layer segments is presented in *Section 5.2*. The heat transfer processes that govern the interaction of the layers are discussed in *Section 5.3*. The operational states of the tank that determine how the heat transfer processes act on each of the layers in presented in *Section 5.4*. A set of heat transfer parameters are introduced in *Section 5.5* using the control draw scenario. A discussion on model considerations for buoyancy, mixing and layers choice is presented in *Section 5.6*.

5.1 Introduction

A 1D multi-node model is chosen to reproduce the thermal stratification that occurs in the tank of a horizontally oriented EWH to resolve transient switching events due to heat recovery. The model is discretised in space (layered geometry of body of water) and time (based on time-steps). The volume of water is divided into multiple nodes that will allow for the simulation of discrete layers for thermal stratification, which is discussed further in *Section 5.2*.

The tank has three distinct states: heating, cooling and draw, which the model will emulate. In each state, there are different heat and mass transfer processes, happening between the environment and layers for each time step. *Figure 5.1* shows the basic logic required for tank state switching due to the thermoprobe layer, T_t in relation to the upper hysteresis limit, T_{hyst_U} and lower hysteresis limit, T_{hyst_L}.

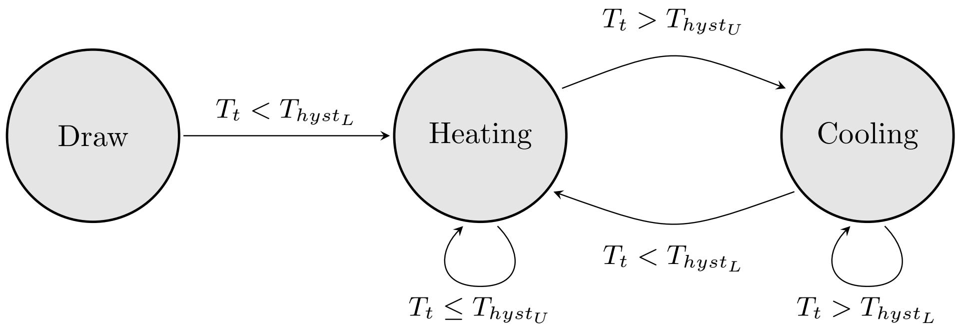

Figure 5.1: Basic logic and changing of states for the model.

Key assumptions made for the model are as follows:

- Each node mixes at the end of each timestep, i.e. is associated with a single temperature.
- Nodes are modelled as solid masses.
- Thermal insulation on the tank is constant on all tank boundaries.
- Flow rates are constant.
- Ambient temperature is constant.
- Inlet temperature is constant.
- Hysteresis switching temperatures, T_{hyst_U} and T_{hyst_L} are constant.
- Water density is constant.
- Element efficiency is 100%.

The following sections detail the layer segment geometries, heat transfer processes that act on each layer and the tank operational states that combine the heat transfer processes. Thereafter, the model is determined with a set of heat transfer parameters trained from a control draw scenario and results are presented for all draw scenarios for model validation.

5.2 Layer Segment Geometries

The layer configurations are designed using the temperature sensor string as a base, since the ability to compare with sensor locations is useful in the validation process.

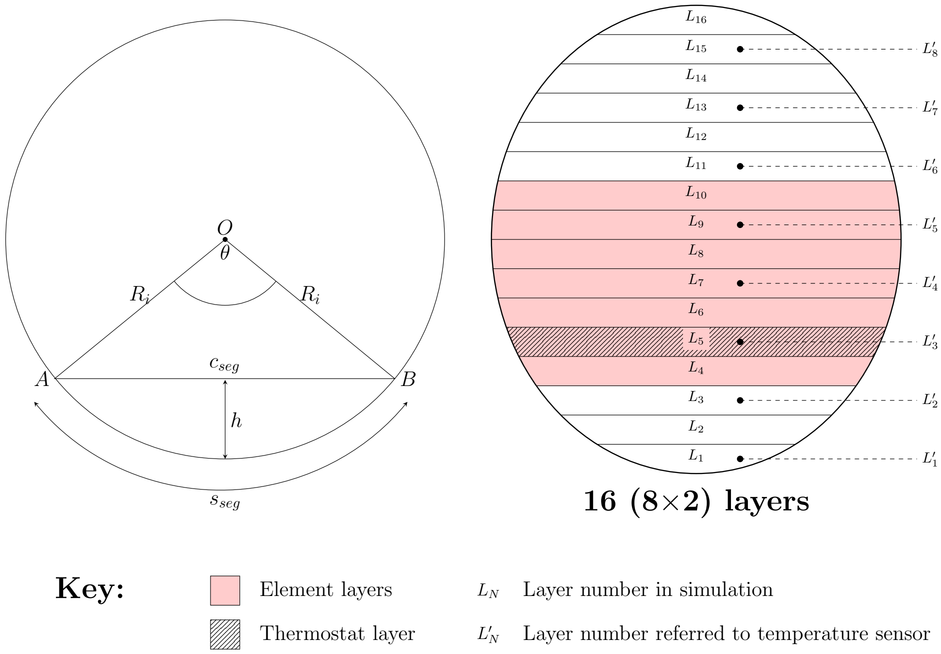

Figure 5.2: Modelling considerations for geometries. Chords and segments considered for layer geometries (left). Example of 16-layer structure with highlighted element layers and thermostat layer.

There are eight sensors that are placed at fixed heights on the temperature sensor string. Therefore, fixed height layers will be used, and the total number of layers should be a multiple of eight for easy comparison of simulated temperatures to measured values. As discussed in *Section 3.4*, a total of 24 simulated layers are chosen.

Each layer has defined the following attributes:

- volume,
- boundary between layers,
- boundary with environment and
- starting temperature.

The volume and temperature determines the stored heat energy in the layer. The boundaries (or areas of interaction) between layers and environment contribute towards the heat transfer rate of the layer. The physical attributes of the layer, volume and boundaries are determined geometrically by abstracting the tank in

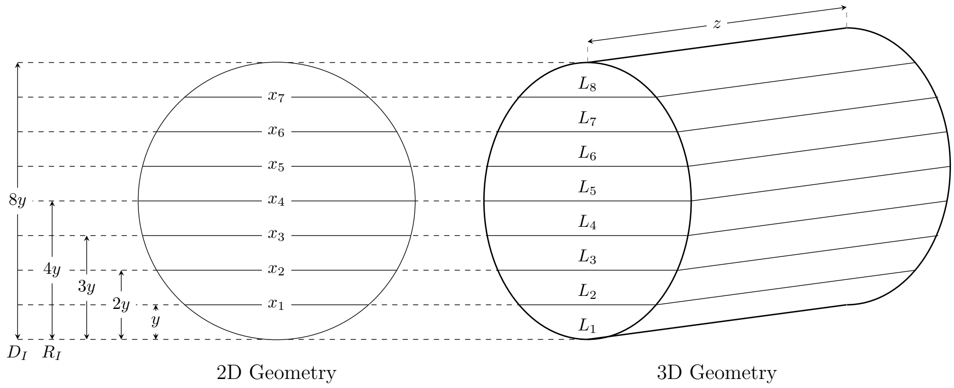

Figure 5.3: Layer segmentation on 2D geometry of circular plane and 3D geometry for cylinder.

a 2D geometry by observing circular plane, as shown in *Figure 5.3*. A detailed example calculation is presented in *Appendix C.2* for an 8-layer configuration. The method can be easily extended for a total number of layers where N is even; small modifications need to be made for N is odd numbered.

The general logic of the physical attributes of the layer is briefly discussed. *Section 5.2.1* presents the calculation steps for the surface areas of layer boundaries.

5.2.1 Boundaries Between Layers

Determine the equi-distant height of each layer, y, by dividing the inner diameter, D_I, by the chosen total number of layers, N, as shown in *Equation 5.1.* At each layer height, y, a horizontal chord can be draw from one end of the circle to the other, denoted as x_1, x_2,.., x_7. Each horizontal chord subtends the center of the circle by an angle, θ. The angle θ_1 for chord x_1 can be found by *Equation 5.2.* The length of the chords can be determined by simplifying the geometry through symmetry and solving with trigonometric relationships, as shown in *Equation 5.3* for chord x_1.

$$y = \frac{D_I}{N} = \frac{2R_I}{N} \tag{5.1}$$

$$\theta_1 = arccos\left(\frac{R_I - y}{R_I}\right) \tag{5.2}$$

$$x_1 = 2R_I sin\theta_1 \tag{5.3}$$

$$A_{12} = x_1\, z \tag{5.4}$$

These chords represent the 1D boundaries between layers, and should be multiplied by the inner length of the tank, z to produce the surface area of the boundary. *Equation 5.4* shows the surface area of the chord, A_{12} for the boundary between Layer 1 and Layer 2.

5.2.2 Boundary Between Layer and Environment

Each angle θ subtending a chord, x, also subtends a line segment of the circle boundary, s. The length of the line segment s is given by *Equation 5.5* with segment s_1 subtended by angle θ_1 as an example. The length of the next layer line segment, s_2 is determined using θ_2, as shown in *Equation 5.6*, where the line segment s_1 is subtracted.

$$s_1 = \frac{\pi}{180}\,\theta_1\, R_I \tag{5.5}$$

$$s_2 = \frac{\pi}{180}\,\theta_2\, R_I - s_1 \tag{5.6}$$

$$A_{1-a} = s_1\, z \tag{5.7}$$

The surface area of the layer boundary facing the environment, denoted A_{1-a}, is determined by multiplying the associated line segment, s_1 with the inner length of the tank, z as shown in *Equation 5.7*.

5.2.3 Layer Volume

The area of the layer on the circular plane is determined by the segment area encased from the chord to the line segment subtended by θ. The area of the segment on the circular plane for Layer 1, A_1 is determined by *Equation 5.8*. Similar to the line segment calculations for the boundary to the environment in *Section 5.2.2*, the area of Layer 2, A_2 should subtract the area A_1, as shown in *Equation 5.9*.

$$A_1 = \frac{R_i^2}{2}\left(\frac{\pi}{180}\,\theta_1 - sin\theta_1\right) \tag{5.8}$$

$$A_2 = \frac{R_i^2}{2}\left(\frac{\pi}{180}\,\theta_2 - sin\theta_2\right) - A_1 \tag{5.9}$$

$$V_1 = A_1\, z \tag{5.10}$$

The volume of the layer is then determined by multiplying the area of the segment on the circular plane to the inner length of the tank. An example is shown in *Equation 5.10*, where V_1 is the volume of Layer 1.

5.2.4 Starting Temperatures

In the case where the number of sensors is not equal to the number of layers in the simulation, the starting temperatures of each layer needs to be determined. If there is no direct reference to a temperature sensor and a simulated layer at a specific height, a linear relationship is determined from the temperature sensors on either side of the layer with relation to its location from each sensor.

Figure 5.4 shows how the starting, temperatures from Sensors $T_1 - T_8$ are processed to gradients $g_{12} - g_{78}$ for a 32-layer configuration of interpolated layer temperatures $L_1 - L_{32}$. This is discussed in more detail in *Appendix C.2.2*.

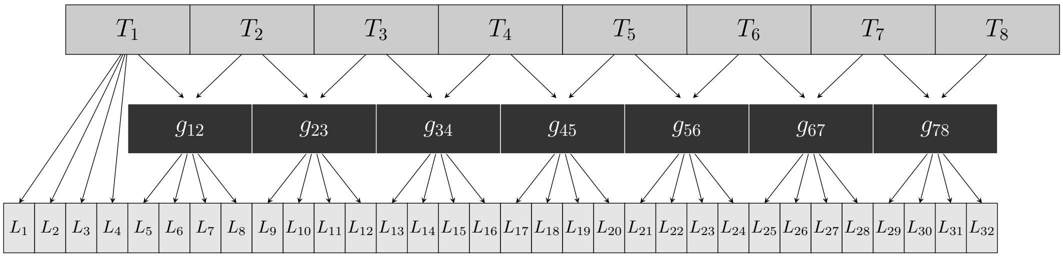

Figure 5.4: Interpolation of 32 layer model to infer initial temperatures from eight sensor temperatures.

5.3 Heat Transfer and Processes

Each layer has an initial energy content, which is defined by its stored temperature. The transfer of energy occurs through either heat or mass transfer processes, thereby changing the temperature of each layer in each pre-defined time-step. Heat and mass transfer occurs from layer-to-layer and layer-to-environment and occurs in three different operational states, discussed in *Section 5.4*.

These processes are used in the model based on its state to determine the energy exchange between layers and the environment to predict layer temperatures at each time step.

5.3.1 Heat Energy Content Per Layer

The energy content stored in each layer, E_j is defined by its volume, V_j, and its temperature, T_j, compared to a reference temperature, T_{ref}. The density of water, ρ, is assumed to be constant at $1\,000$ kg/m^3, and the specific heat of water c_p is assigned a value of $4.2\,\text{kJ/(kg.°C)}$.

$$E_j = \rho c_p V_j (T_j - T_{ref}) \tag{5.11}$$

Since the volume for each layer and storage material (water) is fixed, the energy content of the layer changes based on the temperature difference of the layer, ($T_j - T_{ref}$, where T_{ref} is kept constant. Therefore, changes in T_j will directly change the energy content of each layer.

The exchange of heat within each layer is defined by the heat transfer processes that act on it; which cause a change in the layer after each discrete time-step. This method assumes that energy exchange in each layer mixes perfectly. The net energy stored in the layer after a time step, denoted $E_j(k+1)$ is shown in *Equation 5.12*, where $E_j(k)$ is the energy stored in the layer before the time step, τ is the fixed time-step interval, and $Q_{j_{in}}(k)$ and $Q_{j_{out}}(k)$ are the heat transfer processes affecting the layer, defined further in *Section 5.3.2*.

$$E_j(k+1) = E_j(k) + \tau[Q_{j_{in}}(k) - Q_{j_{out}}(k)] \tag{5.12}$$

5.3.2 Heat Transfer

The basic heat transfer equation in *Equation 5.13* is used for most of the processes considered in the model; most notably, conduction between layers and conduction to the environment (or heat loss). The heat transfered is denoted with Q with a heat transfer coefficient, h, through a boundary area, A, between two temperatures on either side of the boundary; and ΔT which is the difference between the two temperatures.

$$Q = hA\Delta T \tag{5.13}$$

This is the base equation used for all heat transfer processes in the system, including layer-to-layer heat transfer under heating and cooling conditions, and layer-to-environment.

Heat transfer between layers, denoted Q_{L-L}, is defined by *Equation 5.14* where h is the heat transfer coefficient that approximates conduction of heat. This process occurs in all states, but is the dominant process in heating and cooling states. Convection that occurs due to the heat added from the element is modelled through the changing of heat transfer coefficient, h, to be replaced with h_h and h_l for different regions of the tank in the heating state. Heat transfer due to turbulent mixing is also modelled in this way, by replacing the heat transfer coefficient with h_{mix}, which occurs during a draw event.

$$Q_{L-L} = hA_{L-L}\Delta T \tag{5.14}$$

Heat loss from layer-to-environment through the tank walls and insulation, denoted Q_{L-a} is also modelled through the basic heat loss equation shown in *Equation 5.15*. Heat transfer through the tank wall has an area of A_{L-a} with a heat transfer coefficient determined by the insulation layer, U, between temperature of the layer, T_j and the ambient temperature or temperature of the environment, T_a.

$$Q_{L-a} = UA_{L-a}(T_j - T_a) \tag{5.15}$$

The final process considered, using the basic heat transfer equation is due to mass flow, which occurs when water is drawn from the tank and filled from the bottom with water from the inlet pipe. As water at a certain temperature moves through the system, it causes layer energy content to change, which affects the layer temperature.

$$Q_d = \dot{m}c_p\Delta T = qc_p(T_{upper} - T_{lower}) \tag{5.16}$$

The heat transfer from the draw event, denoted Q_d occurs through mass transfer rate, $\dot{m}$, of a medium (water), which has the heat capacity of water c_p. The equation can also be written in terms of volumetric flow rate q (ℓ/min), where 1 kg of water is approximately equivalent to 1 ℓ of water.

5.3.3 Mixing Processes

Mixing occurs through two processes: convection currents caused by the heating element, where the layers affected by the element heat up at a high rate and the heat needs to move to higher regions of the thermal storage. This is handled through heat transfer coefficients, h_{upper} and h_{mix}. The discussion for which tank states the coefficients, h_h, and h_{mix}, are applied in the model is presented in *Section 5.4.3*.

Since each layer is calculated independently, the consideration of layer buoyancy is discussed for the model. The lack of this consideration could result in temperature inversions in the layers, where layers in lower positions have higher temperatures than upper layers. This is discussed further in *Section 5.6.1*. The technique used by Rahman et al. (2016) checks the temperatures of each layer and if a lower layer has a higher temperature than the upper layer ($T_{j-1} > T_j$), the volumes mix to the same temperature using *Equation 5.17*.

$$T_j[k+1] = T_{j-1}[k+1] = \frac{V_j[k]T_j[k] + V_{j-1}[k]T_{j-1}[k]}{V_j[k] + V_{j-1}[k]} \tag{5.17}$$

5.4 Operational States

Energy transfer occurs in the system through three operational states: draw, heating (element on) and cooling (element off). These states are introduced in *Section 2.4.1*. The heating and cooling states represent the steady-state operation of the EWH and is controlled by temperature measured in the tank based on hysteresis. The draw state represents a stochastic process, which occurs as a user requires hot water service.

The model implementation for each of these states is discussed in the following subsections.

5.4.1 Model State: Draw

In the draw state, the dominant heat transfer process is through mass flow; referring to *Equation 5.16*. Each layer changes its energy content (based on its change in temperature) due to a fixed flow of water through the system.

The flow of energy for the draw state in the model is shown in *Figure 5.5*. Each layer has an initial temperature which defines its energy content. At a fixed flow rate, a time-step would have a finite volume of water moving through the system. Starting from the inlet, which has a fixed temperature, a fixed volume of water would move into Layer 1, L_1. The same fixed volume of water from Layer 1 at its current temperature will move to Layer 2, L_2 and the exchange will move through the system until the same fixed volume of water from the final layer, L_N to the outlet, where N represents the total number of layers. This occurs in a single time-step where the temperatures from each layer are exchanged in the current time step and the incoming volume of water for each layer completely mixes with the energy residing in the layer. A new temperature for the layer is established based on its new energy content and the next time step proceeds.

This energy exchange is defined in *Equation 5.12* where Q_{in} and Q_{out} are determined by *Equation 5.16*. Since inlet temperature is assumed to be constant and a generally

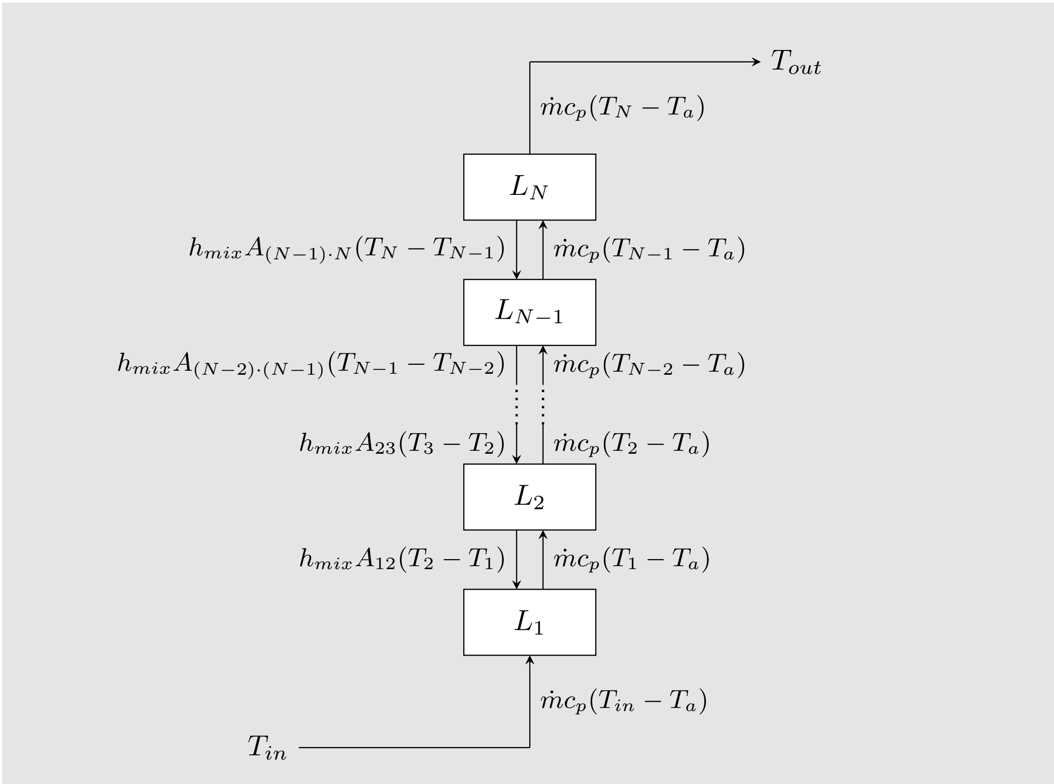

Figure 5.5: Heat transfer model for the draw state.

a lower temperature than the temperatures in the tank, the value for Q_{in} could result in 0 Js transferred in; where the temperature of the inlet is equal to the ambient temperature, $T_{in} = T_a$. Therefore Q_{net} would result in a negative exchange, which would indicate that the layer is losing more energy than it is gaining and therefore reducing its temperature.

The limitations of this model is that the flow rate per time step (i.e. the volume of water moved in one time step) cannot be greater than the volume of the smallest layer.

5.4.2 Model State: Cooling

In the cooling state, there is no transfer of mass, but transfer of heat through conduction. This state occurs when the element is in OFF state, often triggered when the thermostat layer registers a temperature above its upper hysteresis, T_{hyst_U}. In the absence of an external heat source, heat moves between layers and from layer to environment, from higher temperature to lower temperatures.

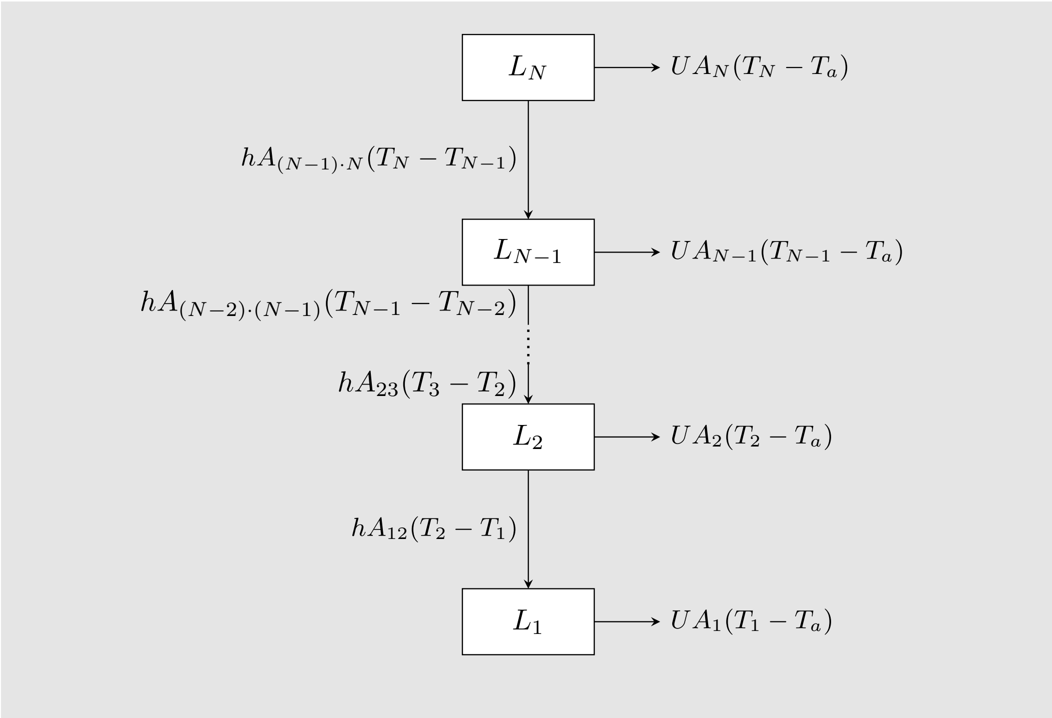

Figure 5.6: Heat transfer model for the cooling state.

An example of this is shown in Layer L_2 in *Figure 5.6*, where heat enters from Layer L_3 through the layer boundary, A_{23} and leaves to Layer L_1 through the layer boundary, A_{12}. Heat is lost to the environment through wall boundary to the environment, A_2. Layer boundaries are defined in *Section 5.2*.

Using the energy exchange equation in *Equation 5.12*, Q_{in} and Q_{out} are determined by *Equation 5.14*, where Q_{in} is the heat from L_3, and Q_{out} is the combination of heat moving to L_1 and the heat lost to the environment.

The rate of heat transfer through the system between layers is constant, and defined by the coefficient, h, representing conduction. This variable is heuristically determined using the control scenario. The rate of heat transfer to the environment is also constant and is dependent on the rate of heat transfer through the insulation of the boundary wall, U. The heat transfer in this state is the slowest of the three processes and while it is always occurring, it is often dominated by the draw and heating states.

5.4.3 Model State: Heating

The heating state is activated when the thermostat layer registers a temperature below a lower threshold, T_{hyst_L}. This temperature is dependant on the manual thermostat setting of the water heater. Once activated, the element will supply heat to its surrounding layers and cause a greater rate of heat exchange between layers due to convection. *Figure 5.7* shows the heating state model with four defined zones: (i) element and conduction, (ii) element and convection, (iii) normal and conduction and (iv) normal and convection.

Layers directly affected by the element are identified as element layers L_{E_1} to L_{E_M} where M is the total number of element layers and m is the iterator. The heat from the element is added to each element layer in an equal distribution based on the volume of the layer, as shown in *Equation 5.18*. The heat contribution of the element in layer Q_{E_m}, where E_m is the iterator for element layers, is a ratio of Q_{E_T}, which is the total heat supplied by the element, in this case the element rating is, 3 kW. The ratio of V_{E_m}, which is the volume of the corresponding layer and the total volume of element affected layers $\sum_{m=1}^{M} V_{E_m}$ determines the ratio of heat supplied to that layer.

$$Q_{E_m} = \left(\frac{V_{E_m}}{\sum_{m=1}^{M} V_{E_m}} \right) Q_{E_T} \tag{5.18}$$

The tank is separated into convective and conductive zones, where the different heat transfer coefficients, h_h and h_l respectively, are assigned to replace h in *Equation 5.14*. These zones are separated midway through the element layers, indicated by $E_{\frac{M}{2}}$. Therefore, heat transfer interactions between layer $E_{\frac{M}{2}}$ to L_N are convective layers with a higher rate of heat transfer h_h, and heat transfer interactions between L_1 to $E_{\frac{M}{2}}$ are conductive layers with heat transfer rates h_l, similar value to h. In this way, convection is crudely modelled by a higher heat conduction coefficient for affected by the element layers.

In the same way that heat transfer is modelled in the cooling state, heat travels between layers through generic heat transfer with different rates for specified layers. When referring to *Equation 5.12*, normal layers have Q_{in} as only the heat from the hotter neighbouring layer, and Q_{out} is the combination of heat that leaves to the colder neighbouring layer and the heat lost to the environment. For element layers,

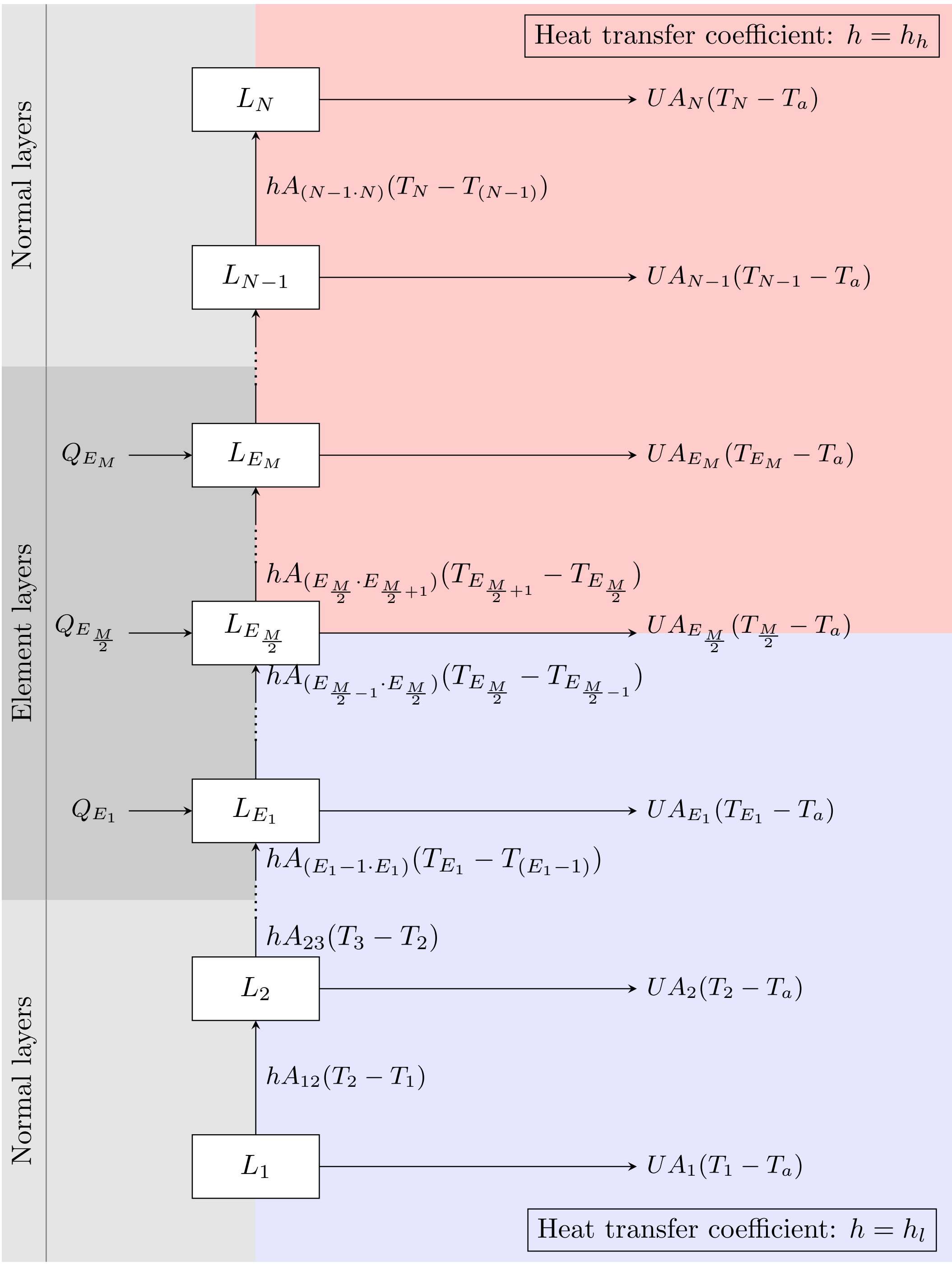

Figure 5.7: Heat transfer model for the heating state.

Q_{in} has an additional input from the element, Q_{E_m}, where all other heat processes acting on the layer remain the same.

5.4.4 Logic for States Switching

The thermostat layer is determined as the corresponding height of temperature sensor T_3, shown in *Figure 3.4 (a)* in *Section 3.2.2*. For a 32 layer simulation configuration, this corresponds to layer L_9 (L_{4j-3}), which is labeled as L'_3 in resulting graphs to correspond to the index of the temperature sensor. The temperature in the thermostat layer is denoted, T_t, which is the temperature used as the conditions for switching the element state. An upper hysteresis temperature, T_{hyst_U}, and a lower hysteresis temperature, T_{hyst_L}, are defined based on the thermostat setting.

The logical conditions required for the tank to move to different states are shown in *Table 5.1*. These conditions accompany the graph shown in *Figure 5.8* to show the states changing over time in steady-state and due to a draw event. If the element is in ON state, the tank will enter heating state and T_t will rise; indicated by Ⓐ. If T_t rises to above T_{hyst_U}, and the element is still in ON state, then the element transitions to OFF state Ⓑ and the tank enters cooling state; indicated by Ⓒ. While the element is in OFF state and T_t is greater than T_{hyst_L}, the element remains in OFF state and the tank remains in cooling state; indicated by Ⓒ. As T_t falls below T_{hyst_L}, the element transitions to ON state Ⓓ and the tank enters heating mode, indicated by Ⓐ. Thus the tank hysteresis is preserved and the tank automatically maintains its high service temperatures.

A draw event can occur stochastically and interrupt the hysteresis cycle at any point, which would drastically reduce the temperatures in the tank, including T_t, as shown in *Figure 5.8*. As the T_t falls below T_{hyst_L}, the thermostat transition the element to ON state Ⓓ and the tank enters heating state Ⓐ. The tank heats up until T_t is greater than T_{hyst_U} to transition the element to OFF state Ⓑ and the tank enters cooling state Ⓒ.

For the EWH in horizontal orientation, not all layers heat up uniformly, as discussed in *Section 3.2.2*, where T_1 and T_2 heat up at slower rates and therefore requires several element operations before steady-state is reached.

5.5 Model Parameters

For implementation of the model (written in Python), several parameters need to be defined; these are catergorised as setup variables and initial variables.

Table 5.1: Karnaugh map representation for conditions for state changes based on temperature of thermostat layer, T_t, and element state.

AND	**Element = ON**	**Element = OFF**
$T_t \leq T_{hyst_U}$	A: Heating State Element remain ON	C: Cooling State
$T_t > T_{hyst_U}$	Enter A: Heating State Element transition B OFF	N/A
$T_t > T_{hyst_L}$	A: Heating State	C: Cooling State Element remain OFF
$T_t < T_{hyst_L}$	A: Heating State	Enter A: Heating State Element transition D ON

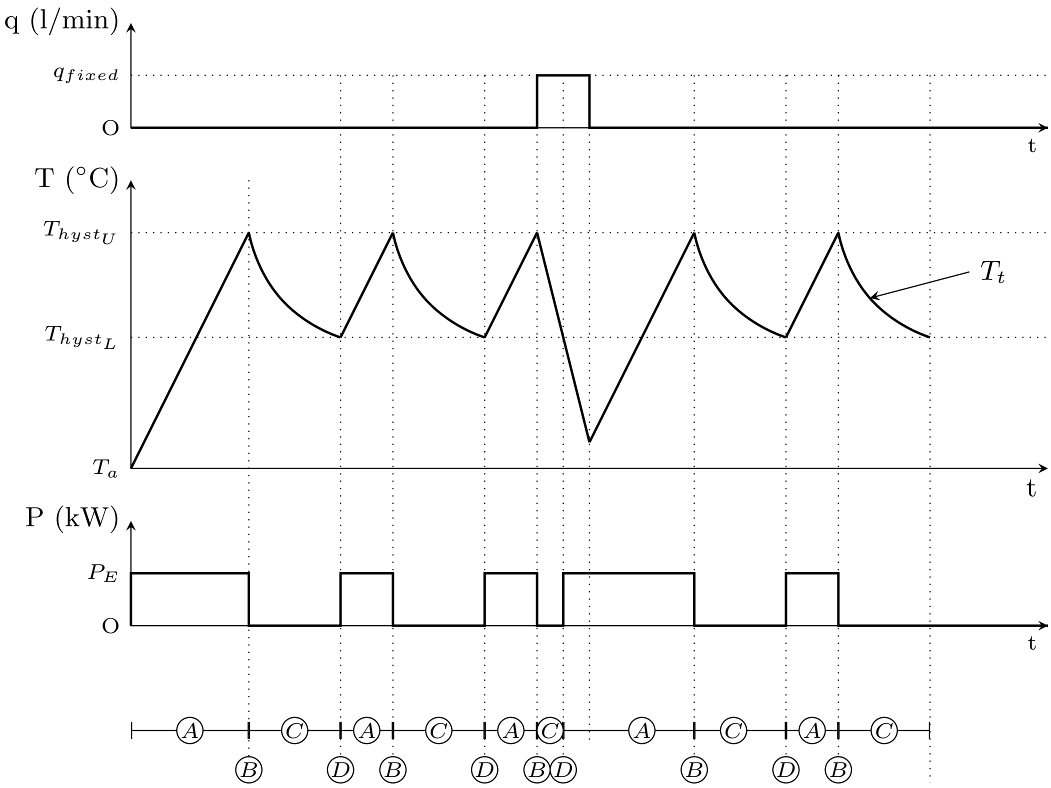

Figure 5.8: Switching conditions for model.

5.5.1 Setup Variables

Setup variables are defined by tank-specific variables and simulation variables. The tank-specific variables required are as follows:

- Total volume (V_T)
- Inner dimensions (R_I, z)
- Element power (P_E)
- Element layers (L_{E_1}, ..., L_{E_M})
- Thermostat layer (L_t)
- Temperature hysteresis limits (T_{hyst_U} and T_{hyst_L})

Tank variables V_T and P_E are determined by given specifications. The inner dimensions R_I and z are calculated and discussed in *Section A.1.2*, due to limited access for measuring. For an EWH with 150 ℓ tank capacity and a 3 kW element placed in horizontal orientation, with inner height (diameter) of 437 mm and length of 1000 mm (as defined in *Figure A.4*). The thermostat layer is determined by matching the height of the thermoprobe to the relevant layer in the model. Element layers are also defined by the size and expected effect of the radiated heat. Temperature hysteresis points T_{hyst_U} and T_{hyst_L} are determined by the thermostat temperature and by observing steady-state operations. The simulation variables that need to be defined before implementation of the model are as follows:

- Number of layers (N)
- Simulation time step (τ)
- Heat transfer coefficients (U, h, h_l, h_h, h_{mix})

Parameters N and τ are chosen variables. The chosen number of simulation layers, (N), is 24 layers (3×8) with a timestep, τ, of 1 s. The heat transfer coefficients are difficult to determine emperically, and therefore will be determined heuristically through the use of pre-training data from experiments. The element layers are defined as Layers $4 - 12$ with the thermostat layer as 7 (/24). The initial variables used to simulate tank changes after draw event scenarios are heurstically determined and provided in *Table 5.2*. The effect of parameters on simulation output parameters is discussed in *Appendix C.3*.

Table 5.2: Model parameters used for simulating low or high flow draw events.

Parameter (unit)	**Simulation Value**
Thermostat layer	Layer 7
Element layers	Layer 4 – 12
Insulation, U	120
Cooling, h	100
Heating Lower Layers, h_l	100
Heating Upper Layers, h_h	800
Mixing, h_{mix}	1 300

5.5.2 Initial Variables

The operational variables required to run the model include the following:

- Ambient temperature (T_a)
- Inlet temperature (T_i)
- Initial temperatures per layer (T_1, ..., T_N)
- Flow rate (q)
- Draw capacity (V_d)
- Total run time for simulation (t_T)

All the operational variables are determined through measured quantities. The initial temperatures inside the tank are determined by using eight RTD sensors placed inside the tank at fixed heights, as discussed in *Section 3.4.1.* If the modelled number of layers is greater than eight, then the initial temperatures of the intermittent layers are interpolated, as discussed in *Section 5.2.4.*

To simplify the implementation of the model, the ambient temperature, inlet temperature and a fixed effective flow rate were assumed as fixed variables during the run time of the simulation.

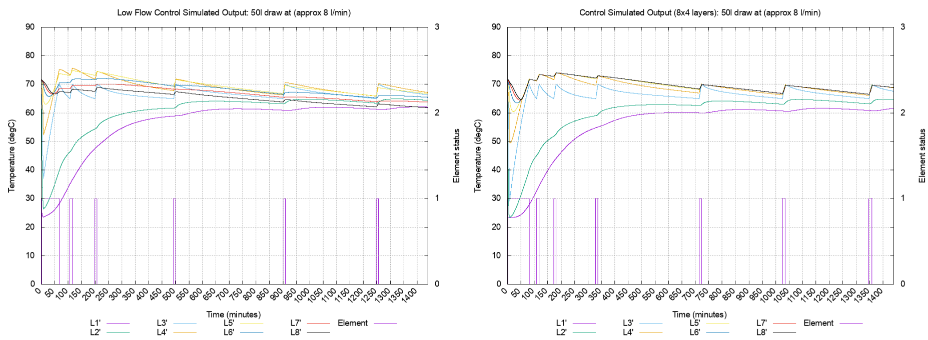

(a) No buoyancy consideration. (b) Additional buoyancy consideration.

Figure 5.9: Simulations output with buoyancy effect considerations for better temperature fidelity of internal tank temperatures.

5.6 Discussion

Some key model design choices are discussed in this section. In particular, an additional process was added from the previous implementation of the model to account for buoyancy considerations to resolve temperature inversions; this is discussed in *Section 5.6.1*. A further discussion is considered for the approach to the heating process modelled for this implementation; this is discussed in *Section 5.6.2*. And finally, a discussion on the choice of simulation layers is presented in *Section 5.6.3*. This includes a discussion on the computation time of the simulation and a comparison to other multi-node model implementations from literature.

5.6.1 Buoyancy Consideration

The consequence of not correctly matching the temperature layers is that the overall efficacy of the model can be called into question and draw scenarios that are outside of a controlled environment may produce unrealiable predictions on the element status. If these considerations are neglected, a temperature inversion appears with the internal temperatures in the tank; an example of this is provided in *Figure 5.9 (a)*.

The layer buoyancy and temperature mixing technique presented in *Equation 5.17* is applied to the model to resolve the temperature inversion. The simulation outputs from the model with modified output is shown in *Figure 5.9 (b))*. The results show no temperature inversion and there is a clear temperature distribution in the tank showing the thermal stratification. The simulated temperatures appear very similar to experimental measurements from a horizontal draw profile presented in *Figure 3.4*.

5.6.2 Approach to Heating Process

The approach taken for temperature mixing processes due to circulating currents in the tank, such as convection or turbulence through the inlet, is handled through heat transfer coefficients h_h and h_{mix}, which have higher values than the coefficients modelling normal conduction between layers h and h_l (typically in the range of $100 \times h$, as seen in *Table 5.2*). Depending on the tank state, the coefficients come into effect to ensure faster movement of heat between layers. These coefficients, with the consideration of buoyancy (shown in *Figure 5.9* in *Section 5.6.1*) produce simulated temperature layers that are fairly well aligned to the experimental results, presented in *Chapter 6*. The weakness in the modelling approach for heuristically-defined heat transfer coefficients is that each new tank will require a validated unique set of parameters.

The heat transfered between layers using the method deployed through heat transfer coefficients is directly proportional to the area of the boundary layer and the difference in temperature between layers, as is seen in *Equation 5.13* and *Equation 5.14*. Therefore, the use of heat transfer coefficients to model mixing processes occurring due to circulating currents is limited by the area and difference in temperatures of the layers and the fixed water density for each node.

Different approaches in literature consider the use of resultant mass flow to represent a fluid stream, or buoyancy induced mixing with variable water density as discussed in *Section 2.5.3*. These approaches could allow for greater control of heat movement for each time-step, which is not limited by the change in temperature or the area of the layer.

5.6.3 Choice of Simulation Layers

The choice of layer structure in the simulation is based on two factors: ability for the model to resolve the subesequent events for heat recovery post draw and computation run time. The comparison of these factors are summarised in *Table 5.3*. The discussion and presentation of the model results from these layer structures are presented in *Appendix C*.

Table 5.3: Number of layers in simulation in comparison to the ability to resolve subsequent element events and simulation computation time for 24−hour single-draw and steady-state.

Parameter (unit)	**8-layers**	**16-layers**	**24-layers**	**32-layers**
Subsequent events	None	One	Two	Two
Simulation time (s)	20.8	21.2	30.9	32.5

The higher number of layers determines a higher degree of stratification (Kleinbach et al., 1993). This means that the high number of layers are able to produce internal tank temperatures that have a well-defined thermocline. As discussed in *Chapter 4*, all the draw events evaluated have at least one subsequent event, and in many low flow rate cases, contain two subsequent events.

The computation time is also a secondary factor in the choice of simulation layer structure. The simulations are performed on a 1.8 GHz i5 processor. The single-item simulation performed consists of a single-draw event with up to 24−hrs of steady-state operations. The computation time for single-item modelling will become a bigger factor in the load aggregation for scaled systems.

Based on the objective of this work, the ability to produce the required subsequent events to resolve the element switching observed in experiments motivated the choice of simulation layers as either 24 layers (3×8). This chosen number of layers is in contrast to early implentations of the TRNSYS tool using the multi-node model which produced validated results for a maximum of 15 layers (Kleinbach et al., 1993). This is also in contrast to the 10−node implementation by Rahman et al. (2016), although this modelled no flow into or out of the tank. Since at this stage, the variations of EWH tank parameters are not considered in the aggregated modelling, the 30 s computation time for single item modelling was considered sufficient to ensure model fidelity.

5.7 Conclusion

This chapter describes the development of a horizontal EWH model, which accounts for the three major states of a tank: draw, heating and cooling. The model separates the volume of water in the tank into discrete layers that hold homogeneous temperatures. Temperature changes to each layer is detemined through a set of heat transfer equations that approximate processes occurring in the tank, mass transfer, conduction, convection and turbulent mixing.

The requirement for the large number of layers in comparison to other applications of multi-node models to resolve the subsequent replacement operations for the element post draw is likely due to the approach taken for modelling the mixing occurring due to circulating currents. The current implementation of the model has a 10 s difference in simulation time between 8 layers (1×8) and 24 layers (3×8). This difference may become more significant if the model needs to scale for the aggregated model approach, where each EWH has its own set of environmental and draw parameters. The future use of mass flow transfer to model circulating currents and factoring in a variable water density based on turbulent flow could be considered. It is possible that these changes could mean the implementation of less layers to reduce the simulation time of the model.

Chapter 6

Results and Validation

This chapter covers the results and validation of the multi-node model for a horizontal EWH. The model is tested against four single-draw scenarios are presented in *Section 6.2*, where the measured data is compared with the simulation output. The model is also tested against a two consecutive draw events in *Section 6.3*. The model performance of the element switching events post draw are discussed in *Section 6.4*. The chapter will be concluded in *Section 6.5*.

6.1 Introduction

The multi-node model is evaluated using a set of draw scenarios to validate its efficacy. Successful tracking of internal tank temperatures and element events will validate the heat transfer processes and the use of model parameters used in the model. The aim is to produce a thermostatically controlled EWH model in horizontal orientation that is capable of resolving the subsequent element events observed from partial draws.

The proposed model will be tested against a set of single-draw events, with volumes and flow rates chosen to cover a range of end-user draw events. These single-draw event tests will determine the "ideal-case" performance of the model in a tightly controlled experiment. A double-draw event scenario will also be discussed to evaluate the efficacy of the model in a simulated "real-world" scenario, where two consecutive draw events occur on the tank and the heat recovery cycle is observed and modelled.

6.2 Single-Draw Validation

The sequence of events modelled is as follows a draw event initiated just after the tank reaches its maximum temperature. This is the same sequence defined in *Section 3.4.1* and used for experiments discussed in *Section 4.3.* This ensures that test cases are comparable with similar starting temperatures in the tank. Thereafter, the model predicts the tank recovery based on temperature changes in the tank and element operations.

A single set of model parameters is used for Sample 1 of each draw scenario introduced in *Section 4.3.* Each single draw scenario was modelled with the multi-node model using the same set of parameters as discussed in *Section 5.5.* The model output for the control scenario 50 ℓ draw at low flow rate is presented in *Section 6.2.1.* The model outputs for the validation scenarios are presented as follows: 50 ℓ draw at high flow rate in *Section 6.2.2*, 100 ℓ draw at low flow rate in *Section 6.2.3*, and 100 ℓ draw at high flow rate in *Section 6.2.4.*

6.2.1 Control: 50-Litre Draw at Low Flow Rate

The model parameters were determined heuristically by using Sample 1 experiment of the low flow rate, 50 ℓ draw scenario presented in *Section 4.3.1.* The full set of measured temperatures and element operations is shown in *Figure 6.1 (a).* The model is set up with the initial variables from the experiment and the model parameters defined in *Table 5.2* (in *Section 5.5.1*) were determined by matching the output to the experimental results. The final output is presented in *Figure 6.1 (b).* Note that since the model is operating with 3×8 layers (24 total), the layer numbers presented are those that match the position of the experimental sensors, indicated by L'_N.

A visual comparison of the experimental results to the simulation results in *Figure 6.1 (a)* and *(b)* yields a good match, which is expected from the control scenario. Both trends have a primary element replacement event (t_{ON_1}) duration of approximately 60 min with the first subsequent element event (t_{ON_2}) occurring at approximately 100 min, and the second subsequent replacement (t_{ON_3}) occurring at approximately 200 min. The next element event occurs at approximately 500 min, which appears to be the start of steady-state operation. Subsequent steady state events (t_{ON_4} and t_{ON_5}) occur around $850 - 900$ min and $1\,150 - 1\,250$min respectively,

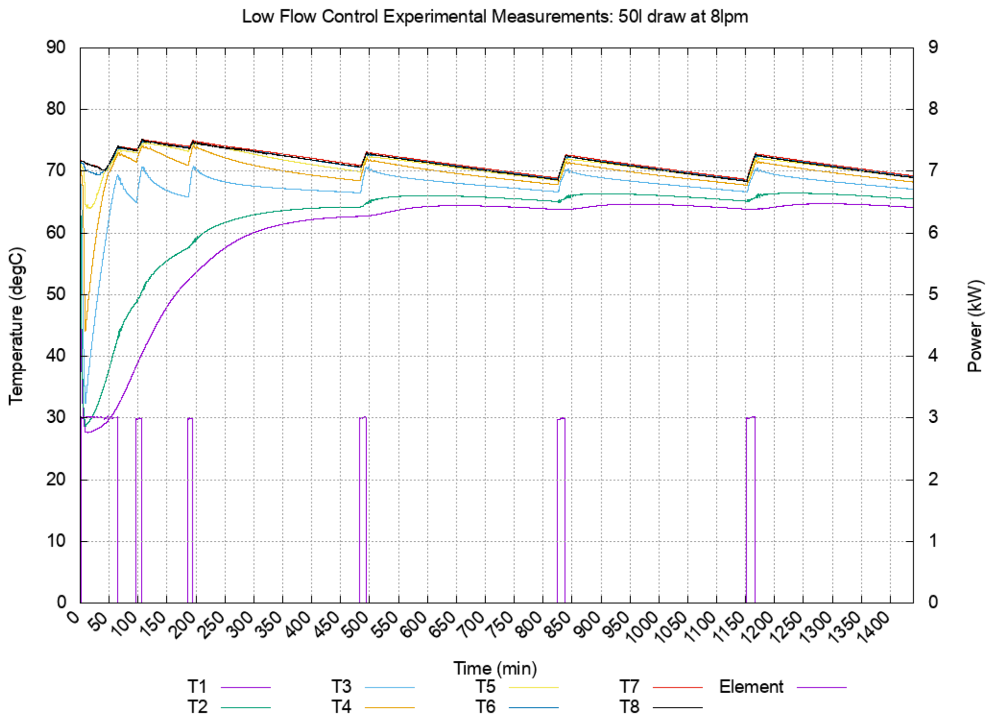

(a) Measured results.

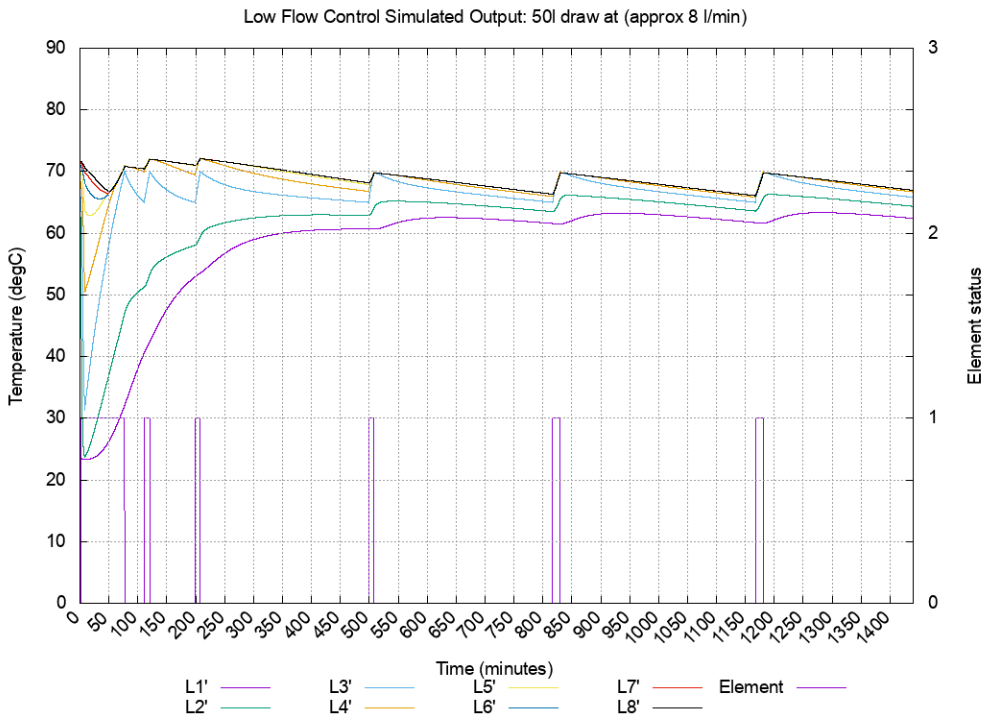

(b) Simulated results.

Figure 6.1: Control test measurements for low flow rate at approx. 8 ℓ/min for a 50 ℓ draw (33% full capacity).

Table 6.1: Element event time comparisons for low flow control (approx. $8\,\ell$/min) for a $50\,\ell$ draw: experiment vs. simulation from *Figure 6.1 (a) and (b).* All values expressed in minutes.

Element event	Experiment (min)		Simulation (min)		Difference (min)	
	Start	t_D	**Start**	t_D	Δt	**% Exp**
ON_1	0	62.22	0	75.27	13.05	20.98
OFF_1	62.22	32.22	75.27	33.65	1.43	4.45
ON_2	94.43	9.8	108.92	9.9	0.1	1.02
OFF_2	104.23	80.08	118.82	78.6	−1.48	−1.85
ON_3	184.32	7.6	197.42	8.43	0.83	10.96
OFF_3	191.92	289.45	205.85	291.42	1.97	0.68
ON_4	481.37	10.12	497.27	8.92	−1.2	−11.86
OFF_4	491.48	331.15	506.18	308.95	−22.2	−6.7
ON_5	822.63	13.58	815.13	12.93	−0.65	−4.79
OFF_5	836.22	313.1	828.07	337.28	24.18	7.72
ON_6	1 149.32	14.43	1 165.35	13.47	−0.97	−6.7

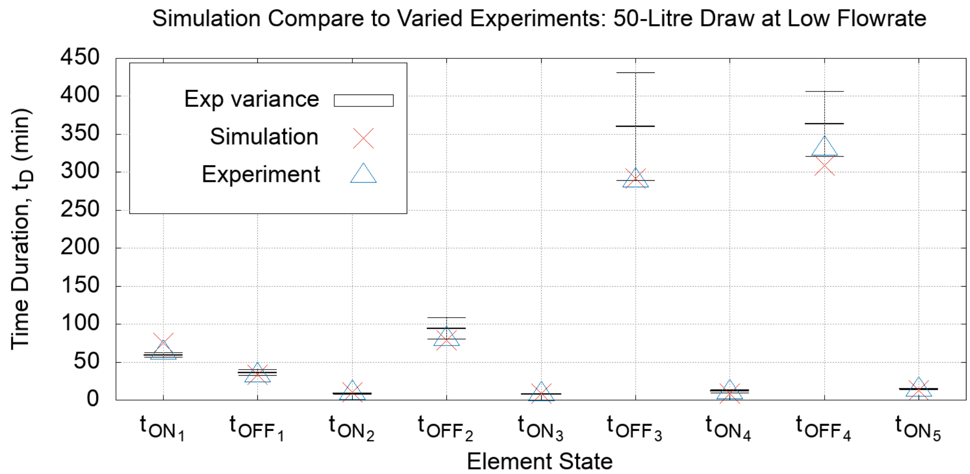

Figure 6.2: Comparison of simulation output using initial parameters of Sample 1 for low flow rate, $50\,\ell$ draw to varied margins from *Section 4.3.1.*

where the model starts to deviate from the experiment.

The associated starting time of an element state change, and the durations in each state (t_D) are presented in *Table 6.1* for both the experiment and the simulation. As discussed in *Section 4.3*, the starting time is used for visual inspection, and the durations in each state (t_D) are more suitable for comparisons. This is done in the final column where the difference of durations in each state for the experiment and the simulation (Δt_{diff}) is determined and the absolute difference to the experiment is determined by percentage.

In *Table 6.1*, it is seen that the primary element replacement is overestimated by 13.05 min (20.98% from the experiment). The subsequent element operations after the primary replacement in the simulation have a duration between $8 - 10$ min, and the steady state operations fall in a range of $13 - 14$ min, which are fairly similar to the experiment. The element in OFF state durations match fairly well to the experiment within a range of 8%, indicating that the thermal conductance of the insulation, (U), is well matched. The worst performing state duration is t_{ON_1}, which has a 21% deviation.

Figure 6.2 represents the results shown in *Table 6.1* graphically by comparing the model output durations for each element state to the maximum absolute variation for the three experiments produced in *Section 4.3.1*. All the switching durations of the events fall close to their error bounds.

6.2.2 Validation: 50-Litre Draw at High Flow Rate

The model parameters produced from the control were tested against another experiment with the same volume drawn but at high flow rate. The Sample 1 experiment of the high flow rate, 50 ℓ draw scenario presented in *Section 4.3.2* was used as the second validation test. The full set of measured temperatures and element operations is shown in *Figure 6.3 (a)*. The model is set up with the initial variables from the experiment and the model parameters defined in *Table 5.2* (in *Section 5.5.1*). The resulting simulation output is presented in *Figure 6.3 (b)*.

A visual comparison of the experimental results to the simulation results in *Figure 6.3 (a)* and *(b)* shows decent matching in features, except there is an extra replacement event in the simulation.

In *Table 6.2*, it is seen that the primary element replacement is overestimated by 2.05 min (3.31% from the experiment). Due to the additional replacement event, the comparison of switching events will be mismatched. The greatest error occurring

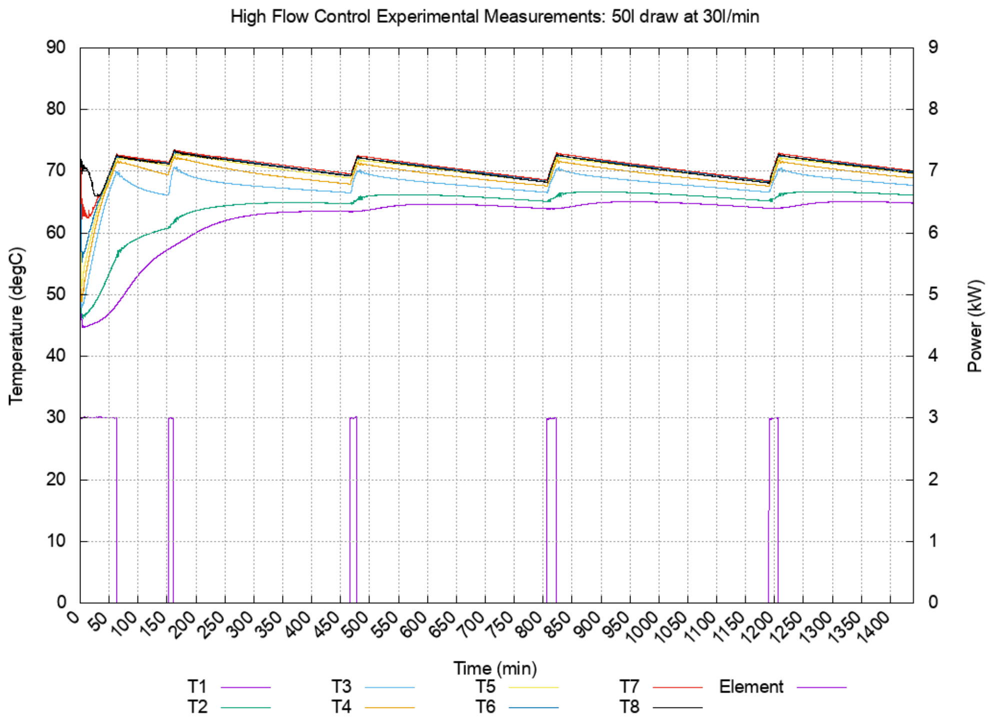

(a) Measured results.

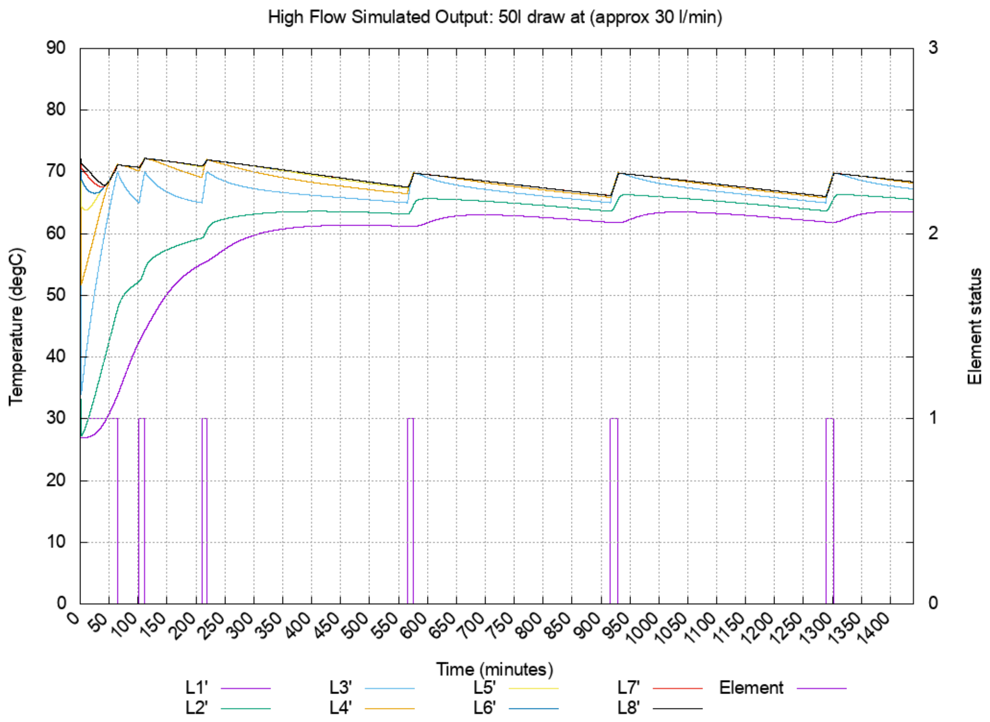

(b) Simulated results.

Figure 6.3: Control test measurements for high flow rate at 30 ℓ/min for a 50 ℓ draw (33% full capacity).

Table 6.2: Element event time comparisons for high flow (30 ℓ/min) validation test for 50 ℓ draw: experiment vs. simulations from *Figure 6.3 (a) and (b)*. All values expressed in minutes.

Element event	Experiment (min)		Simulation (min)		Difference (min)	
	Start	t_D	**Start**	t_D	Δt	**% Exp**
ON_1	0	61.95	0	64	2.05	3.31
OFF_1	61.95	89.68	64	37.43	−52.25	−58.26
ON_2	151.63	9.47	101.43	9.62	0.15	1.58
OFF_2	161.1	305.33	111.05	98.98	−206.35	−67.58
ON_3	466.43	11.57	210.03	8.23	−3.33	−28.82
OFF_3	478	328.15	218.27	347.13	18.98	5.78
ON_4	806.15	15.68	565.4	10.32	−5.37	−34.22
OFF_4	821.83	368.18	575.72	340.43	−27.75	−7.54
ON_5	1 190.02	15.72	916.15	13.27	−2.45	−15.59

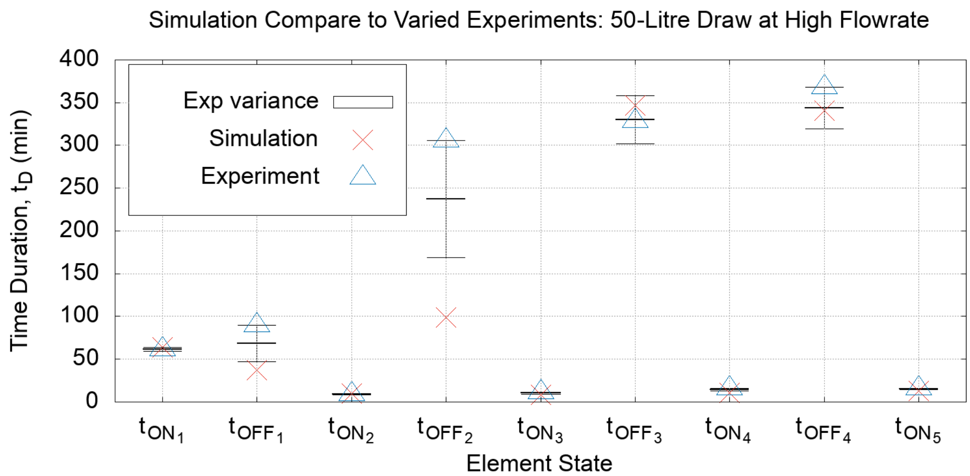

Figure 6.4: Comparison of simulation output using initial parameters of Sample 1 for high flow rate, 50 ℓ draw to varied margins from *Section 4.3.2*.

for t_{OFF_2} with a 67.58% deviation for relative comparisons.

Figure 6.4 represents the results shown in *Table 6.2* graphically by comparing the model output durations for each element state to the maximum absolute variation produced for the three experiments in *Section 4.3.1*. Sample 1 was the outlier, but the simulation still underpredicts for t_{OFF_2}.

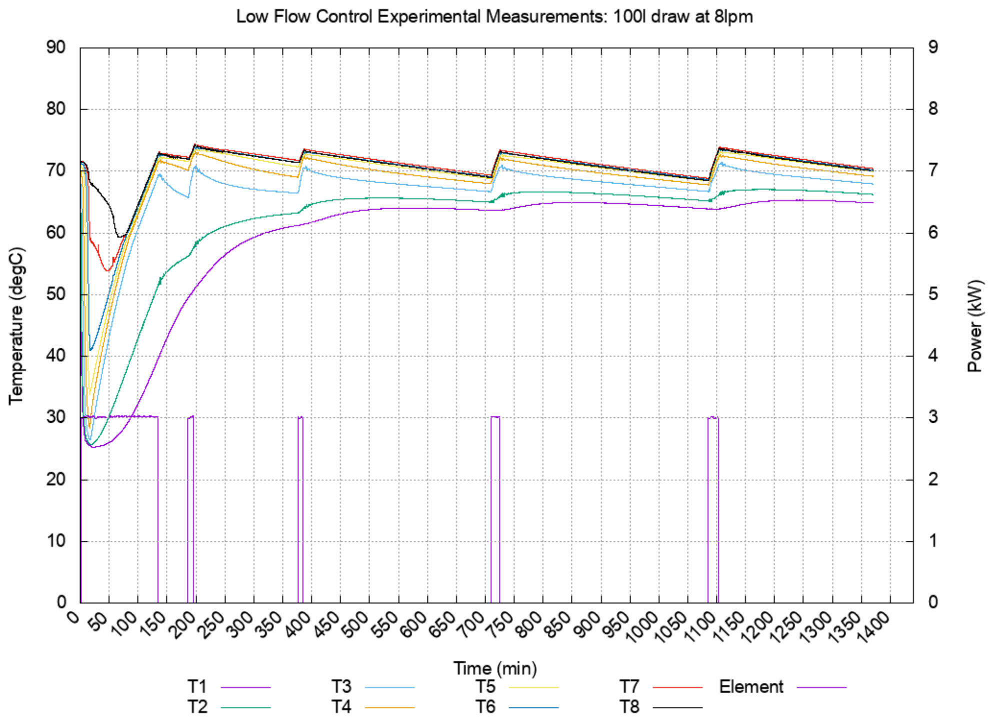

(a) Measured results.

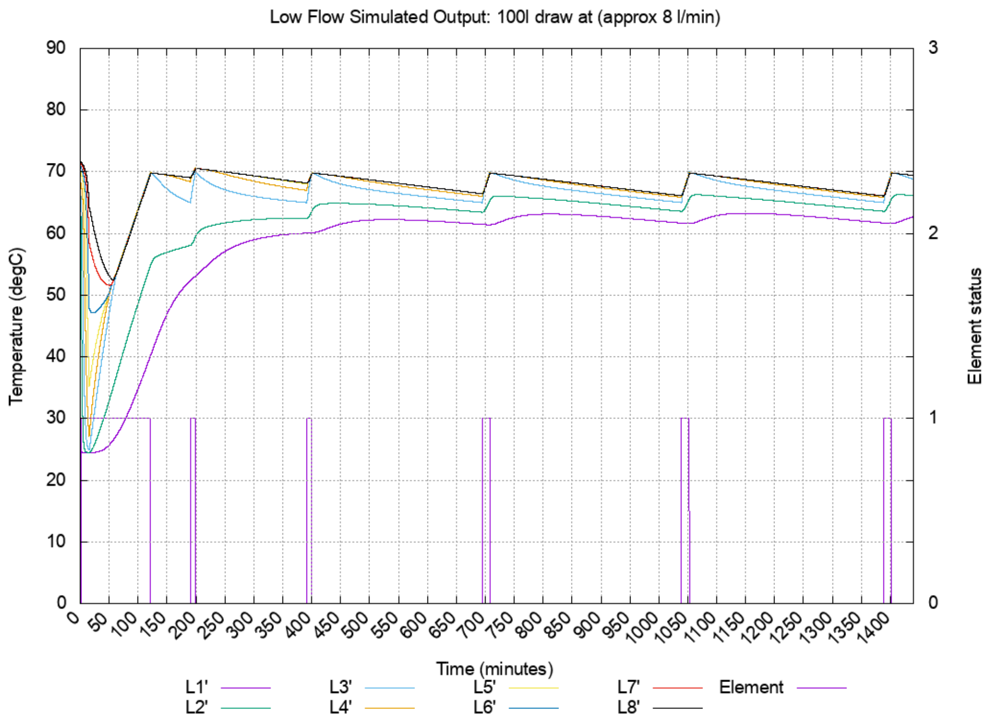

(b) Simulated results.

Figure 6.5: Test measurements for low flow rate at approx. $8\,\ell$/min for a $100\,\ell$ draw (66% full capacity).

6.2.3 Validation: 100-Litre Draw at Low Flow Rate

The model parameters produced from the control were tested against an experimental test with the same flow rate but different draw volume. The Sample 1 experiment of the low flow rate, $100\,\ell$ draw scenario presented in *Section 4.3.3* was used for the first validation test. The full set of measured temperatures and element operations is shown in *Figure 6.5 (a).* The model is set up with the initial variables from the experiment and the model parameters defined in *Table 5.2* (in *Section 5.5.1*). The resulting simulation output is presented in *Figure 6.5 (b).* Again, since the model is operating with 3×8 layers (24 total), the layer numbers presented are those that match the position of the experimental sensors, not the actual layer numbering in the simulation.

A visual comparison of the experimental results to the simulation results in *Figure 6.5 (a)* and *(b)* shows some similar features. The simulated primary element replacement (t_{ON_1}) is much shorter than the experiment. The two subsequent replacement events match well with the experiment. The steady state events thereafter also match well with the experiment.

In *Table 6.3*, it is seen that the primary element replacement is underestimated by 13.27 min (9.98% from the experiment). The duration for t_{OFF_1} over-estimates by 33.8%, but visually allows for the next element event to line up well due to the under-estimation of the primary element event. All other events are matched within a 15% deviation, except for t_{ON_6} where the experiment had an un-naturally long steady-state duration, which is considered an outlier.

6.2.4 Validation: 100-Litre Draw at High Flow Rate

The final validation test on the model parameters is conducted against a high draw ($100\,\ell$) and high flow rate draw scenario, where Sample 1 from the experiment set is used (presented in *Section 4.3.4*). The full set of measured temperatures and element operations is shown in *Figure 6.7 (a).* The model is set up with the initial variables from the experiment and the model parameters defined in *Table 5.2* (in *Section 5.5.1*). The resulting simulation output is presented in *Figure 6.7 (b).*

A visual comparison of the experimental results to the simulation results in *Figure 6.7 (a)* and *(b)* yields a good match with many matching features. Both trends have a primary element replacement event (t_{ON_1}) duration of approximately

Table 6.3: Element event time comparisons for low flow (approximately 8 ℓ/min) validation test for 100 ℓ draw: experiment vs. simulations from *Figure 6.5 (a) and (b)*. All values expressed in minutes.

Element event	**Experiment (min)**		**Simulation (min)**		**Difference (min)**	
	Start	t_D	**Start**	t_D	Δt	**% Exp**
ON_1	0	132.95	0	119.68	−13.27	−9.98
OFF_1	132.95	51.38	119.68	68.75	17.37	33.8
ON_2	184.33	10.18	188.43	8.7	−1.48	−14.57
OFF_2	194.52	179.52	197.13	192.6	13.08	7.29
ON_3	374.03	9.35	389.73	8.78	−0.57	−6.06
OFF_3	383.38	323.97	398.52	294.55	−29.42	−9.08
ON_4	707.35	14.8	693.07	12.68	−2.12	−14.3
OFF_4	722.15	361.23	705.75	331.53	−29.7	−8.22
ON_5	1 083.38	18.27	1 037.28	13.42	−4.85	−26.55

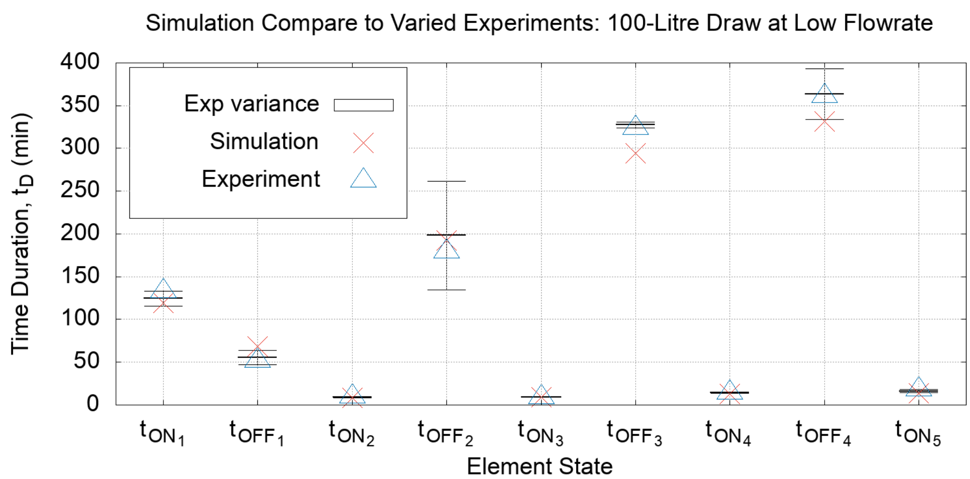

Figure 6.6: Comparison of simulation output using initial parameters of Sample 1 for low flow rate, 100 ℓ draw to varied margins from *Section 4.3.3*.

100 min, where the simulation is producing minor underestimate. The first and second subsequent element events show good agreement at approximately 200 min and 400 min mark. The steady-state events show fair agreement, with an off-set in time.

In *Table 6.4*, it is seen that the primary element replacement is underestimated by

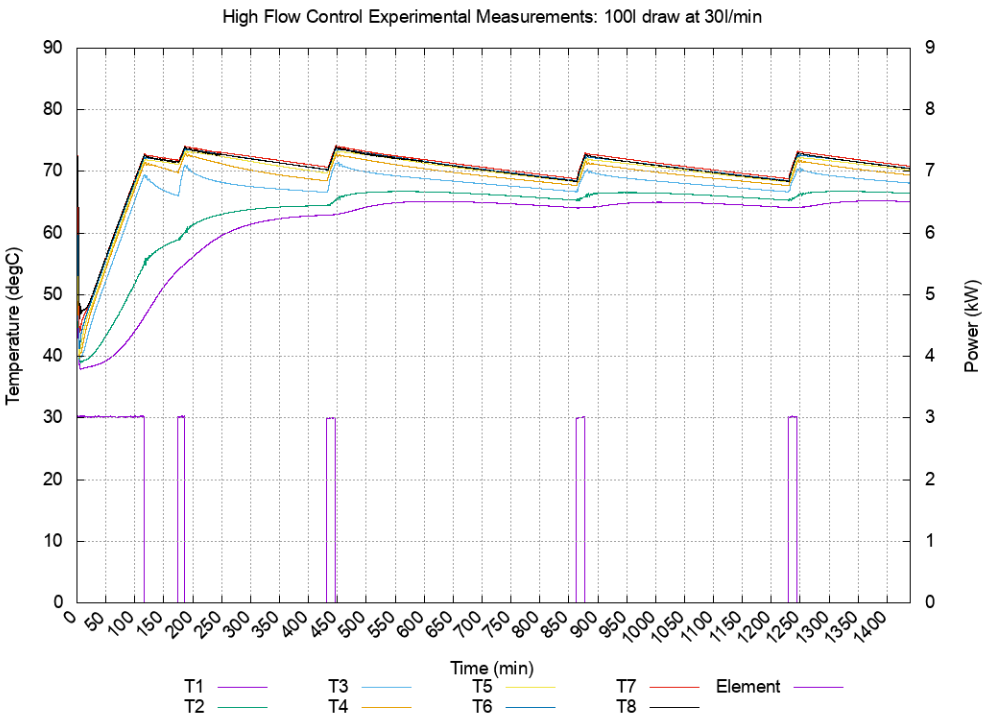

(a) Measured results.

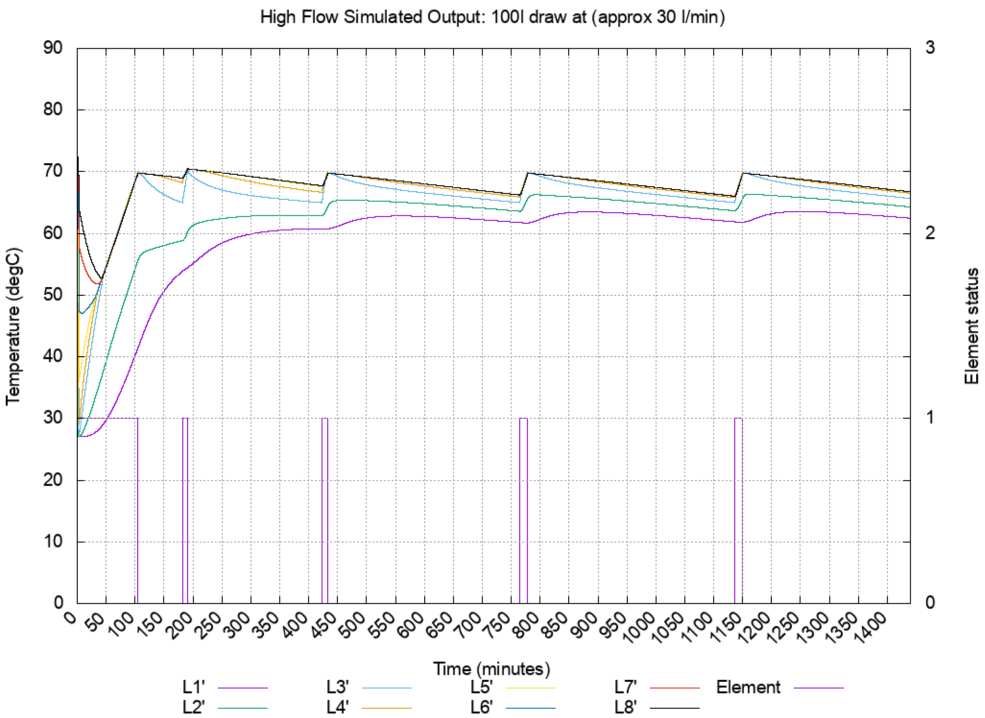

(b) Simulated results.

Figure 6.7: Control test measurements for high flow rate at $30\,\ell$/min for a $100\,\ell$ draw (66% full capacity).

Table 6.4: Element event time comparisons for high flow (30 ℓ/min) validation test for 100 ℓ draw: experiment vs. simulations from *Figure 6.7 (a) and (b)*. All values expressed in minutes.

Element event	**Experiment (min)**		**Simulation (min)**		**Difference (min)**	
	Start	t_D	**Start**	t_D	Δt	**% Exp**
ON_1	0	115	0	104.75	−10.25	−8.91
OFF_1	115	59.47	104.75	77.2	17.73	29.82
ON_2	174.47	10.6	181.95	8.57	−2.03	−19.18
OFF_2	185.07	246.57	190.52	232.37	−14.2	−5.76
ON_3	431.63	14.33	422.88	9.82	−4.52	−31.51
OFF_3	445.97	416.57	432.7	332.4	−84.17	−20.2
ON_4	862.53	14.3	765.1	13.12	−1.18	−8.28
OFF_4	876.83	351.72	778.22	358.27	6.55	1.86
ON_5	1 228.55	15.4	1 136.48	13.57	−1.83	−11.9

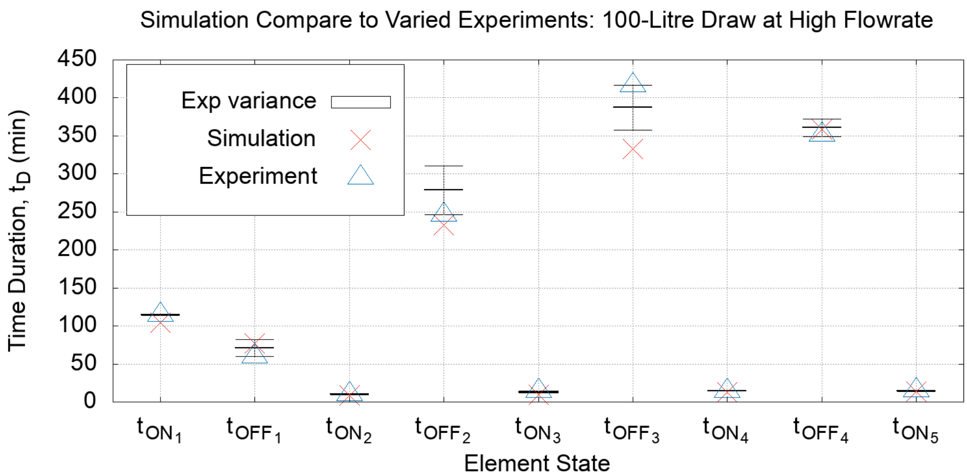

Figure 6.8: Comparison of simulation output using initial parameters of Sample 1 for high flow rate, 100 ℓ draw to varied margins from *Section 4.3.4*.

10.25 min (8.91% from the experiment). The greatest errors are seen in the OFF_1 duration and ON_3 with deviations around 30%.

Figure 6.8 represents the results shown in *Table 6.4* graphically by comparing the model output durations for each element state to the maximum absolute variation produced for the three experiments in *Section 4.3.4*. Most of the events are underestimated for each element state, although they are predicted close to the range of experimental observations.

6.2.5 Single-Draw Discussion

The resulting error comparisons from each of the draw scenarios are summarised in *Figure 6.9 (a)* and *(b)*. There are two types of errors determined, (a) Percentage error based on experimental state, and (b) Time difference error against a 24 hr base.

The relational percentage error comparisons illustrated in *Figure 6.9 (a)* are the percentage errors of the difference in state durations from the simulations to the experiment. A positive error indicates that the simulation overestimates the state duration, whereas a negative error indicates that the simulation underestimates the duration of the state. In general, it is seen that the model underestimates most of the durations of element states.

The percentage errors depicted in *Figure 6.9 (a)* show large errors towards 65% as the time difference is compared to the expected duration for the element state from the experiment. The note that the worst performing draw pattern was the 50 ℓ high flow, which is due to the presence of an additional subsequent element event.

Also shown in *Section 4.3.5*, variations for element state durations from tests of the same draw scenario can have a variance of over 30%. Another way to view the data is the time difference against a fixed time, such as 24 hr (or 24×60 min), as described in *Equation 6.1.*

$$\epsilon_{\Delta t} = \frac{t_{d_{sim}} - t_{d_{exp}}}{24 \times 60} \times 100 \tag{6.1}$$

The results illustrating errors calculated from $\epsilon_{\Delta t}$ are shown in *Figure 6.9 (b)*. The most notable difference from *Figure 6.9 (a)* is the t_{ON} steady-state states are greatly reduced in their errors. This is due to the short duration of the pulses that account for a much shorter portion of a 24-hr period. Both of these graphs will be used to evaluate the matching of the simulation against experiment matching of each draw scenario.

The best matching event scenario is the control event (low flow, 50 ℓ draw), which is expected as the model parameters were determined from this scenario. It has the best overall performance for switching events, however, it has the highest error on the primary event, which will play a significant role in the aggregated demand.

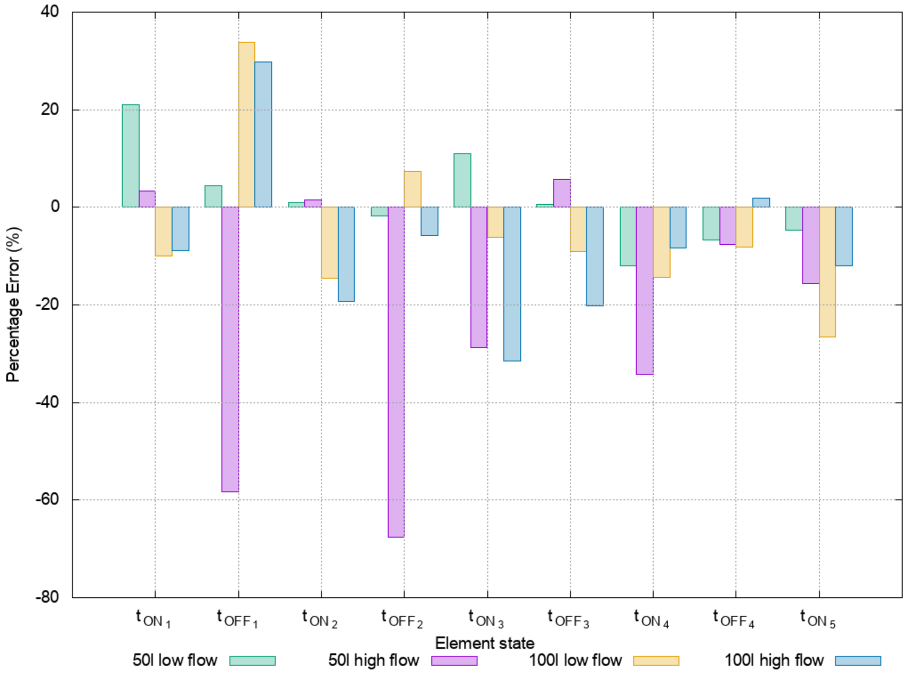

(a) Percentage error relative to duration of experiment state.

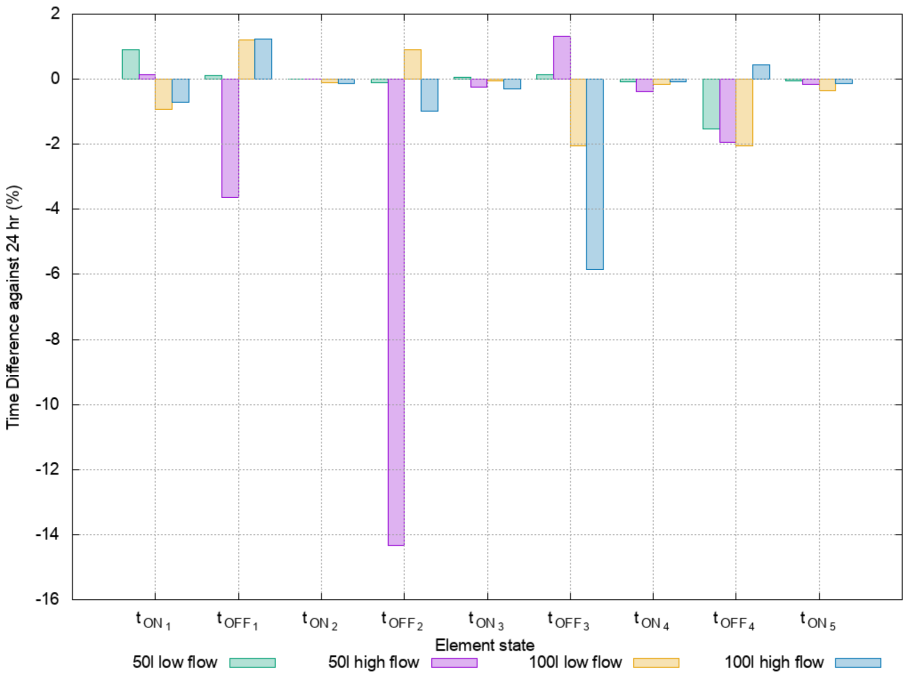

(b) Percentage error relative to a 24 hr period.

Figure 6.9: Percentage error of simulation element state durations to experiment for each draw scenario. The percentage errors illustrated are taken from *Table 6.1*, *Table 6.3*, *Table 6.2*, *Table 6.4*. (a) Percentage error relative to duration of experiment state. (b) Percentage error relative to a 24 hr period.

Both $100\,\ell$ draw simulations show reasonable agreement. Both present fairly high deviations in t_{OFF_1} and t_{OFF_3}, which could indicate a weakness in the model for higher draw volumes.

Since the main focus of this work is to determine the element states for draw replacements, the simulated outputs from the model will be discussed in terms of its separate components: draw replacements in *Section 6.4.1.*

6.3 Double-Draw Validation

To emulate a real-world scenario, the model is tested against an experiment with two consecutive draw events. Similar to the single-draw event scenarios, the experiment is initiated from a fully heated tank. Two $25\,\ell$ draws are conducted at a flow rate of $8\,\ell/\text{min}$, with a 10 min separation between the draw events.

Figure 6.10 (a) shows the measurements from the experiment for the double draw event. The primary element event for the double draw event remains in ON state for 75 min, which is followed by two replacement cycles. Under 300 min of tank recovery data was collected, which is sufficient to show the subsequent events for the simulation. It can be seen that Sensor T_2 malfunctioned midway through the experiment.

The double draw scenario is modelled with the multi-node model using the same set of parameters as discussed in *Section 5.5*. *Figure 6.10 (b)* shows the model performance for the double draw event. There is good visual agreement in the temperatures for each simulated layer and the element events also match fairly well. This shows that the resolution of the layers in the multi-node model can track the changes in temperatures well enough to resolve the subsequent element events seen in the experimental measurements.

6.4 Discussion

The simulation outputs from the multi-node model have been discussed in relation to duration of element switching events to an experimental dataset. Visual comparisons are considered for absolute time comparisons and relative errors are considered for each switching event.

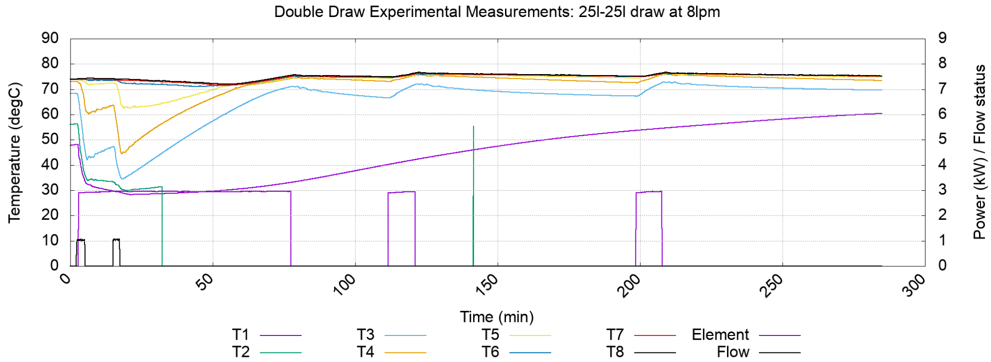

(a) Experimental measurements for double draw event.

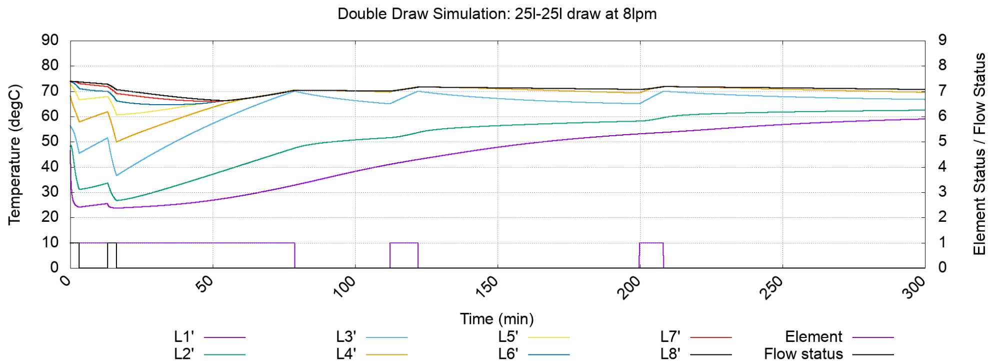

(b) Simulated results for double draw event

Figure 6.10: Double draw event, two consecutive 25 ℓ draws at 8 ℓ/min separated by 10 min. (a) Experimental measurements. (b) Resulting model ouput.

The results for four single-draw replacement scenarios and the double-draw replacement is discussed in *Section 6.4.1*.

6.4.1 Draw Replacement

For the single-draw events, the simulation outputs from the multi-node model show good visual agreement with the experimental measurements. In three of the four cases, the model parameters produced element patterns that generally matched the draw replacement patterns. Notably, 50 ℓ low flow over-estimates the primary event and 50 ℓ high flow that includes an additional subsequent replacement event, which produces high relative errors for each element switching event.

For the double-draw event, the simulation outputs show good visual agreement with the experimental measurements. This provides an indication that the model outputs can be applied to non-controlled experiments and therefore shows the potential for expansion to more realistic draw patterns.

6.5 Conclusion

A set of heuristically determined parameters are produced using a control draw scenario. Three additional draw scenarios are tested using the parameters for validation purposes. The main aim of the model is to correctly model the draw replacement characteristic of the element, which has been done with reasonable success. Three of the four tests scenarios show promise, with good matching on each element state. One test scenario (50 ℓ at high flow rate) produces a visual match over a 24-hour observation, but includes an additional subsequent replacement event. An example using a double draw event has successfully produced a good visual match in profiles, indicating confidence that the model is versatile and can be expanded to realistic draw examples.

The next chapter applies this model in an aggregated system to determine the effect of predicted grid loading parameters such as the cumulative peak power demand and time of peak.

Chapter 7

Aggregation Effects

This chapter covers the system effects of the proposed models through aggregation of load profiles. The aggregation method is described in *Section 7.2* and the resulting load profiles are presented in *Section 7.3*. A comparison of perfomance against a binodal model is presented in *Section 7.4*. The discussions on the results are presented in *Section 7.5* and the opportunities for DSM are presented in *Section 7.6*. The chapter will be concluded in *Section 7.7*.

7.1 Introduction

The aggregation of load profiles provides an indication of the cumulative system impact of controllable loads. This is a vital tool to determine the impact of control strategies for the effective usage of TES as deferrable loads. The control strategies could be employed for the following applications:

- peak demand reduction,
- loadshedding related reductions (prevention or system recovery),
- draw excess supply in times of renewable surplus

Such aggregation techniques also lend towards determining, with greater confidence, the system impact of changes in TES designs for energy savings and identifying opporunities for cleaner energy sources for domestic water heating.

This chapter will investigate the efficacy of the multi-node model developed in *Chapter 5* and verified in *Chapter 6*. This chapter examines the model performance against the expected impact from experimental trends using a replication aggregation technique. The results from multi-node model will also be compared with the performance of the binodal model. By simulating the aggregation effects of the experimental output against the model output and using the same seeding for EWH participation on the grid, it is possible to verify effectiveness of using the model through comparisons of cumulative peak demand, time of peak and total energy.

7.2 Method

This section presents a comparison of the simulated cumulative effects for a partial draw event of a tank in horizontal orientation to its experimental counterpart. The resulting load profiles provide a means to compare the overall effect in the switching differences of the simulated and experimental element loads. The element datasets used are the same four datasets determined in *Section 6.2*:

- $50\,\ell$ at low flow rate (presented in *Section 6.2.1*),
- $50\,\ell$ at high flow rate (presented in *Section 6.2.2*),
- $100\,\ell$ at low flow rate (presented in *Section 6.2.3*), and
- $100\,\ell$ at high flow rate (presented in *Section 6.2.4*).

A load profile is aggregated by replicating a time-varying load profile (or element switching profile) of an EWH for the simulated population, i.e. 10 EWHs means replication of the same signal 10 times. If all EWHs produce service at the same time, the aggregated load profile would show the same element switching profile at the same times as the experimental profiles with a cumulative peak demand of $10 \times P_E$. A peak time interval is applied to the population to introduce delays to each EWH producing hot water service, denoted as t_{delay}, as shown in *Figure 7.1 (a)*. This results in a varied a more realistic load profile.

The time that each EWH starts to load the grid, t_{delay}, with heat replacement from a draw event is determined by a random number generator that has a Gaussian distribution (Marsaglia and Tsang, 2000). The time produced from the random number generator is within the range of the peak time interval, as shown in *Figure 7.1 (a)*.

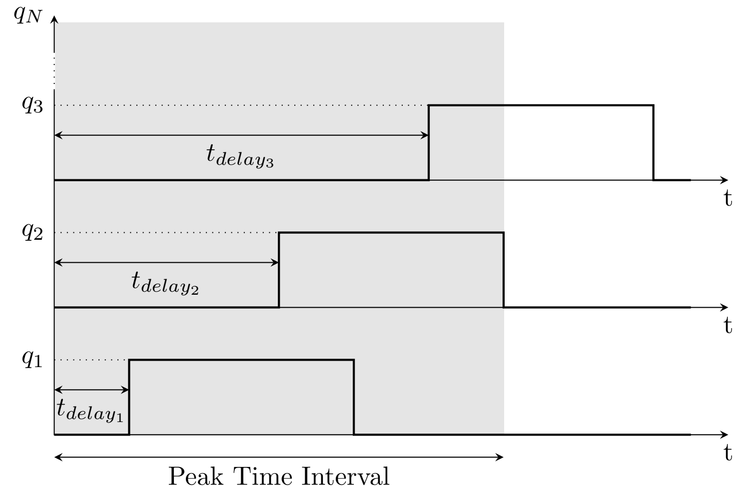

(a) Theoretical time distribution of draw events at fixed flow rate, q within a peak time interval (in gray).

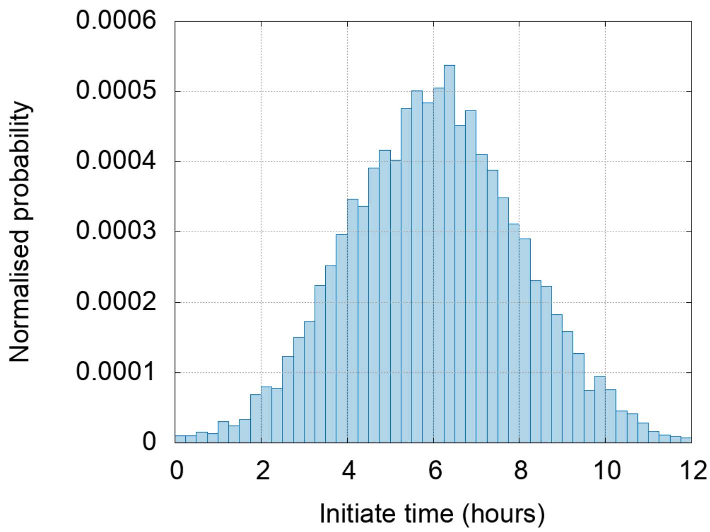

(b) Time delays histogram.

Figure 7.1: Time distributions for initiating each draw event within the demand interval (a) Times of delays, where t_{delay} is a randomised time from the start of the simulation within a peak time interval and (b) Histogram of delays for $1e4$ EWH in a 12 hour time frame.

The Gaussian distribution is used in an attempt to model human behaviour and to produce definitive regions for peak demand for ease of comparison (Lane and Beute, 1996). *Figure 7.1 (b)* shows the normalised probability distribution used for a 12-hour peak time interval for the $10,000$ (or $1e4$) EWH population.

A range of peak time intervals considered are 0, 4, 8 and 12 hours, where 4 hrs represents the most realistic peak time interval for the South African power grid.

A range of EWH populations is also considered: 10, 100, 1 000 and 10 000, or ($1e1$, $1e2$, $1e3$ and $1e4$). The South African grid caters to approximately 5.4 million EWH on the grid (StatsSA, 2016), but for the purposes of this investigation, only 10 000 are considered.

For each draw scenario, there are two aggregated load profiles produced for comparison: one using the replicated experimental load and the other using the replicated simulated load. The set of t_{delays} for each load profile is identical for a specific population and peak time interval, ensuring that the simulated hot water service is the identical. These two load profiles are then compared to determine the peak demand, time of the peak and total energy in the system. The benefit of limiting the aggregation to one validated set of element traces for a fixed draw is to determine the effect of other factors that come into play in aggregated systems such as the EWH population and demand time intevals. And finally, each EWH only participates on the grid when its draw is initiated, therefore steady-state operation before that time is ignored.

Load profile synthesis of large-scale grid modelling would include a variety of EWHs with a wider variety of draw conditions. For the purposes of this investigation, real-time or realistic hot-water draw times with variable draw capacities are not considered for the production of the load profiles in the discussion. In this chapter, the synthesised load models have been used to compare a single draw replacement element pattern for both an experiment and a simulation. This is used to determine the aggregated effect of using the predicted output of the simulation and how it would differ from the experiment. This is with the assumption that all the EWHs on the system are identical and have identical replacement element patterns. This has been shown to be highly unlikely from the variances produced in *Section 4.3*.

7.3 Results

Load profiles for each experimental and simulated scenario for the multi-node model (discussed in *Chapter 5*) are presented in the following subsections. The load profile results for the maximum population of 10 000 EWH (or $1e4$) presented at each considered peak demand interval. The aggregation effects are best discussed with large populations, as there is less stochastic variability with larger populations and trends can be better observed. The features from the load profiles will be discussed in each subsection and a discussion of overall trends for peak demand and energy in the system will be discussed in (1) 50 ℓ low flow (in *Section 7.3.1*), (2) 50 ℓ high flow (in *Section 7.3.2*), (3) 100 ℓ low flow (in *Section 7.3.3*) and (4) 100 ℓ high flow (in *Section 7.3.4*).

Important features from each of the load prediction modelling is the ability to determine peak demand (time of occurrance and peak load) to a lesser extent, total energy loaded in the system. The synthesised load profiles produce peaks that will be compared by demand (MW) and time of occurance (hr). Based on nature of the experiment, only the first peak is determined. Therefore, a ratio of P_{sim}/P_{exp} is used to describe the comparison of peaks, where P_{sim} is the peak demand for the simulated element operations, and P_{exp} is the peak demand for the element operations from the experiment. In cases where $P_{sim}/P_{exp} = 1$, the demand peaks of both orientations are equal. The same applies to time of occurrance where a ratio of t_{sim}/t_{exp} is used to describe the comparison of peak times, where t_{sim} is the time of peak for the simulated element operations, and t_{exp} is the time of peak for the element operations from the experiment. An error calculation is also implemented, where ϵ_P represented in *Equation 7.1* is the error for peak demand and ϵ_t is the error for time of occurance, shown in *Equation 7.3*.

$$\epsilon_P = \frac{P_{sim} - P_{exp}}{P_{exp}} \times 100 \tag{7.1}$$

$$\epsilon_E = \frac{E_{sim} - E_{exp}}{E_{exp}} \times 100 \tag{7.2}$$

$$\epsilon_t = \frac{t_{sim} - t_{exp}}{t_{exp}} \times 100 \tag{7.3}$$

Peak demand ratios and energy ratios are also discussed across the whole simulated range of populations of EWH on the system. Ratios for peak demand are discussed in *Section 7.3.5* and ratios for energy are discussed in *Section 7.3.6*.

7.3.1 Load Profiles: 50-Litre Draw at Low Flow Rate

The low flow rate, 50 ℓ draw scenario experiment and simulation from *Section 6.2.1* is aggregated and the synthesized load profiles for a 10 000 EWH population are presented in *Figure 7.2*. *Table 7.1* presents the values for peak demand and peak

Table 7.1: Load profile comparison of peak demand and time of peak for experiment and simulations for low flow 50 ℓ draw (refer to *Figure 7.2*).

Feature	**Demand Interval**			
	0 hr	**4 hr**	**8 hr**	**12 hr**
Peak Demand Exp P_{exp} (MW)	30	17.58	10.52	7.54
Peak Demand Sim P_{sim} (MW)	30	19.93	12.28	8.76
Peak Demand Ratio P_{sim}/P_{exp}	1	1.13	1.17	1.16
Error Peak $\frac{P_{sim}-P_{exp}}{P_{exp}} \times 100$ (%)	0	13.38	16.68	16.24
Time of Peak Exp t_{exp} (hr)	0	2.57	4.73	6.52
Time of Peak Sim t_{sim} (hr)	0	2.63	4.74	6.63
Peak Time Ratio t_{sim}/t_{exp}	0	1.03	1	1.02
Error Peak Time $\frac{t_{sim}-t_{exp}}{t_{exp}} \times 100$ (%)	0	2.61	0.35	1.67

times. *Section 6.2.1 (a)* shows the load profile for 0 hr demand window, which means that all EWHs enter the grid at the same time, resulting in the original trend with peak demand equal to the element size multiplied by the EWH population at 30 MW. The left trend is the experiment and the right trend is the simulation from the multi-node model.

4 hr Demand Interval: The load profiles for a 4 hr demand interval are presented in *Figure 7.2 (b)*. The peak demand from the experiment is 17.58 MW which occurs at 2.57 hrs into the simulation and the peak demand from the simulation is 19.93 MW occurring at 2.63 hrs. This has a peak ratio (P_{sim}/P_{exp}) of 1.13 and a time of peak ratio (t_{sim}/t_{exp}) of 1.03. The simulation over estimates the peak by 13.38% and the peak time by 2.61%.

8 hr Demand Interval: The load profiles for a 8 hr demand interval are presented in *Figure 7.2 (c)*. The peak demand from the experiment is 10.52 MW which occurs at 4.73 hrs into the simulation and the peak demand from the simulation is 12.28 MW occurring at 4.74 hrs. This results in a peak ratio (P_{sim}/P_{exp}) of 1.17 and a time of peak ratio (t_{sim}/t_{exp}) of 1. The simulation over estimates the peak by 16.68% and the peak time is overestimated by 0.35%.

12 hr Demand Interval: The load profiles for a 12 hr demand interval are presented in *Figure 7.2 (d)*. The peak demand from the experiment is 7.54 MW which

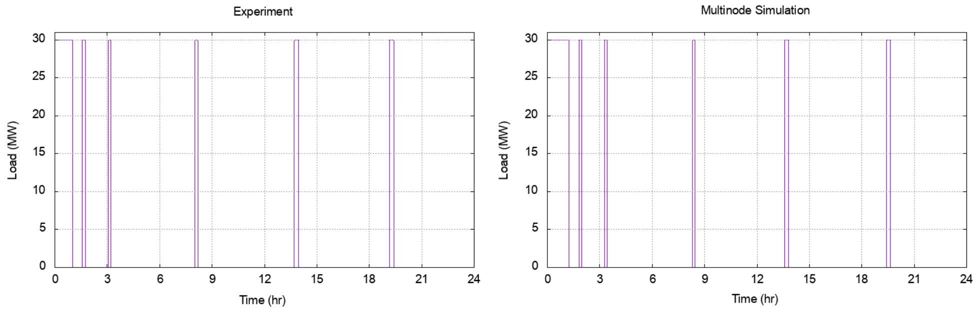

(a) Demand interval window: 0 hrs.

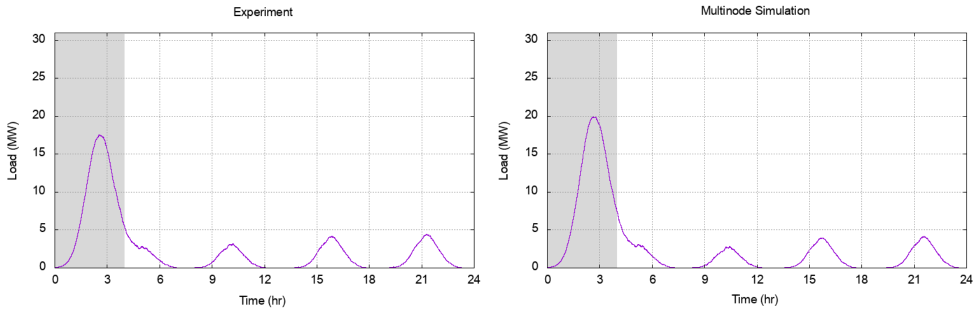

(b) Demand interval window: 4 hrs.

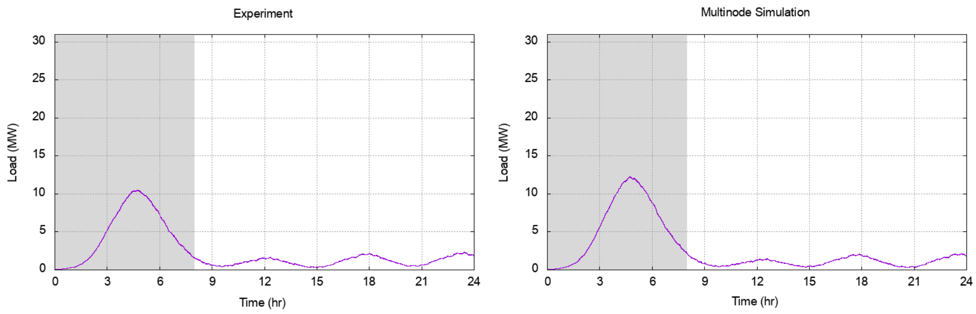

(c) Demand interval window: 8 hrs.

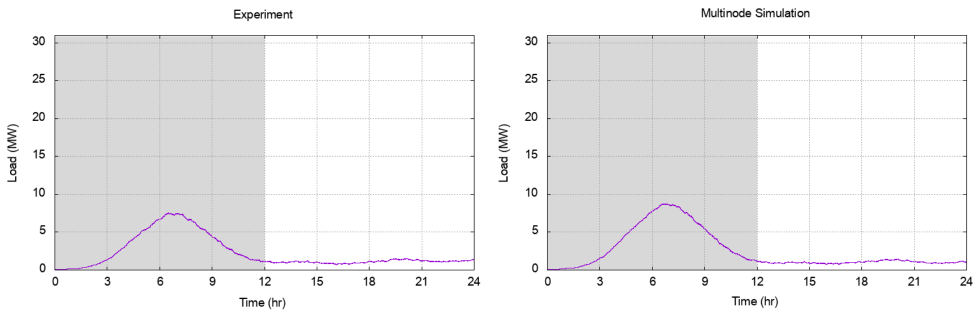

(d) Demand interval window: 12 hrs.

Figure 7.2: Synthesised aggregated load profiles of experiment against simulation of low flow (approx. 8 ℓ/min for a 50 ℓ draw for a EWH population of 10 000 and varying demand windows of [0; 4; 8; 12] hrs.

Table 7.2: Load profile comparison of peak demand and time of peak for experiment and simulations for high flow 50 ℓ draw (refer to *Figure 7.3*).

Feature	**Demand Interval**			
	0 hr	**4 hr**	**8 hr**	**12 hr**
Peak Demand Exp P_{exp} (MW)	30	16.79	9.66	6.91
Peak Demand Sim P_{sim} (MW)	30	17.74	10.63	7.62
Peak Demand Ratio P_{sim}/P_{exp}	1	1.06	1.1	1.1
Error Peak $\frac{P_{sim}-P_{exp}}{P_{exp}} \times 100$ (%)	0	5.67	9.97	10.38
Time of Peak Exp t_{exp} (hr)	0	2.56	4.76	6.63
Time of Peak Sim t_{sim} (hr)	0	2.59	4.63	6.43
Peak Time Ratio t_{sim}/t_{exp}	0	1.01	0.97	0.97
Error Peak Time $\frac{t_{sim}-t_{exp}}{t_{exp}} \times 100$ (%)	0	0.99	-2.87	-2.93

occurs at 6.52 hrs into the simulation and the peak demand from the simulation is 6.52 MW occurring at 6.63 hrs. This results in a peak ratio (P_{sim}/P_{exp}) of 1.16 and a time of peak ratio (t_{sim}/t_{exp}) of 1.02. The simulation over estimates the peak by 16.24% and the peak time is underestimated by 1.67%.

The synthesised load profile from the multi-node model model matches fairly well with the load profiles from the experiments. The model over-estimates the peak demand by approximately 17% and it is likely due to the longer primary replacement time in the simulation. The time to peak for the model matches very well with errors within 3%. The steady-state peaks match fairly well, both in demand amplitude and time of occurrance).

7.3.2 Load Profiles: 50-Litre Draw at High Flow Rate

The high flow rate, 50 ℓ draw scenario experiment and simulation from *Section 6.2.2* is aggregated and the synthesized load profiles for a 10 000 EWH population are presented in *Figure 7.3*. *Figure 7.3 (a)* shows the load profile for 0 hr demand window with a multiplied peak of 30 MW.

4 hr Demand Interval: The load profiles for a 4 hr demand interval are presented in *Figure 7.3 (b).* The peak demand from the experiment is 16.79 MW which occurs

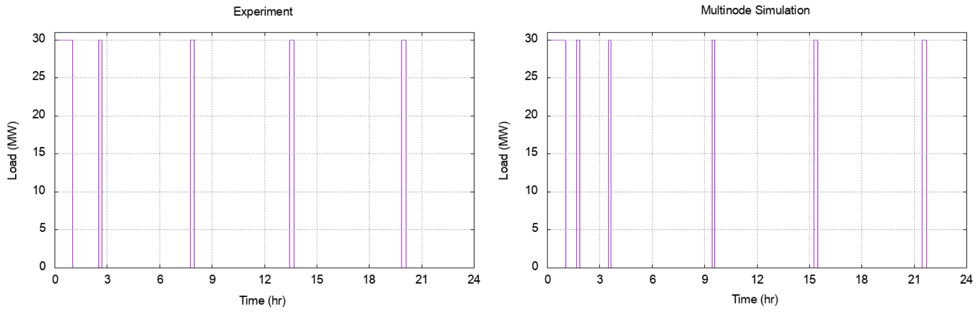

(a) Demand interval window: 0 hrs.

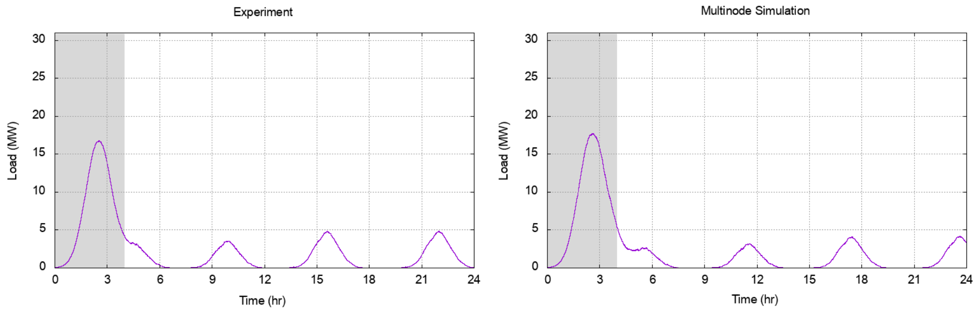

(b) Demand interval window: 4 hrs.

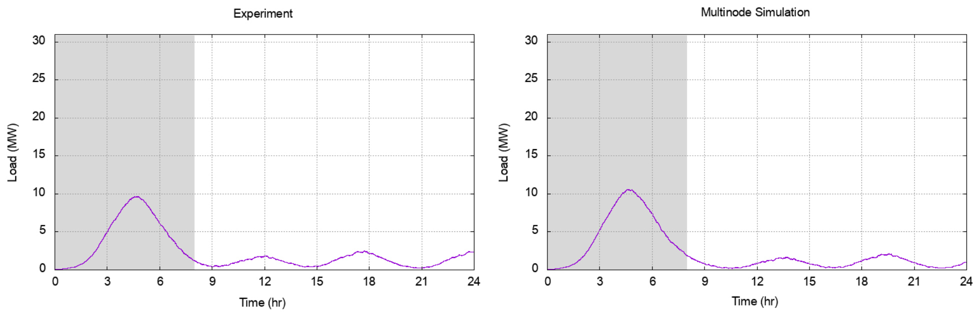

(c) Demand interval window: 8 hrs.

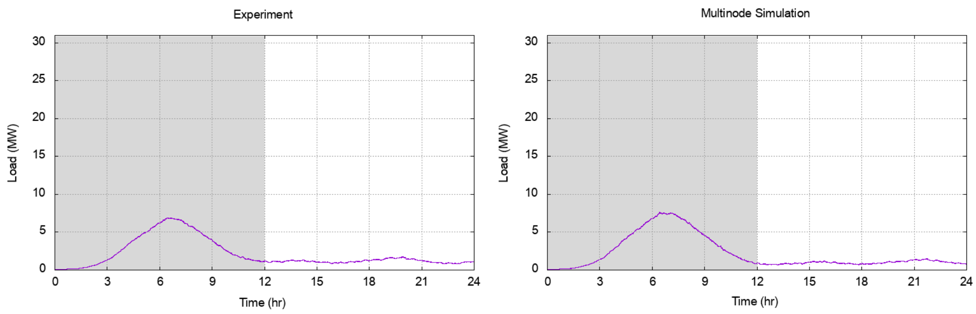

(d) Demand interval window: 12 hrs.

Figure 7.3: Synthesised aggregated load profiles of experiment against simulation of low flow (approx. 30 ℓ/min for a 50 ℓ draw for a EWH population of 10 000 and varying demand windows of [0; 4; 8; 12] hrs.

at 2.56 hrs on the load profile and the peak demand from the simulation is 17.74 MW occurring at 2.59 hrs. This has a peak ratio (P_{sim}/P_{exp}) of 1.06 and a time of peak ratio (t_{sim}/t_{exp}) of 1.01. The simulation overestimates the peak demand by 5.67% and the peak time by 0.99%.

8 hr Demand Interval: The load profiles for a 8 hr demand interval are presented in *Figure 7.3 (c)*. The peak demand from the experiment is 9.66 MW which occurs at 4.76 hrs on the load profile and the peak demand from the simulation is 10.63 MW occurring at 4.63 hrs. This results in a peak ratio (P_{sim}/P_{exp}) of 1.1 and a time of peak ratio (t_{sim}/t_{exp}) of 0.97. The simulation overestimates the peak demand by 9.97% and the peak time is underestimated by 2.87%.

12 hr Demand Interval: The load profiles for a 12 hr demand interval are presented in *Figure 7.3 (d)*. The peak demand from the experiment is 6.91 MW which occurs at 6.63 hrs on the load profile and the peak demand from the simulation is 7.62 MW occurring at 6.43 hrs. This results in a peak ratio (P_{sim}/P_{exp}) of 1.1 and a time of peak ratio (t_{sim}/t_{exp}) of 0.97. The simulation overestimates the peak by 10.38% and underestimates the peak time by 2.93%.

This is a very good match on the peak demand and an exact match on the time of peak occurance. The simulation from the multi-node model consistently overestimates the peak demand in the three varied demand intervals presented within 11%. The time of peak occurrance matches well with the experiment, with ratios close to 1 and very low errors calculated (below 3%).

7.3.3 Load Profiles: 100-Litre Draw at Low Flow Rate

The low flow rate, 100 ℓ draw scenario experiment and simulation from *Section 6.2.3* is aggregated and the synthesized load profiles for a 10 000 EWH population are presented in *Figure 7.4*. *Table 7.1* presents the values for peak demand and peak times. *Figure 7.4 (a)* shows the load profile for 0 hr demand window with a multiplied peak of 30 MW.

4 hr Demand Interval: The load profiles for a 4 hr demand interval are presented in *Figure 7.5 (b)*. The peak demand from the experiment is 27.17 MW which occurs at 3.16 hrs on the load profile and the peak demand from the multi-node model is 25.97 MW occurring at 3.05 hrs. This has a peak ratio (P_{sim}/P_{exp}) of 0.96 and a time of peak ratio (t_{sim}/t_{exp}) of 0.96. The simulation underestimates the peak

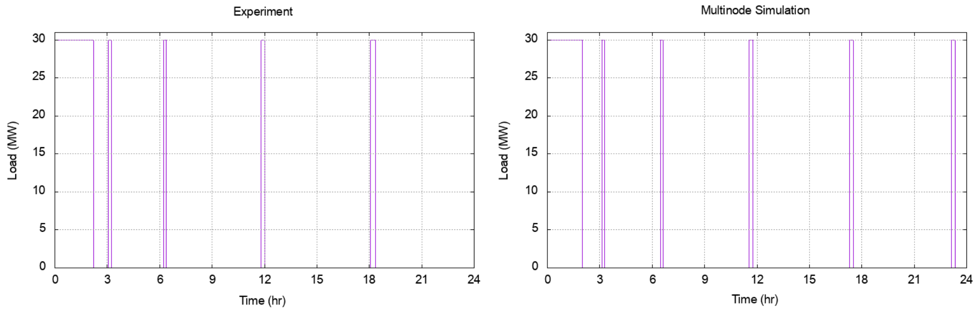

(a) Demand interval window: 0 hrs.

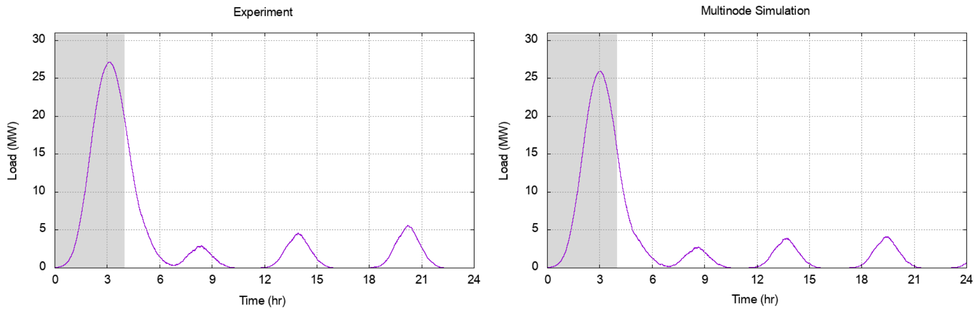

(b) Demand interval window: 4 hrs.

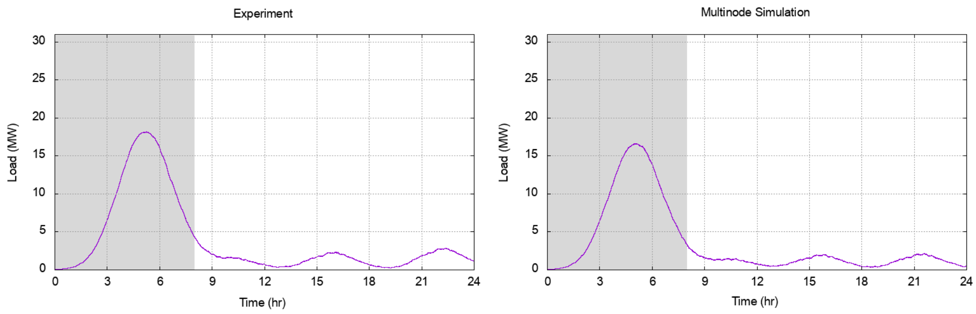

(c) Demand interval window: 8 hrs.

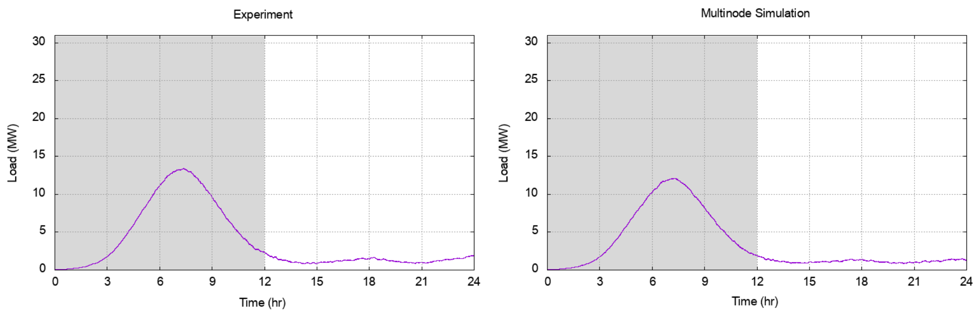

(d) Demand interval window: 12 hrs.

Figure 7.4: Synthesised aggregated load profiles of experiment against simulation of low flow (approx. 8 ℓ/min for a 100 ℓ draw for a EWH population of 10 000 and varying demand windows of [0; 4; 8; 12] hrs.

Table 7.3: Load profile comparison of peak demand and time of peak for experiment and simulations for low flow 100 ℓ draw (refer to *Figure 7.4*).

Feature	**Demand Interval**			
	0 hr	**4 hr**	**8 hr**	**12 hr**
Peak Demand Exp P_{exp} (MW)	30	27.17	18.2	13.41
Peak Demand Sim P_{sim} (MW)	30	25.97	16.66	12.12
Peak Demand Ratio P_{sim}/P_{exp}	1	0.96	0.92	0.9
Error Peak $\frac{P_{sim}-P_{exp}}{P_{exp}} \times 100$ (%)	0	-4.43	-8.46	-9.64
Time of Peak Exp t_{exp} (hr)	0	3.16	5.26	7.37
Time of Peak Sim t_{sim} (hr)	0	3.05	5.04	7.28
Peak Time Ratio t_{sim}/t_{exp}	0	0.96	0.96	0.99
Error Peak Time $\frac{t_{sim}-t_{exp}}{t_{exp}} \times 100$ (%)	0	-3.59	-4.11	-1.25

demand by 4.43% and the peak time by 3.59%.

8 hr Demand Interval: The load profiles for a 8 hr demand interval are presented in *Figure 7.5 (c)*. The peak demand from the experiment is 18.2 MW which occurs at 5.26 hrs on the load profile and the peak demand from the multi-node model is 16.66 MW occurring at 5.04 hrs. This results in a peak ratio (P_{sim}/P_{exp}) of 0.92 and a time of peak ratio (t_{sim}/t_{exp}) of 0.96. This is a very good match on the peak demand and an exact match on the time of peak occurance. The simulation underestimates the peak demand by 8.46% and the peak time is underestimated by 4.11%.

12 hr Demand Interval: The load profiles for a 12 hr demand interval are presented in *Figure 7.5 (d)*. The peak demand from the experiment is 13.41 MW which occurs at 7.37 hrs on the load profile and the peak demand from the simulation is 12.12 MW occurring at 7.28 hrs. This results in a peak ratio (P_{sim}/P_{exp}) of 0.9 and a time of peak ratio (t_{sim}/t_{exp}) of 0.99. The simulation underestimates the peak by 9.64% and the peak time by 1.25%.

The simulation from the multi-node model consistently under-estimates the peak demand in the three varied demand intervals presented within 10%. The time of peak occurrance matches well with the experiment, with ratios close to 1 and very low errors calculated (below 5%).

Table 7.4: Load profile comparison of peak demand and time of peak for experiment and simulations for high flow 100 ℓ draw (refer to *Figure 7.5*).

Feature	Demand Interval			
	0 hr	**4 hr**	**8 hr**	**12 hr**
Peak Demand Exp P_{exp} (MW)	30	25.55	16.28	11.94
Peak Demand Sim P_{sim} (MW)	30	24.27	14.91	10.85
Peak Demand Ratio P_{sim}/P_{exp}	1	0.95	0.92	0.91
Error Peak $\frac{P_{sim}-P_{exp}}{P_{exp}} \times 100$ (%)	0	-5.04	-8.42	-9.17
Time of Peak Exp t_{exp} (hr)	0	2.97	4.97	7.23
Time of Peak Sim t_{sim} (hr)	0	2.85	4.86	7.05
Peak Time Ratio t_{sim}/t_{exp}	0	0.96	0.98	0.98
Error Peak Time $\frac{t_{sim}-t_{exp}}{t_{exp}} \times 100$ (%)	0	-3.94	-2.27	-2.47

7.3.4 Load Profiles: 100-Litre Draw at High Flow Rate

The high flow rate, 100 ℓ draw scenario experiment and simulation from *Section 6.2.4* is aggregated and the synthesized load profiles for a 10 000 EWH population are presented in *Figure 7.5*. *Figure 7.5 (a)* shows the load profile for 0 hr demand window with a multiplied peak of 30 MW.

4 hr Demand Interval: The load profiles for a 4 hr demand interval are presented in *Figure 7.5 (b)*. The peak demand from the experiment is 25.55 MW which occurs at 2.97 hrs on the load profile and the peak demand from the multi-node model is 24.27 MW occurring at 2.85 hrs. This has a peak ratio (P_{sim}/P_{exp}) of 0.95 and a time of peak ratio (t_{sim}/t_{exp}) of 0.96. The simulation underestimates the peak demand by 5.04% and the peak time by 3.94%.

8 hr Demand Interval: The load profiles for a 8 hr demand interval are presented in *Figure 7.5 (c)*. The peak demand from the experiment is 16.28 MW which occurs at 4.97 hrs on the load profile and the peak demand from the multi-node model is 14.91 MW occurring at 4.86 hrs. This results in a peak ratio (P_{sim}/P_{exp}) of 0.92 and a time of peak ratio (t_{sim}/t_{exp}) of 0.98. This is a very good match on the peak demand and an exact match on the time of peak occurance. The simulation underestimates the peak demand by 8.42% and the peak time is underestimated by 2.27%.

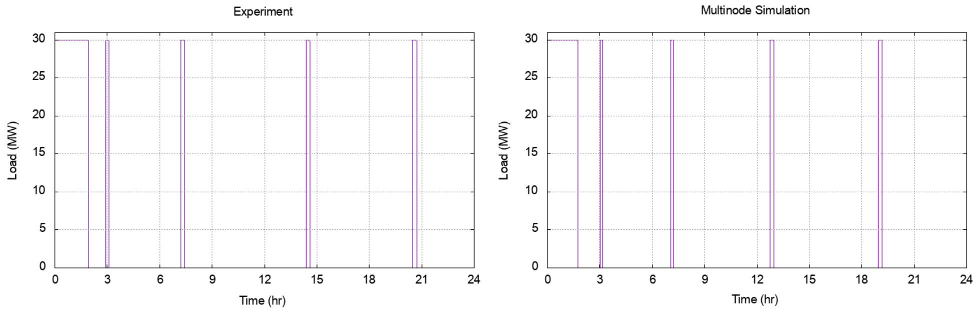

(a) Demand interval window: 0 hrs.

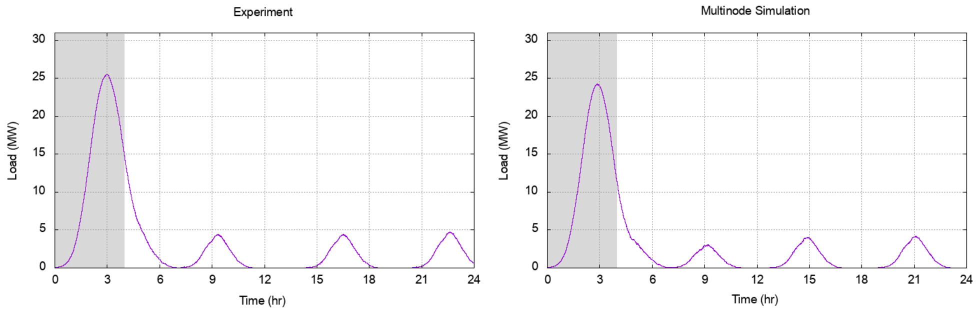

(b) Demand interval window: 4 hrs.

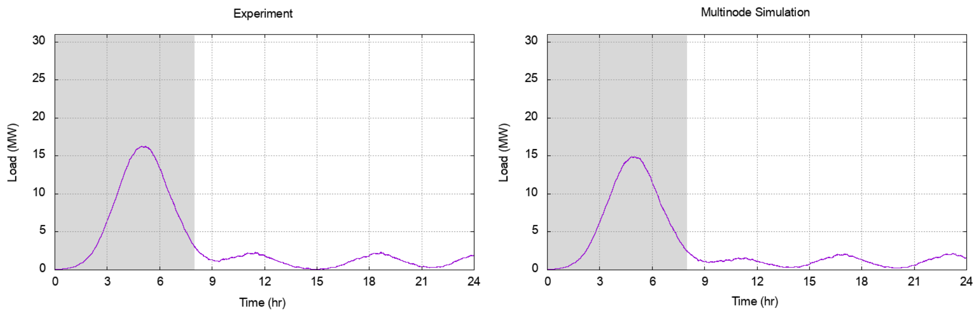

(c) Demand interval window: 8 hrs.

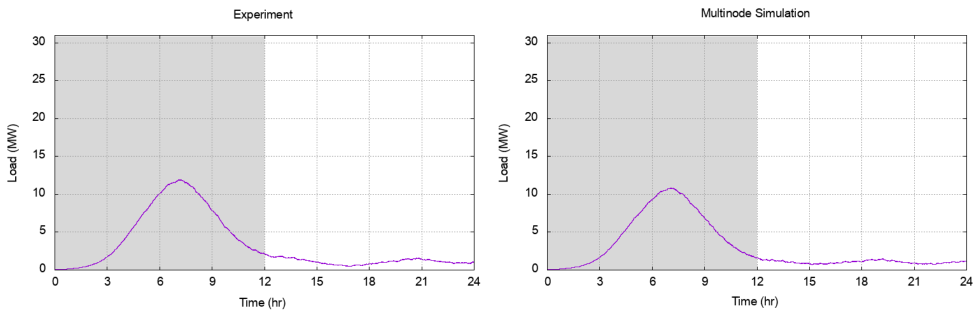

(d) Demand interval window: 12 hrs.

Figure 7.5: Synthesised aggregated load profiles of experiment against simulation of low flow (approx. 30 ℓ/min for a 100 ℓ draw for a EWH population of 10 000 and varying demand window of [0; 4; 8; 12] hrs.

12 hr Demand Interval: The load profiles for a 12 hr demand interval are presented in *Figure 7.5 (d)*. The peak demand from the experiment is 11.94 MW which occurs at 7.23 hrs on the load profile and the peak demand from the simulation is 10.85 MW occurring at 7.05 hrs. This results in a peak ratio (P_{sim}/P_{exp}) of 0.91 and a time of peak ratio (t_{sim}/t_{exp}) of 0.98. The simulation underestimates the peak by 9.17% and the peak time by 2.47%.

The simulation from the multi-node model consistently under-estimates the peak demand in the three varied demand intervals presented within 10%. The time of peak occurrance matches well with the experiment, with ratios close to 1 and very low errors calculated (below 4%).

7.3.5 Peak Demand

The key feature from each of the aggregated load profiles is the ability to predict peak demand loading on the system, which is important for ensuring there is enough supply to meet demand. This feature has been discussed in the load profiles presented previously for 10 000 EWH population for each synthesised scenario and the comparison of each scenario is performed using demand ratios defined in *Equation 7.1*.

This section includes all the considered EWH populations of [10; 100; 1 000; 10 000] or [$1e1$; $1e2$; $1e3$; $1e4$]. The resulting peak power demand ratios are plotted against the EWH population for each demand interval of [0; 4; 8; 12] hrs and presented in *Figure 7.6 (a)-(d)*. The trends are plotted on a log scale (base 10) on the x-axis to account for the large range of EWH populations considered.

Clustering around a ratio of 1 indicates that there is a good match in the predicted first maximum between the load profile synthesised from experimental element trace and the simulated element trace. Points that are greater than 1 indicate that there is an over-prediction, and points that are lower than 1 indicate that there is an under-prediction. In all the graphs, a peak time interval of 0 hrs results in a ϵ_P of 1 for all populations, which is expected. For smaller populations ($1e1$), the ratios appear to be more eratic, with relatively high errors. For larger populations, the ratios appear to converge and stabilise. In general, it is seen that the 50 ℓ draws over-estimate the peak demand, with errors up to 20%. The 100 ℓ draws have more consistency predict within 10% for peak demand. The larger populations have been discussed in further detail in the preceeding sections.

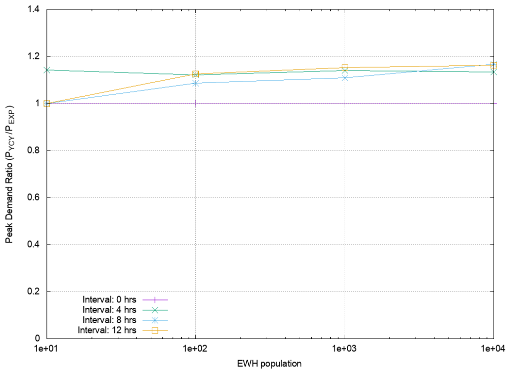

(a) 50 ℓ draw at low flow.

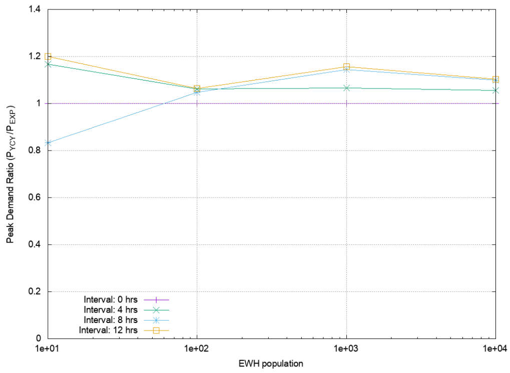

(b) 50 ℓ draw at high flow.

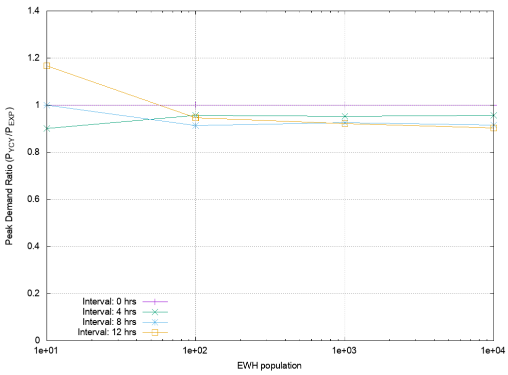

(c) 100 ℓ draw at low flow.

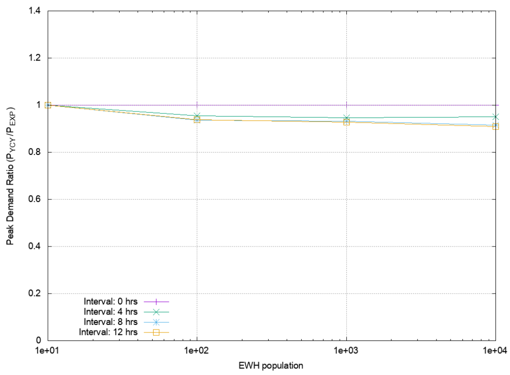

(d) 100 ℓ draw at high flow.

Figure 7.6: Peak power demand ratios for EWH populations [$1e1$; $1e2$; $1e3$; $1e4$] for demand windows [0; 4; 8; 12] hrs.

7.3.6 Energy

The next feature is total energy in the system for a 24-hour interval, which is important for resource planning purposes. The resulting energy ratios for EWH populations of [10; 100; 1 000; 10 000] or [$1e1$; $1e2$; $1e3$; $1e4$] are plotted against the EWH population for each demand interval of [0; 4; 8; 12] hrs and presented in *Figure 7.7 (a)-(d)*. The trends are plotted on a log scale (base 10) on the x-axis to account for the large range of EWH populations considered.

The energy ratio profiles are more stable than the peak demand ratios, which could be due to the accumulating nature of energy calculations. It can be seen that the 50 ℓ at high flow and 100 ℓ at low flow rate draws have the closest overall predicted energy to the experiment. The 50 ℓ draw at low flow consistently over predicts the system energy by approximately 10% and the 100 ℓ high flow draw consistently under-predicts by approximately 15%.

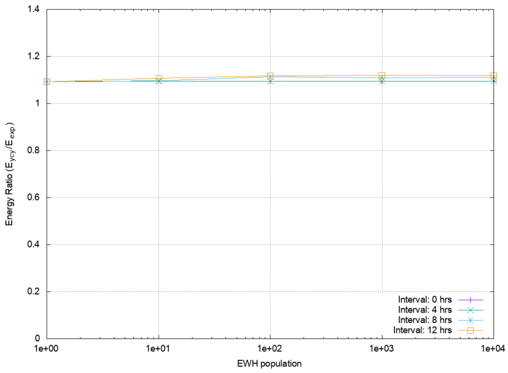

(a) 50 ℓ draw at low flow.

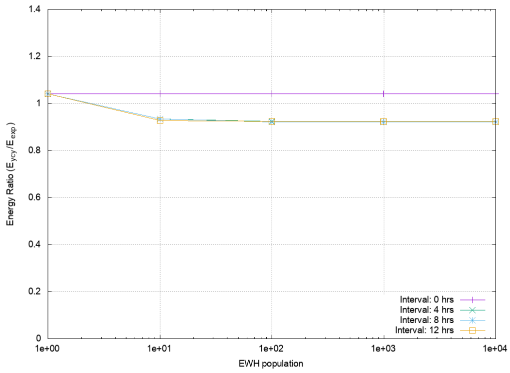

(b) 50 ℓ draw at high flow.

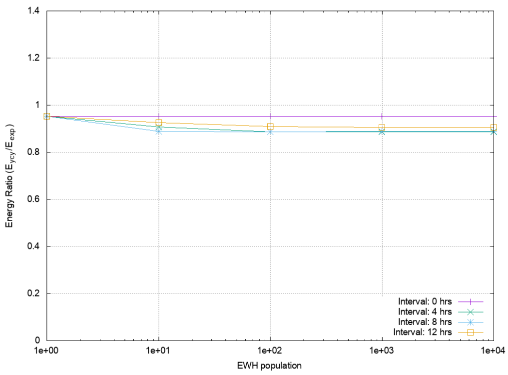

(c) 100 ℓ draw at low flow.

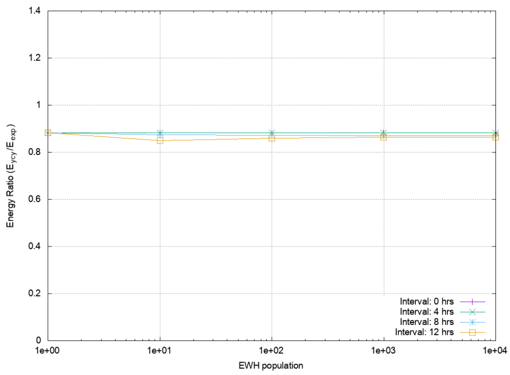

(d) 100 ℓ draw at high flow.

Figure 7.7: Energy ratios for EWH populations $[1e1; 1e2; 1e3; 1e4]$ for demand interval $[0; 4; 8; 12]$ hrs.

7.4 Comparison with Binodal Model Performance

The binodal model implemented for comparison is the horizontal EWH load model by Nel (2015). *Figure 7.8 (a)-(d)* shows the performance of the horizontal binodal model for the four single-draw scenarios presented in this work for direct comparison (using the same experimental data in *Section 6.2.1*,*Section 6.2.2*,*Section 6.2.3*,*Section 6.2.4*). The effective initial temperature of the tank was determined based on volume ratios for each temperature sensor. The implementation of this model included a hysteresis control points between 65 and 70 and thermal resistance of insulation of $25°C$.day/kWh to match the standing loss events. As discussed, the binodal model only replaces energy from a draw in a single element event and then steady-state follows, which is as expected in the model results presented.

The aggregated performance of the multi-nodal simulation outputs were compared against the binodal model. The results are shown in *Figure 7.9* for each time interval

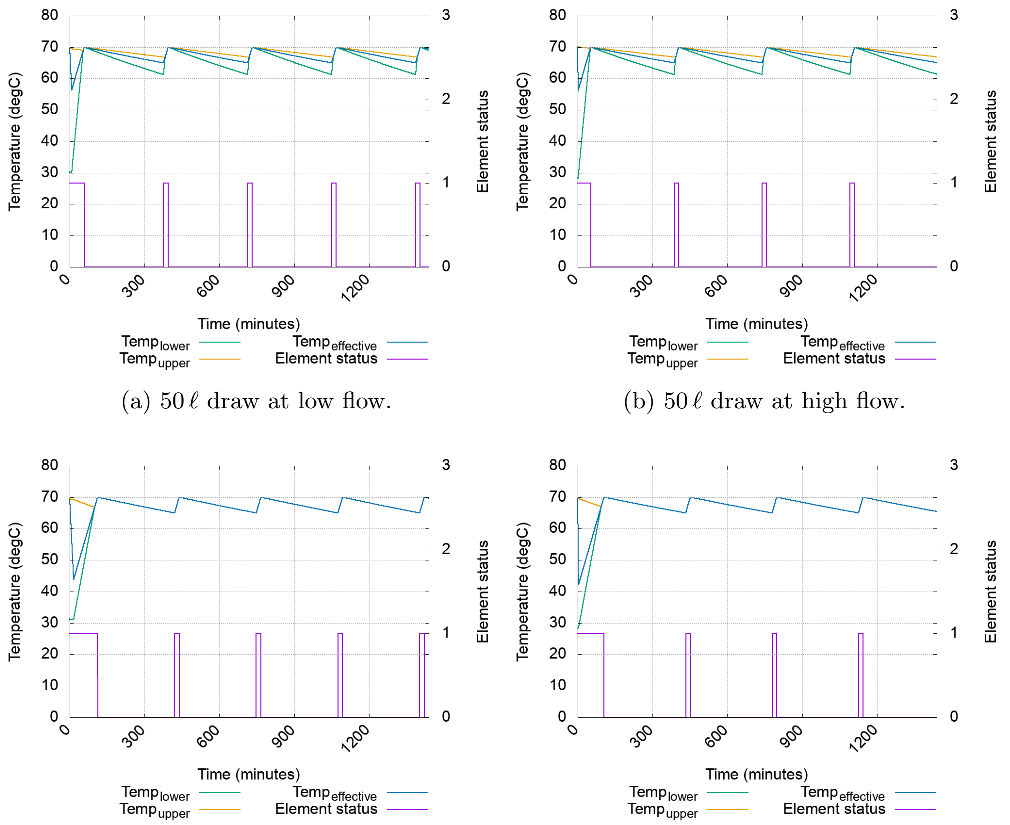

(a) 50 ℓ draw at low flow.

(b) 50 ℓ draw at high flow.

(c) 100 ℓ draw at low flow.

(d) 100 ℓ draw at high flow.

Figure 7.8: Model performance of the horizontal binodal model using draw scenarios from *Chapter 6*.

[0; 4; 8; 12] hrs for a EWH population of $1e4$.

In general, it can be seen that the load profile curve of the multi-node model follows the shape of the experimental curve, as would be expected due to the original element switching profile matching better with the inclusion of the subsequent replacement cycles. For both the 50 ℓ draws, the model over-estimates the peak demand, whereas for the 100 ℓ draws, it under-estimates the peak demand. The steady-state events track very well for the 50 ℓ at low flow draw, with matching demand amplitude and times of occurrance. The other three draws track less well, but consistently predict fairly well for steady-state demand amplitude.

The resulting load profile curve from the binodal model does not display the secondary peak caused by the subsequent replacement cycles. For all four draw types, the model consistently under-predicts the peak demand. The steady-state events generally do not track well for time of occurrance, likely due to the missing subsequent replacement cycles. The peak power values for the steady-state events

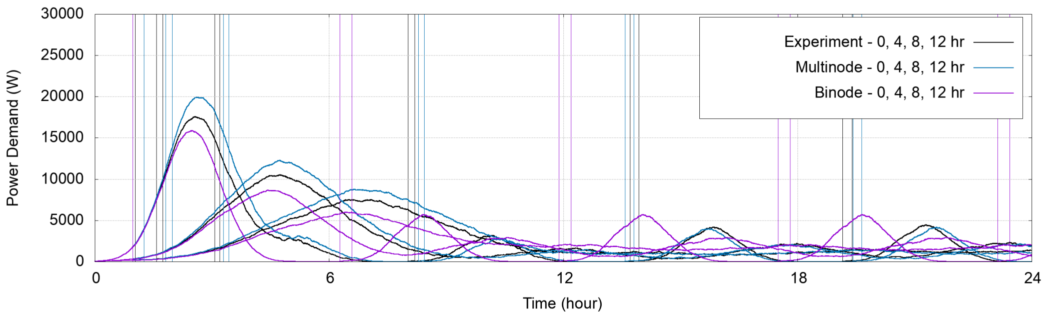

(a) 50 ℓ draw at low flow.

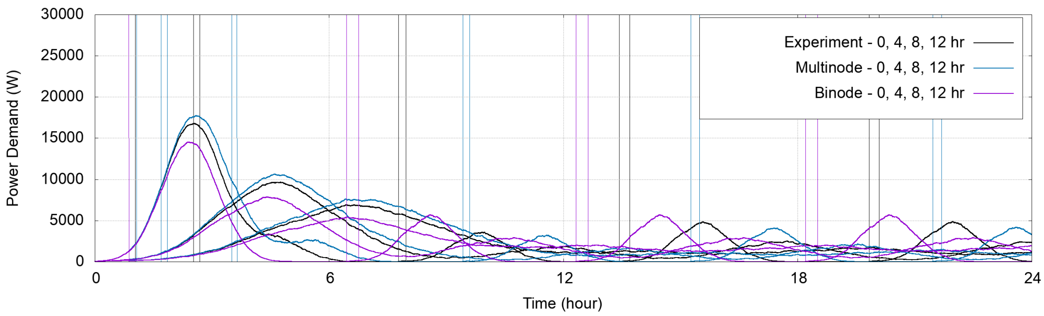

(b) 50 ℓ draw at high flow.

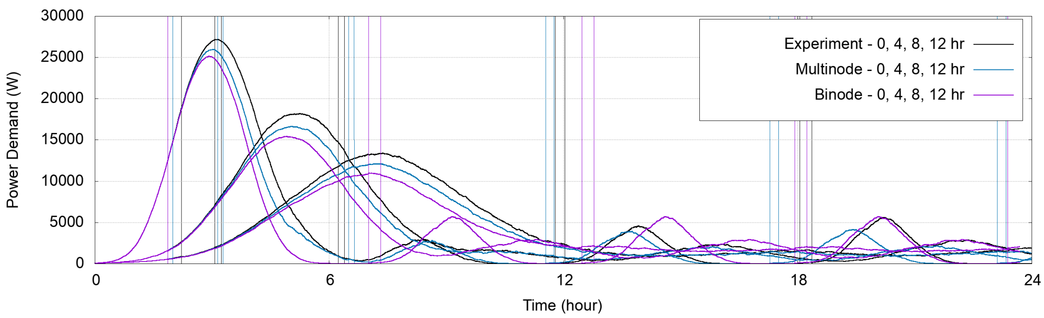

(c) 100 ℓ draw at low flow.

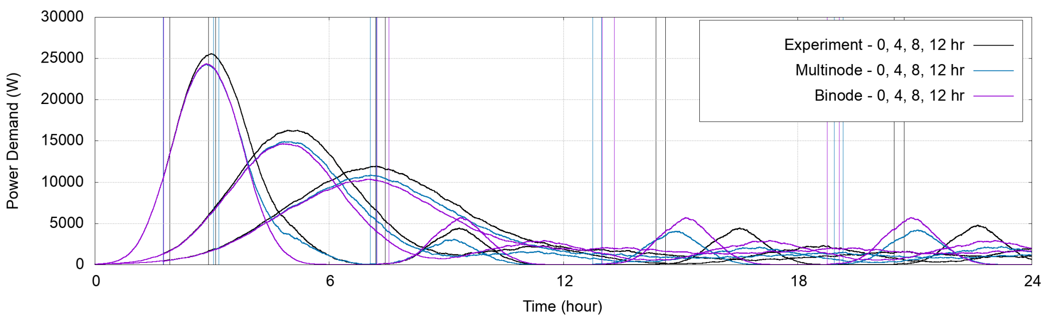

(d) 100 ℓ draw at high flow.

Figure 7.9: Aggregated load profiles comparing performance of the multinode model to the binodal model for an EWH population of $1e4$.

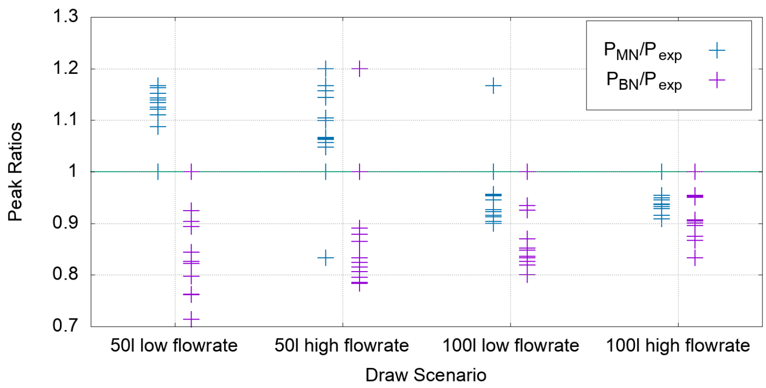

(a) Peak demand ratios.

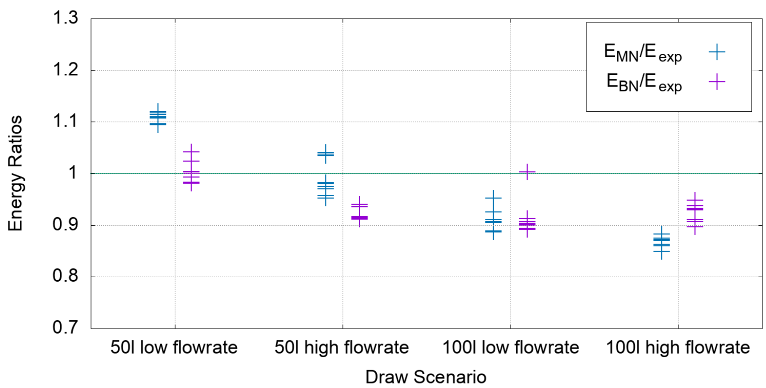

(b) Energy ratios.

Figure 7.10: Comparison of peak demand and energy ratios for multinode (MN) and binodal models (BN) for considered draw scenarios (each data point represents a simulated scenario from the varied EWH populations and peak time interval).

over-predict in value.

The peak demand and total energy comparison of the multi-node model (MN) and the binodal model (BN) set of load profiles from *Figure 7.10*, are summarised in *Figure 7.10 (a)* and *Figure (b)*. The ratios presented include the results from all the simulations performed: EWH populations of $[1e1;\ 1e2;\ 1e3;\ 1e4]$ for demand interval $[0;\ 4;\ 8;\ 12]$ hrs. The information on populations and peak time intervals have been omitted from graph to provide a general overview of trends.

In the summarised peak demand ratios presented in *Figure 7.10 (a)*, the multi-node model shows tighter clustering of the ratios, indicating that the predictions appear within a smaller margin of error. The multi-node model also only has a margin of error within a 20% range, whereas the binodal model exceeds this threshold as shown in both the $50\,\ell$ draw types. Both models appear to perform better for the

$100\,\ell$ draw types.

In the summarised energy ratios presented in *Figure 7.10 (b)*, the binodal model appears to perform more consistently for system energy predictions. The margin of error of predictions are primarily contained within a 10% range. The multi-node model, as discussed in *Section 7.3.6* perform with results within the 15% error range.

7.5 Discussion

The cumulative effects of the aggregated load profiles resulting from multi-node model have been evaluated against the experimental output and in a comparison against the binodal model horizontal model. The factors evaluated include the load profile trend, peak demand predictions, time to peak, total energy of the system for 24 hrs, and steady-state (peaks and time of occurrance). These are discussed in *Section 7.5.1*.

The results are discussed *Section 7.5.2* in context to previously published work and the contribution of the heat replacement cycles are discussed in relation to the predicted peak demands. And finally, the opportunities for demand-side management based on the model outputs will be discussed in *Section 7.6*.

7.5.1 Performance Factors

The aggregated load profiles resulting from the multi-node model match the expected trend of the experimental profiles. In all curves, it is possible to see the curve with a large peak demand amplitude and a smaller secondary peak on its tail end. This was the aim of producing the multi-node model, to ensure that the second demand amplitude could be resolved through the modelling of the subsequent replacement cycles post draw event. It is also clearly indicated that the binodal model does not exhibit this secondary peak in demand, as expected from its single draw replacement event. In less controlled aggregated load simulations, it is likely that the binodal model will underestimate the peak demand where the replacement cycles could produce an unexpected rise in demand predictions.

The peak demand produced by the multi-node model is presented in detail in *Section 7.3.1*, *Section 7.3.2*, *Section 7.3.3*, and *Section 7.3.4*. The performance is also discussed in *Section 7.3.5* and compared with the binodal model in *Section 7.4*. It is seen that prediction of peak power demand predictions are generally reasonable. Some scenarios produce better predictions than others, for instance, the 100 ℓ high flow rate has the best performance around 1 and the 50 ℓ high flow rate has the worst clustering around a ratio of $0.8 - 1.2$, indicating that the peak demand generally falls within 20% of its expected value. The 50 ℓ draw predictions could be improve to produce better predictions. It is considered better in comparison with the binodal model that can produce peak demand predictions over 20% of the expected value.

The predictions for time to peak demand are show every good agreement, as indicated in *Table 7.1*,*Table 7.2*, *Table 7.3* and *Table 7.4*. Most of the results show ratios very close to 1 with error margins that are well within 5% of expected time to peak.

The total energy of the system within a 24 hour period is evaluated for the multi-node model in *Section 7.3.6* and the performance is compared with the binodal model in *Section 7.4*. The performance for the total system energy is within 15% of the expected value. The predictions are more closely clustered with small ranges displaying within each experimental scenario, showing that EWH population and demand interval have little impact on the overall energy, which is expected. However, the binodal model produces better performance for energy predictions, with a smaller range of error (within 10%).

The steady-state events for the aggregated load profiles resulting from the multi-node model have been discussed in *Section 7.4* as a comparison to the binodal model. It has been noted that the draw scenario 50 ℓ at low flow draw matches the steady-state events very well, both in demand amplitude and time of occurrance. In general, the multi-node model produces demand amplitudes similar to the experimental load profiles, whereas the binodal model over-estimates the amplitude. The steady-state events are a supplementary feature to this model and would require further investigation to match correctly. Both models are simulated using a fixed ambient and fixed inlet temperature, which will likely contribute to the resulting standing loss results.

7.5.2 Heat Replacement Contribution to Peak Demand

Yen et al. (2019) produced results showing that the contribution of tank orientation (vertical to horizontal) with same draws could have a maximum aggregated demand ratio of 0.58 (of 40% deviation). The results showed that vertical tanks will over-predict the demand, where a population of primarily horizontally oriented tanks are prevalent. It was therefore postulated that the binodal model performance would similarly over predict the demand due to a similar element switching pattern occurring. This investigation has shown that the binodal model actually under-predicts the peak demand.

It should be noted in the vertically oriented tank that the thermostat is placed either at the bottom or mid-way up the height. This results in the top of the tank producing much higher temperatures than the region around the thermostat, as seen in *Figure 3.4* in *Section 3.2.2*. This results in a longer duration for the primary heat replacement cycle for the vertically oriented tank, resulting in an over-prediction of cumulative peak demand. The binodal model implementation does not consider the upper layers heating more than expected and therefore the element duration for the primary event closely matches the energy balance from the expected draw.

7.6 Opportunities for Demand-Side Management

Peak demand prediction is affected by the draw cycles and the primary event in combination with subsequent events need to be considered, or under-predictions could occur, as has been shown in the binodal model implementation. This indicates that the multi-node model should be considered over the binodal model for cumulative demand predictions. Considering the $50\,\ell$ draw at low flow, approximating a shower from each EWH in the population for a $4-$hour peak demand interval, similar to the South African peak time period, the expected ADMD is 1.75 determined by *Equation 7.4*, where P is the peak demand (W) and N is the number of EWH in the population. The peak demand is presented in Watts as the element is a purely resistive load with a measured power factor of 1. This ADMD value also makes the assumption that all EWH participate within the peak demand interval. This value exceeds ADMD value of 1.3 of controllable load estimated by Beute and Delport (2006).

$$ADMD = \frac{P}{N} \tag{7.4}$$

The ADMD of the multi-node model output is 2, and the ADMD of the binodal model output is 1.5. In this case, the multi-node model over-predicts the ADMD. For a stochastic implementation of this model with the inclusion of time-correlated probability density functions determined for typical hot water usage, greater value may be derived in determining the ADMD due to domestic hot water usage. This is expected to reduce the ADMD values with the inclusion of greater diversity in the system, as not all EWH in the population will elicit a draw event during the peak demand interval.

With the successful implementation of the double-draw scenario in *Section 6.3*, it shows that the developed multi-node model can handle non-ideal scenarios and still predict temperature distributions and element switching events with good agreement. This shows promise for considering the model in an aggregated system with stochastic draws or the inclusion of control strategies, where EWHs will be externally turned off for a period and draw events may still occur on the tank.

The next steps in the use of this model to simulate aggregated system effects is the implementation of the model over longer periods with expected variations implemented for tank parameters, environmental parameters and usage parameters. As an extension to ripple control, external control strategies could be considered for peak load reduction, load-shedding prevention, load-shedding recovery and responsive loading for excess grid supply.

For modelling total system energy, the binodal model has produced better predictions and is simpler to implement. Therefore, the use of the binodal model to determine the expected passive energy savings due to changes regulations could be used reliably. An example of this could include the regulatory change to VC 9006 to a MEPS for Class B tank insulation and its relation to testing procedures in SANS 151.

System effects for solar and heat pump contributions will still need to be considered. The use of the multi-node model is a promising base model for the consideration of including renewable sources with an auxiliary electrical back-up. Reliable models will assist regulators and standards bodies to implement energy regulations that can assist in meeting sustainable goals and give clarity to policy decisions made for setting MEPS.

7.7 Conclusion

This chapter describes a method to investigate the aggregated effects of the simulated load of a horizontally oriented EWH and validate its effectiveness for predicting cumulative peak power demand and time of peak in a system application. Load profiles are produced from the four draw scenarios, by varying the EWH population and peak time intervals. The load profiles are evaluated by a ratio of first peak attributes for the simulated element switching profiles against experimental element switching profiles. The first peak attributes are the peak power demand and time of peak. Energy drawn from the overall system is also evaluated as a ratio.

The performance of the cumulative effects for the multi-node model is compared against the performance of the binodal model. It is shown that the multi-node model prediction of peak power demand is fairly good, with most of the data points falling within the 0.8 ratio (or 20% deviation) of expected value. The binodal model produced consistently weaker predictions with up to 0.7 ratio (or 30% deviation) in peak demand prediction. The multi-node model presents promising results for the time to peak predictions, with error margins within 5% of expected value; the binodal model was not evaluated on this factor. Finally, the multi-node model presents promising results for total energy predictions, with approximately 15% deviation in predictions. However, the binodal model presents better performance on total energy predictions, with predictions closer to 10% deviation.

The next chapter summarises the findings of this work in a conclusion.

Chapter 8

Concluding Remarks

This chapter presents the summary of results from each of the chapters in *Section 8.2* and highlights the key findings from the research work in *Section 8.3*. Further discussions on the extensions for this work are presented in *Section 8.4*. Finally, the concluding remarks made for this thesis is presented in *Section 8.5*.

8.1 Introduction

The objective of this research work was the investigation of the following question:

Can a multi-node model be used to predict element switching in a horizontally-oriented EWH post draw event to produce better peak demand predictions for system loading on a grid in comparison to load models with simpler abstractions?

The following objectives were formulated to attempt to answer the question:

1. To develop a thermostatically controlled load model with a multi-nodal approach for a horizontal EWH with element switching fidelity to resolve subsequent events for variable draws.
2. To predict peak demand for the aggregated system with better overall performance than a binodal model developed for horizontal EWH.

This chapter details the results from the work and finally links the findings to the research question and objectives that were set.

8.2 Summary of Research Work

The EWH was shown to be a good candidate for DSM initiatives for the management of loads on the electrical grid in *Chapter 2*. It has an estimated peak demand equivalent to Stage 3 loadshedding, so targetting these loads could be useful in alleviating the current power demand crises facing the South African power utility. Therefore, a suitable thermal model linked to element switching to produce a load model, which is capable of correctly simulating the unique draw replacement of a horizontally oriented EWH is necessary to simulate DSM scenarios. Simplifying the 3D volume to a 1D temperature gradient is a common approach for abstracting thermal stratification. Thermal models linked to load models in the literature have been shown to oversimplify the thermal processes and not sufficiently reproduce the transient nature of the loads due to draw replacement seen in horizontal tanks.

In *Chapter 3*, it was identified that the geometry of the horizontally oriented tank and the placement of the internal components, specifically, the element and thermoprobe, result in the unique draw replacement load profile of the element. This replacement profile consists of a primary replacement event, followed by several subsequent replacements before steady-state is reached. The multinodal approach was chosen for its ability to resolve a flexible degree of stratification, which was expected for the resolution of the subsequent replacement events observed in the horizontal measurements. It was also chosen for its relatively low computation time. The draw events chosen to validate the model was also discussed. All these decisions were made in the context of the research question and the stated objectives.

The draw replacement of four draw scenarios was characterised in terms of the element ON/OFF state durations in *Chapter 4*. This was done in comparison with steady-state characterisations. The draw scenarios were as follows: $50\,\ell$ draw low flow rate, $50\,\ell$ draw high flow rate, $100\,\ell$ draw low flow rate and $100\,\ell$ draw high flow rate. Variations in the durations of each element state were observed using three instances of each set of draw parameters. It was found that if the t_{ON} duration was lower than durations of steady-state counterparts, then the element event is part of the draw replacement. Similarly, if the t_{OFF} duration was lower than durations of steady-state counterparts, then the element event is part of the draw replacement. It was noted that of the draw events considered, which consider a wide range of operational states, a maximum of two subsequent replacement cycles post draw occurred for the element. This consideration was taken into account for the choice of simulated layers.

A 1D multi-node model for a horizontally oriented EWH was developed with the use of 24 thermal layers inside the water volume in *Chapter 5*. The model accounts for the three operational states of a tank: draw, heating and cooling. Heat transfer processes were included in the model and coefficients were determined heuristically from a control case. Due to a fixed water density assumption, mixing processes in the tank are handled through tank states and heat transfer coefficients that affect chosen layers. Buoyancy effects are handled through the perfect homogenisation of temperature layers if layers lower in the structure produce a higher temperature, thus avoiding a temperature inversion. Reduction of number of layers and computation time are proposed with the application of mass transfer through a variable water density.

In *Chapter 6*, the multi-node model and its heuristically determined parameters is tested and validated against three additional single-draw scenarios and a double draw scenario. Three of the four single-draw scenarios showed promise, with good matching on each element state. One test scenario (50 ℓ high flow) produced an additional subsequent replacement event, which affected the relative errors in the analysis, but produced viable features with a high visual match over a 24-hour period. The double-draw event consisted of two 25 ℓ draws with a 10 min separation between events.

The aggregated effects of the load profiles from each draw scenario were investigated in *Chapter 7*. Comparative load profiles were produced from the experimental element switching profile and the simulated element switching profile, by varying the EWH population and peak time intervals. These cumulativeload profiles were compared using a ratio of the first peak attributes (maximum demand and time of occurance) and total system energy. The prediction of peak power demand was fairly good, with most of the data points falling within the 20% deviation of expected value. The prediction of time of occurance shows promise, with many data points falling within the 5% deviation from expected values. The total system energy is predicted within 15% of expected values. A comparison is made to a binodal model; the multi-node model is shown to produce a better prediction performance for the peak demand.

8.3 Findings

The key findings from the research work can be summarised as follows:

1. Significant variations exist between experimental measurements with same draw volume and flow rate (*Chapter 4*).

2. Results from the multi-node model to predict layer temperatures and element switching events adequately matches measured experiments for controlled single-draw events and a realistic double-draw event (*Chapter 5* and *Chapter 6*), indicating the approach used for mixing processes shows promise.

3. The cumulative results for the two $50\,\ell$ draw scenarios produced higher deviations for the multi-node model. The low flow scenario over-predicted the primary element duration, causing an over-prediction in the scaled aggregation. The high flow scenario produced an additional replacement event, which produced high relational errors to experiment; however, the results from the scaled aggregation showed a minor over-prediction, likely due to the additional replacement event (*Chapter 6* and *Chapter 7*).

4. The aggregated load profiles for (a large range of populations and peak interval periods) produced from the multi-node model predicts the peak demand within 20% deviation, time to peak within 5% deviation and total energy within 15% deviation (*Chapter 7*).

5. The binodal model is shown to consistently under-estimate the peak demand predictions, indicating that the consideration for the subsequent replacement events needs to be taken into account for system aggregation (*Chapter 7*).

6. The multi-node model is shown to perform better than the binodal model for cumulative peak demand predictions (*Chapter 7*).

7. The aggregated load profiles produced from the binodal model is adequate for system energy predictions (*Chapter 7*).

8.4 Future Work

The multi-node model developed has been shown to produce reasonable fidelity in temperature and element switching predictions for the considered draw scenarios. However, some improvements could be considered for future implementation of this base-model:

- Identify factors affecting $50\,\ell$ draws for better draw replacement predictions.

- Model computation time for multi-node model can be reduced for consideration of scaled aggregated systems with the incorporation of unique qualities such as varying ambient temperatures, inlets, EWH design.
- Model fidelity can be improved with consideration of thermal parameters that can be validated. Consideration for incorporating mixing processes that can reduce number of layers and improve compuation time. Possibly even improve temperature fidelity in layers.
- For usage in single-item modelling, further investigation can be considered to ensure model fidelity at a micro-scale.
- Further investigation into single-item energy considerations to improve cumulative results in for the aggregated system.

To implement a base model towards understanding cumulative system effects through load aggregation, the following improvements, functionality and investigations can be considered:

- Consider typical draws and typical EWH parameters with variations. This would require a deeper study into the variation of subsequent events on the EWH across a variety of designs.
- Integration with a vertical model for modelling country considerations.
- Implementation of a stochastic model based on determined probabilities of hot water draw.
- Investigation of control strategies for load shifting and load-shedding mitigation using EWH models.
- Consider effectiveness of domestic ToU.
- Incorporate feedback control for state-of-charge in EWH to ensure user comfort with proposed control strategy.

Expansion of the research work with the consideration of the base model and its implementation of aggregation effects could be considered for the following future applications:

- Measure a statistically relevant number of households from different living standard measures to determine a typical hot water usage profile that is time-correlated (for future grid considerations) and for the development of a relevant energy usage test method for SANS 151 for VC 9006 regulations.
- Extension of base model to domestic solar powered or heat-pump supplied TES with element auxillary to provide clarity on grid loading for the development of energy policy in relation to VC 9006 regulation.

8.5 Conclusion

In concluding the research work, the two objectives are discussed to consolidate towards the research question.

The first objective was to develop a thermostatically controlled load model with a multi-nodal approach for a horizontal EWH with element switching fidelity to resolve subsequent events for variable draw volumes and flow rates. This was done with success, where 3 out of 4 single-draw scenarios showed good agreement, both in simulated temperatures and the element switching events. The unsuccessful scenario overall, still provided reasonable visible agreement and produced fair predictions for the peak demand considerations. A realistic draw profile also shows promising results. Future work can improve the base model for better switching fidelity and lower computation time.

The second objective was to predict peak demand for the aggregated system with better overall performance with the developed multi-node model in comparison to a model with a simplified thermal abstraction (binodal model). The multi-node model produced aggregated load profiles with high fidelity to the expected load profiles from experiments. It also produced better predictions of the cumulative peak demand than the binodal model, which produced an underprediction due to the lack of additional element switching events during heat replacement of a draw.

These two objectives were derived from the research question: *Can a multi-node model be used to predict element switching in a horizontally-oriented EWH post draw event to produce better peak demand predictions for system loading on a grid in comparison to load models with simpler abstractions?* Based on the findings of this research work, it has been affirmed that the multi-node model can predict the element switching patterns observed in the horizontal tank (from first objective) and the resulting load profiles produce better peak demand predictions in aggregated systems than the binodal model which is an EWH load model with a simpler abstraction.

Therefore, this represents a valuable and novel contribution to the development of simulated, computationally-inexpensive, load forecasting tools for thermostatically controlled EWH that demonstrate transient loading effects as evident in horizontally tanks and shows the potential for better predictions of cumulative effects on the grid for a large populations, which is important in the development of DSM strategies.

References

Alizadeh, S. (1999). An experimental and numerical study of thermal stratification in a horizontal cylindrical solar storage tank. *Solar Energy*, 66(6):409–421.

Arteconi, A., Hewitt, N., and Polonara, F. (2013). Domestic demand-side management (DSM): Role of heat pumps and thermal energy storage (TES) systems. *Applied Thermal Engineering*, 51(1-2):155–165.

ASHRAE (2003). 2003 ASHRAE Applications Handbook (SI). *American Society of Heating, Refrigerating and Air-Conditioning Engineers*.

Baker, J. (2008). New technology and possible advances in energy storage. *Energy Policy*, 36(12):4368–4373.

Bekker, B., Eberhard, A., Gaunt, T., and Marquard, A. (2008). South Africa's rapid electrification programme: Policy, institutional, planning, financing and technical innovations. *Energy Policy*, 36(8):3125–3137.

Beute, N. and Delport, J. (2006). An historic overview of controlling domestic water heating. In *Proceedings of the 14th Domestic Use of Energy Conference*, pages 41–46.

Boivin, J.-Y. (1995). Demand side management - The role of the power utility. *Pattern Recognition*, 28(10):1493–1497.

BusinessTech (2020). City power is switching off heavy power users: Here's how to calculate how much electricity you are using. `https://businesstech.co.za/news/energy/371104/city-power-is-switching-off-heavy-power-users-heres-how-to-calculate-how-much-electricity-you-are-using/`. Online; published 5 February 2020.

Campos Celador, A., Odriozola, M., and Sala, J. (2011). Implications of the modelling of stratified hot water storage tanks in the simulation of CHP plants. *Energy Conversion and Management*, 52(8-9):3018–3026.

Cheung, S., Vorajee, M. H., and Yen, Y.-C. J. (2017). Aggregated load modelling for all electric water heaters in SA: Analytical energy-based and state-queuing model. In *South African Universities Power Engineering Conference (SAUPEC)*, pages 6–11, Johannesburg, South Africa.

City Power (2020). Joburg tariffs 2019/2020. https://www.joburg.org.za/documents_/Documents/TARIFFS/Tariffs/big%20%20tariff.pdf/. Online; last accessed 23 September 2020.

Climate Change News (2020). Which countries have a net zero carbon goal? https://www.climatechangenews.com/2020/09/17/countries-net-zero-climate-goal/. Online; published 17 September 2020.

Delport, G. J. (2005). The geyser gadgets that work/do not work. In *Domestic Use of Energy*.

Dolan, P. S., Nehrir, M. H., and Gerez, V. (1996). Development of a Monte Carlo based aggregate model for residential electric water heater loads. *Electric Power Systems Research*, 36(1):29–35.

Eames, P. C. and Norton, B. (1998). The effect of tank geometry on thermally stratified sensible heat storage subject to low Reynolds number flows. *International Journal of Heat and Mass Transfer*, 41(14):2131–2142.

ee Publishers (2015). Time of use tariffs for the residential sector. https://www.ee.co.za/article/time-use-tariffs-residential-sector.html. Online; published 12 March 2015.

Ericson, T. (2009). Direct load control of residential water heaters. *Energy Policy*, 37(9):3502–3512.

Eskom (2013). 1317 geyser fact sheet. http://www.eskom.co.za/sites/IDM/Documents/1317_geyser_fact_sheet_no_rmr.pdf. [Online; accessed 2015-10-28].

Eskom (2020). What is load shedding? https://loadshedding.eskom.co.za/loadshedding/description. [Online; accessed 2020-09-27].

Farooq, A. A., Afram, A., Schulz, N., and Janabi-Sharifi, F. (2015). Grey-box modeling of a low pressure electric boiler for domestic hot water system. *Applied Thermal Engineering*, 84:257–267.

Fernández-Seara, J., Uhía, F. J., and Sieres, J. (2007a). Experimental analysis of a domestic electric hot water storage tank. Part I: Static mode of operation. *Applied Thermal Engineering*, 27(1):137–144.

Fernández-Seara, J., Uhía, F. J., and Sieres, J. (2007b). Experimental analysis of a domestic electric hot water storage tank. Part II: dynamic mode of operation. *Applied Thermal Engineering*, 27(1):137–144.

Forlee, C. (1996). Residential load research: The Eskom way. In *Domestic Use of Electrical Energy*, pages 95–101, Cape Technikon.

Hall, P. J. (2008). Energy storage: The route to liberation from the fossil fuel economy? *Energy Policy*, 36:4363–4367.

Haller, M. Y., Cruickshank, C. A., Streicher, W., Harrison, S. J., Andersen, E., and Furbo, S. (2009). Methods to determine stratification efficiency of thermal energy storage processes - Review and theoretical comparison. *Solar Energy*, 83(10):1847–1860.

Han, Y., Wang, R., and Dai, Y. (2009). Thermal stratification within the water tank. *Renewable and Sustainable Energy Reviews*, 13(5):1014–1026.

Hargreaves, T., Nye, M., and Burgess, J. (2010). Making energy visible: A qualitative field study of how householders interact with feedback from smart energy monitors. *Energy Policy*, 38(10):6111–6119.

Hargreaves, T., Nye, M., and Burgess, J. (2013). Keeping energy visible? Exploring how householders interact with feedback from smart energy monitors in the longer term. *Energy Policy*, 52:126–134.

Hasnain, S. (1998a). Review on sustainable thermal energy storage technologies, Part I: heat storage materials and techniques. *Energy Conversion and Management*, 39(11):1127–1138.

Hasnain, S. (1998b). Review on sustainable thermal energy storage technologies, Part II: cool thermal storage. *Energy Conversion and Management*, 39(11):1139–1153.

Hohne, P. A., Kusakana, K., and Numbi, B. P. (2019). A review of water heating technologies: An application to the South African context. *Energy Reports*, 5:1–19.

Kempton Express (2013). Ripple control still works. `https://kemptonexpress.co.za/8685/ripple-control-still-works-2/`. Online; published 12 July 2013.

Klein, S. A., Duffie, J. A., Mitchell, J. C., Kummer, J. P., Thornton, J. W., Bradley, D. E., Arias, D. A., Beckman, W. A., Duffie, N. A., Braun, J. E., Urban, R. E., Blair, N. J., McDowell, T. P., Duffy, M. J., Mitchell, J. W., Freeman, T. L., Evans, B. L., Fiksel, A., Williams, P. M., and Kummert, M. (2009). *TRNSYS 17*, volume 4. Solar Energy Laboratory, University of Wisconsin-Madison.

Kleinbach, E. M., Beckman, W. A., and Klein, S. A. (1993). Performance study of one-dimensional models for stratified thermal storage tanks. *Solar Energy*, 50(2):155–166.

Kondoh, J., Lu, N., and Hammerstrom, D. J. (2011). An evaluation of the water heater load potential for providing regulation service. *IEEE Transactions on Power Systems*, 26(3):1309–1316.

Lane, I. E. and Beute, N. (1996). A model of the domestic hot water load. *IEEE Transactions on Power Systems*, 11(4):1850–1855.

Leeuwner, L. L., Naude, N. H., Roux, M., and Booysen, M. J. (2017). Evaluation of the Energy Model of a Horizontally-Mounted Electric Water Heater Through

Internal Temperature Measurement. In *IEEE Innovative Smart Grid Technologies - Asia (ISGT-Asia)*, number June 2018.

Lu, N., Chassin, D. P., and Widergren, S. E. (2005). Modeling uncertainties in aggregated thermostatically controlled loads using a state queueing model. *IEEE Transactions on Power Systems*, 20(2):725–733.

Lutz, J. D. and Yen, Y.-C. J. (2020). Review of SANS 151 : Suitability for regulating energy in water heaters and allowance for innovations. Technical Report May, Commissioned by DMRE S&L Programme and prepared for South African Bureau of Standards (SABS), Johannesburg, South Africa.

Marsaglia, G. and Tsang, W. W. (2000). The ziggurat method for generating random variables. *Journal of Statistical Software, Articles*, 5(8):1–7.

McNeil, M., Covary, T., and Vermeulen, J. (2014). South Africa Geyser : Cost-Efficiency Technical Study. Technical report, Commissioned by the Super-Efficient Appliance and Equipment Deployment Programme (SEAD) to support South Africa's S&L programme, Johannesburg, South Africa.

Meyer, J. P. and Tshimankinda, M. (1996). Domestic hot water consumption by developing communities in South African traditional houses. *Energy*, 21(12):1101–1106.

Meyer, J. P. and Tshimankinda, M. (1998). Domestic hot-water consumption in South African apartments. *Energy*, 23(1):61–66.

Nel, P., Booysen, M., and van der Merwe, A. (2016). A computationally inexpensive energy model for horizontal electric water heaters with scheduling. *IEEE Transactions on Smart Grid*, 9(1).

Nel, P. J. C. (2015). *Rethinking electrical water heaters.* PhD thesis, Stellenbosch University.

Nicotra, M., Caldera, M., Leone, P., and Zanghirella, F. (2018). Model-based analysis of thermal energy storage for multiple temperature level heat supply. *Applied Thermal Engineering*, 141(May):288–297.

Oxfordshire County Council (2019). Climate action for a thriving oxfordshire. `https://www.oxfordshire.gov.uk/sites/default/files/file/about-council/CIimateActionDeclaration.pdf`. Online; last accessed 26 September 2020.

Palensky, P., Kupzog, F., Zaidi, A. A., and Zhou, K. (2008). Modeling domestic housing loads for demand response. In *Proceedings - 34th Annual Conference of the IEEE Industrial Electronics Society, IECON 2008*, pages 2742–2747.

Pearlman, M. and Mills, B. (1985). Development of residential hot water use patterns. *ASHRAE Transactions*, 91(2A):657–679.

Popoola, O. M. and Burnier, C. (2014). Solar water heater contribution to energy savings in higher education institutions : Impact analysis. *Journal of Energy in Southern Africa*, 25(1):51–58.

Rahman, A., Smith, A. D., and Fumo, N. (2016). Performance modeling and parametric study of a stratified water thermal storage tank. *Applied Thermal Engineering*, 100:668–679.

Rautenbach, B. and Lane, I. (1993). A discomfort minimization controller model for domestic water heating. In *Domestic Use of Electrical Energy (DUE)*, pages 75–79.

Rautenbach, B. and Lane, I. E. (1996). The multi-objective controller: a novel approach to domestic hot water load control. *IEEE Transactions on Power Systems*, 11(4):1832–1837.

SA Department of Environmental Affairs (2020). South africa's low emission development strategy 2050. `https://www.environment.gov.za/sites/default/files/docs/2020lowemission_developmentstrategy.pdf`. Online; published Feburary 2020.

SA National Planning Commission (2020). National development plan 2030 - executive summary. `https://www.gov.za/sites/default/files/Executive%20Summary-NDP%202030%20-%20Our%20future%20-%20make%20it%20work.pdf`. Online; accessed 30 September 2020.

SANS 151 (2013). Fixed electric storage water heaters. *South African National Standard*, 7.1.

Schlör, H., Fischer, W., and Hake, J. F. (2012). The meaning of energy systems for the genesis of the concept of sustainable development. *Applied Energy*, 97:192–200.

StatsSA (2016). Community survey 2016 - statistical release. *Statistics South Africa, Private Bag X44, Pretoria 0001*, P0301:81.

Terblanche, U. (2018). Standards and Labelling: A Study on the Impact of VC9006 and the lack of compliance. Technical Report June 2019, Prepared for South African Bureau of Standards (SABS), Johannesburg, South Africa.

Vrettos, E., Koch, S., and Andersson, G. (2012). Load Frequency Control by Aggregations of Thermally Stratified Electric Water Heaters. In *3rd IEEE PES Innovative Smart Grid Technologies Europe*, pages 1–8, Berlin.

Willis, R. M., Stewart, R. A., Panuwatwanich, K., Jones, S., and Kyriakides, A. (2010). Alarming visual display monitors affecting shower end use water and energy conservation in Australian residential households. *Resources, Conservation & Recycling*, 54(12):1117–1127.

Yen, Y.-C. J., Nixon, K. J., and Cronjé, W. A. (2017). Experimental results of energy usage for an electric water heater in vertical and horizontal orientation under steady-state conditions. In *South African Universities Power Engineering Conference (SAUPEC)*, pages 707–712, Stellenbosch, South Africa.

Yen, Y.-C. J., Nixon, K. J., and Cronjé, W. A. (2018a). Comparison of aggregated effects of a 50% experimental draw event in a vertical and horizontal EWH. In *South African Universities Power Engineering Conference (SAUPEC)*, Johannesburg, South Africa.

Yen, Y.-C. J., Nixon, K. J., and Cronjé, W. A. (2018b). Volume segmentation in a stratified vertical EWH tank using steady-state element cycles for energy balance. In Sayigh, A., editor, *Transition Towards 100% Renewable Energy: Selected Papers from the World Renewable Energy Congress WREC2017*, pages 481–489. Springer International Publishing AG.

Yen, Y.-C. J., Nixon, K. J., and Cronjé, W. A. (2019). Maximum Demand Comparison of Aggregated Load Profiles for Vertical and Horizontal EWHs Due to a Fixed Draw Event. *SAIEE Africa Research Journal*, 110(3):167–174.

Young, M. F. and Baughn, J. W. (1981). An Investigation of Thermal Stratification in Horizontal Storage Tanks. *Journal of Solar Energy Engineering*, 103(4):286–290.

Zhang, W., Kalsi, K., Fuller, J., Elizondo, M., and Chassin, D. (2012). Aggregate model for heterogeneous thermostatically controlled loads with demand response. In *IEEE Power and Energy Society General Meeting*, pages 1–8, San Diego, CA, USA.

Appendix A

Experiments

This appendix covers the system design for the testing setup in *Section A.1*, which includes details on the set up and the EWH under test. The calibration of measured quantities are also presented in this appendix in *Section A.2*.

A.1 System Design

To complete this project, certain key components needed to be put in place. This includes the establishment of a testing platform and designing of a measuring system. *Figure A.1* shows a schematic of the platform set up.

The incoming water is fed by municipal water at a fluctuating water pressure of $200 - 600\,\mathrm{kPa}$. The water is regulated to the standard $300\,\mathrm{kPa}$ as it feeds to the manifold. The manifold feeds four inlet valves that can operate individual hot water cylinder installations, as indicated by Valve $1 - 4$. This allows for side-by-side testing and individual tests that can run in parallel. For the duration of any draw experiment, no other EWHs were operated through Valves $2 - 4$ to ensure flow rates would not be affected. All plumbing components are joined through insulated flexible 3/4” diameter pipes. The choice of these pipes instead of copper pipes allow for convenient changes to be made to the set up when required.

The EWH inlet is fed from the manifold, which has a manually-operated flow-control valve (with numbered settings) to control flow rate with a non-return valve and a pressure release valve in-line. Water is heated by the EWH and exits from the outlet to a water catchment load. A draw event is initiated by opening both Valve 1 and Valve 5. Valve 5 is present in the system for redundancy.

The electrical circuit connects the element and thermostat to municipal mains with an AC supply of 230 V, 50 Hz. Most EWHs have built-in thermostat control, which operates the element based on a thermostat measurement to a pre-set temperature threshold. The thermostat is controlled through a measured temperature in the tank T_t on the thermoprobe. If the thermoprobe measures a high enough temperature, the thermostat changes the state of the switch s_1 to open therefore allow no current flowing to the element. Conversely, if the thermoprobe measures a low temperature, the thermostat changes the state of s_1 to closed, resulting in current flowing to the element. Switching states of the element are discussed in more detail in *Section 2.4.1* and *Section 5.4*.

Draw events can be controlled manually through Valve 1 and 5. The flow rate for the draw events is controlled with a flow-control valve with a numbered rotational dial. The drawn off water is dispensed into a load container that is connected to a load cell to measure the mass of the water drawn off from the cylinder. Valve 6 releases the water in the load container for a new load measurement.

The thermal expansion of water is calculated to $1.5\,\ell$ for a δT of 50°C and an expansion coefficient of 210×10^{-6}, which is 1% of the system capacity. To achieve a closed loop system, the pressure relief valve is set to minimise the expansion of water from exiting the system. This experiment is operated under qualified technical support in laboratory conditions.

A.1.1 The Testing Platform

The testing facility for hot water storage systems is situated in the Genmin Laboratory at the University of the Witwatersrand (Wits), Johannesburg. This facility is designed to be fully configurable and modular, with future plans for full automation of the operations and data capture. *Figure A.2* shows photographs of the testing platform with a $100\,\ell$, 2 kW horizontally mounted EWH cylinder fed by the manifold using flexible insulated piping.

The platform allows for customisable hot water cylinder installations, which include horizontal and vertical cylinder orientations and for different volumes of cylinders. This is due to the movable mounting bracket design of the platform.

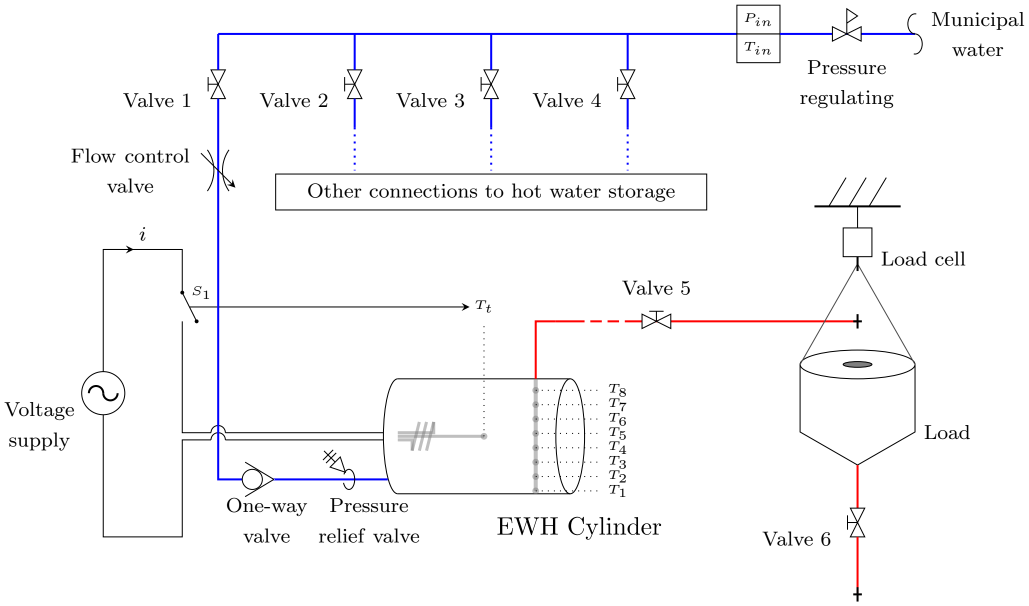

Figure A.1: Schematic of EWH testing platform with design components for measurement and control.

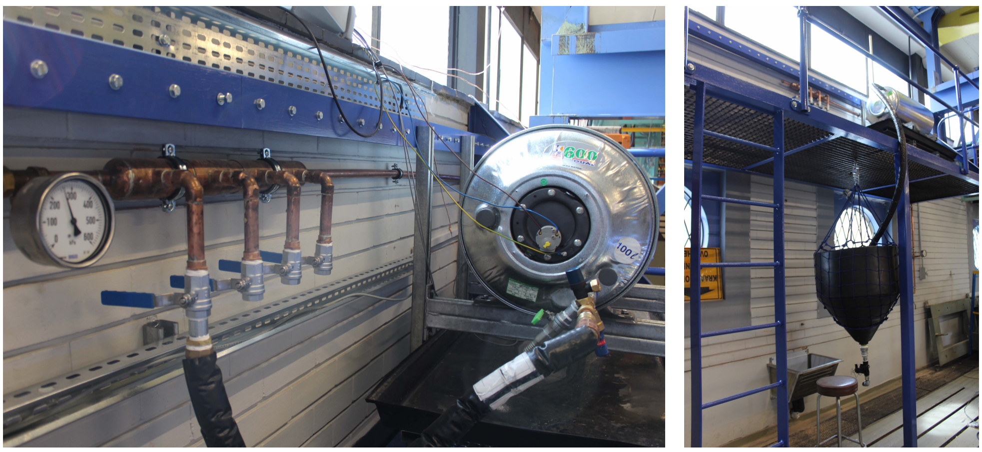

(a) Horizontal EWH cylinder on testing platform. (b) EWH and load.

Figure A.2: Photographs of the EWH testing platform at Wits.

A.1.2 EWH under Test

The EWH under test is an entry-level 150 ℓ, 3 kW EWH that is dual mountable, as shown in *Figure A.4*. The dimensions of the tank are shown in *Figure A.4*. The outer dimensions, outer length L_O and outer diameter D_O, can be measured or checked against the datasheet. Some specifications are also provided on the datasheet, such as the steel thickness, d_{steel} and the insulation thickness, $d_{insulation}$. Since the cylinder is mostly sealed, it is difficult to determine the inner length, z

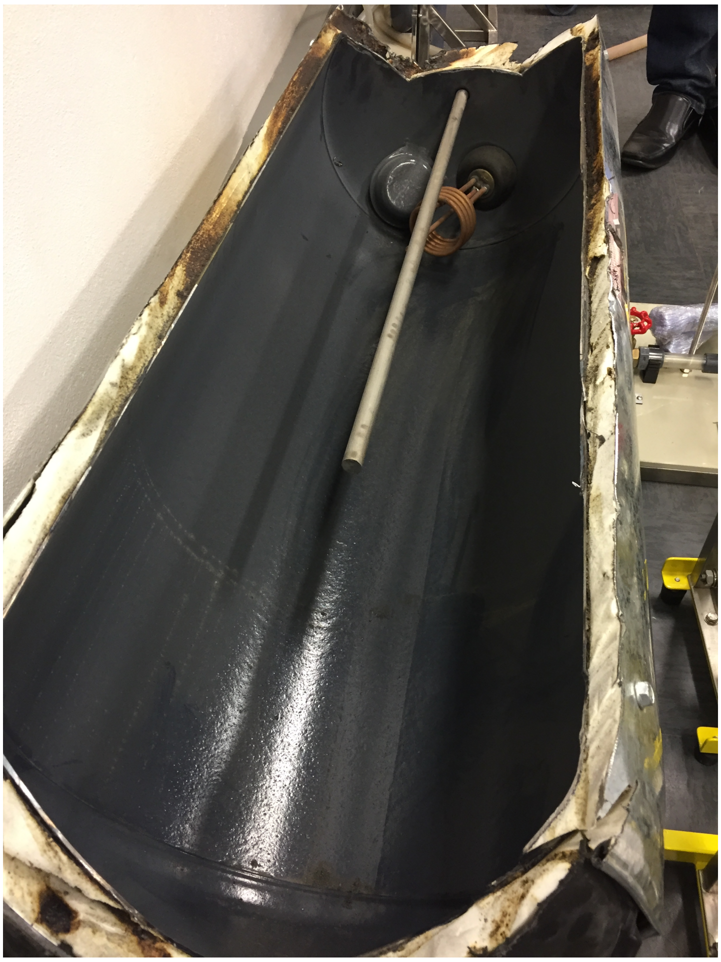

Figure A.3: Photograph of inner components in the EWH under test.

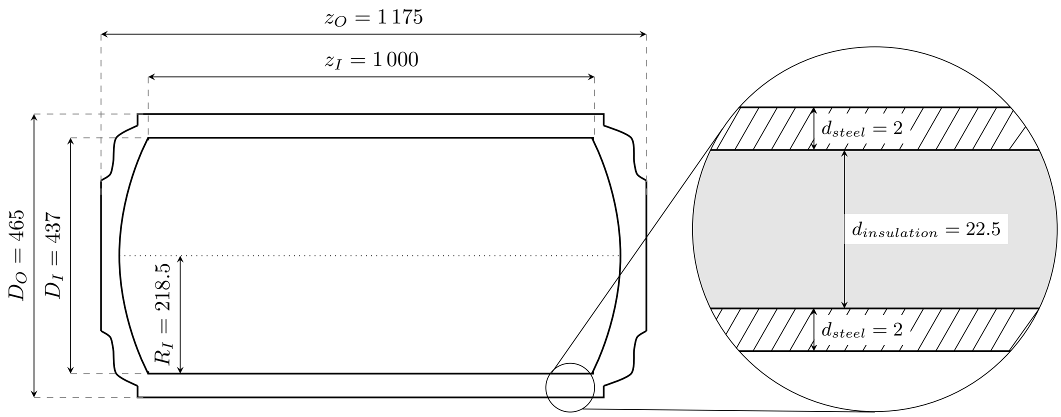

Figure A.4: Schematic of 150 ℓ, 3 kW EWH tank under test (all units in mm).

and inner diameter, D_I. These two parameters are therefore calculated. The inner diameter can be determined by *Equation A.1*, as there are two sets of steel and insulation covering the inner tank cylinder, and the inner tank cylinder needs to be accounted for too.

$$D_I = D_O - 2(d_{insulation}) - 4(d_{steel}) \tag{A.1}$$

The inner length is determined by assuming the cylindrical tank is ideally cylindrical, so the curved dome parts on either end of the circular face, which is evident in the actual device for handling high pressures, but are assumed to be flat for this analysis. Therefore, the volume of the tank can be used to calculate the inner tank length using *Equation A.2*. In the equation, the rated volume $150\,\ell$ is converted to mm^2 by a factor of 10^6, and is divided by the area of the inner circular face.

$$z_I = \frac{150 \times 10^6}{\pi \left(\frac{D_I}{2}\right)^2} \tag{A.2}$$

These inner dimensions, D_I and L_I, are required for the modelling process, where the tank is divided into separate segments and the volumes and surface areas are taken into account.

A.2 Temperature Calibration

The temperature sensor used is the Platinum Resistance Thermometer (PRT) PT100 (Class A) with a range of $-50°\text{C}-500°\text{C}$. A PT100 changes the measured resistance over its terminals with a change in observed temperature. It has a fundamental interval of $0°\text{C}-100°\text{C}$ with a nominal resistance of $38.5\,\Omega$. This results in a gradient or conversion factor, α, of 0.385 for the linear range, as shown in *Equation A.3*, where R_{PT100} is the resistance measured from the sensor (Ω) and T is the inferred temperature (°C).

$$R_{PT100} = \alpha T + 100 \tag{A.3}$$

The PT100 sensors were encased in thin steel casings. Using a temperature calibrator, an α value of 0.389 is obtained. Both the α values will be tested against a mercury thermometer under three different test scenarios.

A.2.1 Test 1: Container of Water at Room Temperature

Two PT100 sensors were tested against a mercury thermometer; all three sensors were placed in a container of well-mixed water at room temperature. The temperatures for the PT100 sensors were calculated using *Equation A.3*. The temperatures resulting from the two α values are shown in *Table A.1*.

Table A.1: Test 1: Temperature calibration of PT100s.

Sensor	**Measured Value**	**Temp (°C)** $\alpha = 0.385$	**Temp (°C)** $\alpha = 0.389$
Mercury Thermometer	20.5°C	–	–
PT100 Sensor 1	108.31 Ω	21.58	21.36
PT100 Sensor 2	108.48 Ω	22.03	21.80

It can be seen that the mercury thermometer reads a much lower temperature than the PT100s (approximately $1.3 - 1.5$). Temperatures predicted using $\alpha = 0.385$ are much higher than the thermometer. Temperatures predicted using $\alpha = 0.389$ higher than the thermometer, but lower than its counterpart.

A.2.2 Test 2: Aluminium Strip in Water (Cold and Hot)

A PT100 is tested with the mercury thermometer in a container of well-mixed water. The two sensors are connected thermally through an aluminium strip to try ensure both sensors read the same temperature. The resulting temperature predictions from both α values are presented in *Table A.2*.

Table A.2: Test 2: Temperature calibration of PT100s.

Sensor	**Measured Value**	**Temp (°C)** $\alpha = 0.385$	**Temp (°C)** $\alpha = 0.389$
Mercury Thermometer	27.0°C	–	–
PT100 Sensor 3	111.5 Ω	29.87	29.56
Mercury Thermometer	77.5 – 78°C	–	–
PT100 Sensor 3	130.3 Ω	78.70	77.89

For the cold water scenario at room temperature, the mercury thermometer reads a value approximately $2.5 - 3°C$ below the PT100s. This difference is approximately $1°C$ greater than values are seen in Test 1. For the hot water scenario, water is boiled and placed in the container and mixed well. The value from the mercury thermometer matches well with the temperature value produced by $\alpha = 0.389$.

A.2.3 Test 3: Steel Bar in Water (Cold and Hot)

A PT100 is tested with the mercury thermometer in a container of well-mixed water. The two sensors are connected thermally through a steel bar to try ensure both sensors read the same temperature. The resulting temperature predictions from both α values are presented in *Table A.3*.

Table A.3: Test 3: Temperature calibration of PT100s.

Sensor	**Measured Value**	**Temp (°C)** $\alpha = 0.385$	**Temp (°C)** $\alpha = 0.389$
Mercury Thermometer	26.5°C	–	–
PT100 Sensor 3	110.85 Ω	28.18	27.89
Mercury Thermometer	72.0°C	–	–
PT100 Sensor 3	128.5 Ω	74.02	73.26

For the cold water scenario at room temperature, the mercury thermometer reads a value approximately $1.5 - 2°C$ below the PT100s. Similar values are seen in Test 1. For the hot water scenario, water is boiled and placed in the container and mixed well. The value from the mercury thermometer reads a values approximately $1.3 - 1.5$ below the PT100s.

A.2.4 Conclusion

The temperature values produced by the PT100s are over $1°C$ above the mercury thermometer. The conversion factor that presents the better temperature values is $\alpha = 0.389$, as (i) it is produced by a temperature calibrator and (ii) it presents closer values to the mercury thermometer. The standard value of $\alpha = 0.385$ is therefore not used. It is possible that the steel casing for the PT100s contributes to this difference in conversion factor.

Appendix B

Additional Background Theory

This appendix presents additional background theory that is relevant to this work. *Section B.1* presents the theory required for calculation of hot water consumption. *Section B.2* presents stratification effects of layer geometry, exploring the difference between constant height and constant volume.

B.1 Hot Water Consumption

Domestic hot water consumption is usually associated to activities such as bathing, showering, hand wash, face wash and dish washing in a basin. Some countries use a centralised source for hot water services, such as kitchen, bathing or ablution use, and include a link to space heating and appliances use for dish washers and laundry use. But South African appliances for dish washing and clothes washing are connected to electrical mains with a built-in element and therefore do not link directly a centralised hot water source. A small portion of multi-family apartment buildings have centralised water heating systems.

ASHRAE (2003) cites representative temperatures for each of these hot water consumption activities, i.e. baths and showers at 43°C. Storing water at temperatures that are safe for consumer use presents a risk for diseases, most notably, Legionnaires' Disease, which is reported to colonise in water temperatures up to 46°C. Therefore, ASHRAE recommends the storage of hot water in the range of 60°C to minimise the risk of contamination. Therefore, tap-mixers, which combine hot water from the storage with a cold water line (around ambient temperature) at the point of dispensation, are required to ensure the safe use of hot water.

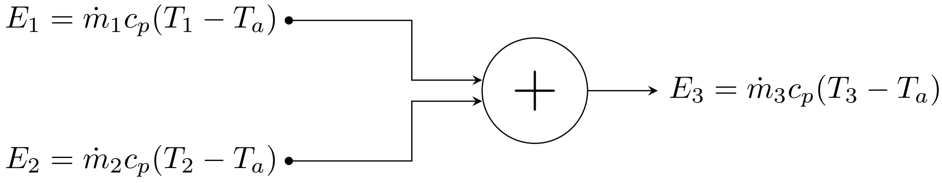

Figure B.1: Energy from two branches mixing and converging to one.

The mixing of converging mass flows in pipes from different temperature sources is shown in *Figure B.1*, where E_1 and E_2 is the energy flow in two separate pipes, for instance, hot and cold water pipes. These energy flows mix to produce E_3, which could be considered the consumer end. *Theorem 1* provides the derivation of the mixing of energy fed from two separate pipes due to mass flow depicted by *Figure B.1*

Theorem 1: Heat flow due to a mixer. By Conservation of Energy:

$$E_3 = E_1 + E_2$$

We know that:

$$E = \dot{m} c_p(T - T_a)$$

Therefore:

$$\dot{m}_3 c_p(T_3 - T_a) = \dot{m}_1 c_p(T_1 - T_a) + \dot{m}_2 c_p(T_2 - T_a)$$

$$\dot{m}_3(T_3 - T_a) = \dot{m}_1(T_1 - T_a) + \dot{m}_2(T_2 - T_a)$$

$$\dot{m}_3 T_3 - \dot{m}_3 T_a = \dot{m}_1 T_1 - \dot{m}_1 T_a + \dot{m}_2 T_2 - \dot{m}_2 T_a$$

By Conservation of Mass, we know that:

$$\dot{m}_3 = \dot{m}_1 + \dot{m}_2$$

Therefore

$$(\dot{m}_1 + \dot{m}_2)T_3 - (\dot{m}_1 + \dot{m}_2)T_a = \dot{m}_1 T_1 + \dot{m}_2 T_2 - (\dot{m}_1 + \dot{m}_2)T_a$$

$$(\dot{m}_1 + \dot{m}_2)T_3 = \dot{m}_1 T_1 + \dot{m}_2 T_2$$

$$\dot{m}_3 T_3 = \dot{m}_1 T_1 + \dot{m}_2 T_2$$

Since $\dot{m} = q\rho$ and ρ is constant:

$$q_3 T_3 = q_1 T_1 + q_2 T_2$$

$\square$

The total volume drawn, V, in each branch can be determined by multiplying the flow rate, q, of the branch by the total time of the draw event, t_d.

$$\begin{aligned} V_1 &= q_1\, t_d \\ V_2 &= q_2\, t_d \\ V_3 &= q_3\, t_d \end{aligned} \tag{B.1}$$

Two end-user scenarios are considered: a shower using a low-flow showerhead (in *Section B.1.1*), and a bath where only the hot water tap is opened (in *Section B.1.2*). For simplication of calculations, the following is considered:

- Hot water temperature is constant at 70°C,
- Cold water temperature is constant at 20°C,
- All flow rates are constant.

B.1.1 Scenario: Average Showerhead

An average showerhead has an approximate flow rate of 16 l/min and the temperature at the user-end should be 43°C to ensure user comfort. Therefore, we can equate $q_3 = 16\,\mathrm{l/min}$ and $T_3 = 43$°C. The temperatures from each branch are $T_1 = 70$°C for the hot water pipe and $T_2 = 20$°C for the cold water pipe. By using the resulting equation in *Theorem 1* and the Conservation of Mass, the remaining two unknown parameters can be determined as $q_1 = 7.4\,\mathrm{l/min}$ and $q_2 = 8.6\,\mathrm{l/min}$. For simplicity and the fact that flow rates are difficult to control at decimal accuracy, these flow rates will be approximated to 8 l/min.

It is estimated that the average shower has a duration of 8 min (7.19 min for Willis et al. (2010)). By using *Equation B.1* for the hot water line, with an estimated flow rate of $q = 8\,\mathrm{l/min}$ and shower duration of $t_d = 7\,\mathrm{min}$, the total volume drawn from the EWH is approximately $V = 50\,\mathrm{l}$. This is comparative to the low flow shower or bath value of 57 l presented by ASHRAE (2003). By considering a shower duration of double the time $t_d = 14\,\mathrm{min}$, the total drawn volume of $V = 100\,\mathrm{l}$. A volume of 50 l and 100 l represents 33.3% and 66.6% of 150 l capacity tank.

B.1.2 Scenario: Hot Bath

A hot water tap fully open scenario is considered, which could account for a bath, where only the hot water tap runs for a period of time. The maximum flow rate of the test system is 30 l/min, so this is the flow rate tested. Depending on the pressure of the pipes fed by municipality, this flow rate could vary. For comparative measures, the draw volumes from the show scenario will be used: 50 l and 100 l. A 50 l draw would partially fill tub with 80 l capacity and allow for some cold water mixing. A 100 l draw would overfill the tank, but is included as a test scenario for completeness.

B.2 Stratification Effects on Cylinder Geometry

In the dynamic state while energy is being drawn from the tank, cold water replaces the drawn volume which causes thermal stratification layers within the tank. These layers also remain in the tank if a partial draw event occurs (some percentage smaller than 100%) and diffusion of heat occurs, whereby layers interact with each other through the connecting surface areas, and diffusion also occurs through the casing of the vessel, in this case, mild steel.

Therefore, the geometry of a storage cylinder has a major impact on the stratification of thermal layers and therefore its thermal storage capabilities. The gravitational direction on a cylinder determines how thermal layers sit in the tank. For a vertically mounted cylinder, the effective area of each thermal layer is circular and remains constant along the height of the tank, h_V. For a horizontally mounted cylinder, the effective area of each thermal layer is rectangular and changes along the height of the tank, h_H.

B.2.1 Vertical - Constant Height

Figure B.2 shows the differences between thermal layering in the horizontal and vertical orientations from a two-dimensional viewpoint. The third dimension in the y-direction is considered constant in each case. This illustrates the difference in volume between both geometries with a constant change in height, denoted dh, along the height of the tank.

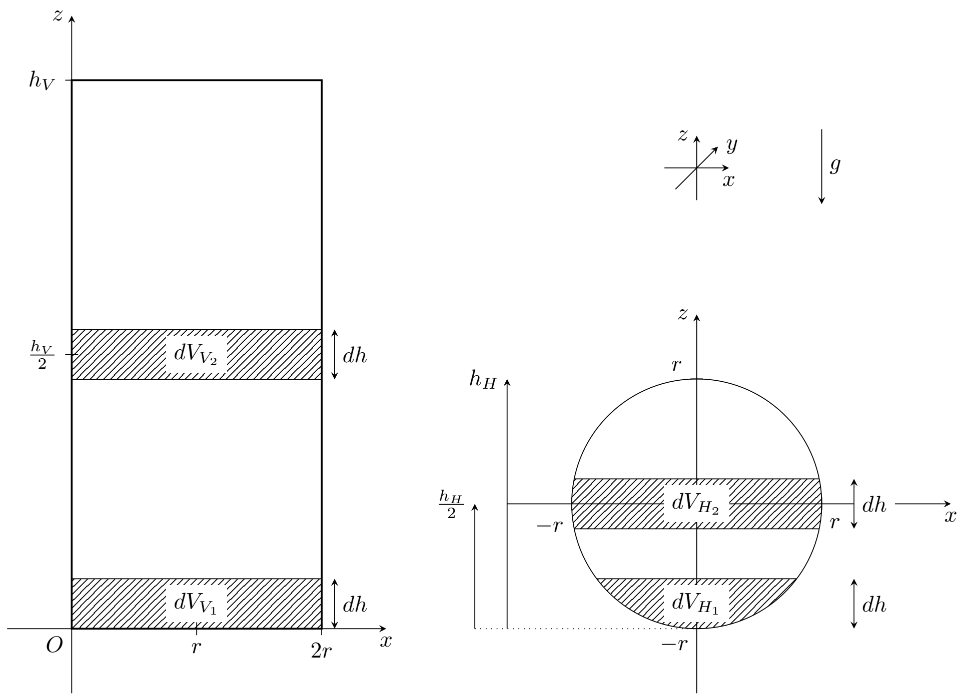

Figure B.2: Change in water volume based on fixed change in height, dh. Orientations: vertical (left) and horizontal (right).

Equation B.2 determines the total volume of water in the vertical orientation, starting from the bottom of the tank where $z = 0$:

$$dV_V = \int_0^{h_V} \pi r^2 \; dz \tag{B.2}$$

For partial volume calculation in the vertical orientation for a change in height, dh, as shown by dV_{V_1} in *Equation* B.3. Since the volume slices for dV_{V_1} and dV_{V_2} is constant in the x-direction, the change in volume is also constant along the height of the tank in the z-direction, therefore $dV_{V_1} = dV_{V_2}$.:

$$dV_{V_1} = \int_0^{h} \pi r^2 \; dz \quad = \quad \int_{\frac{h_V}{2}-\frac{h}{2}}^{\frac{h_V}{2}+\frac{h}{2}} \pi r^2 \; dz = dV_{V_2} \tag{B.3}$$

B.2.2 Horizontal - Constant Height

Equation B.4 determines the total volume of water in the horizontal orientation, starting from the bottom of the tank where $z = -r$, the top of the tank is $z = r$ and L denotes the length of the tank:

$$dV_H = \int_{-r}^{r} 2L\sqrt{r^2 - z^2} \; dz \tag{B.4}$$

Thermal layers in the horizontal orientation are not uniform over the height of the tank as indicated by the z-axis. If comparing volumes with the same change in height, denoted by dh, $dV_{H_1} < dV_{H_2}$, since:

$$\int_{-r}^{-r+h} 2L\sqrt{r^2 - z^2}\ dz \quad < \quad \int_{-\frac{h}{2}}^{\frac{h}{2}} 2L\sqrt{r^2 - z^2}dz \tag{B.5}$$

Inversely, if the volumes dV_{V_1}, dV_{V_2}, dV_{H_1} and dV_{H_2} are considered equal, then $dh|_{V_1} = dh|_{V_2}$ and $dh|_{H_1} > dh|_{H_2}$. This mode of comparison will be more useful when comparing stratification of thermal layers between the two tank orientations.

B.2.3 Area of a Circle - Segmentation in z-Direction

This section shows the derivation for the area of a circle integrating in the z-direction. To represent a circle in a x-z Cartesian plane as shown in *Figure B.2*, the following expression is used, where r is a constant:

$$\begin{aligned} x^2 + z^2 &= r^2 \\ x &= \pm\sqrt{r^2 - z^2} \\ &= \pm r\sqrt{1 - \frac{z^2}{r^2}} \end{aligned} \tag{B.6}$$

Due to symmetry, the area of a semi-circle can be solved where $x > 0$ is half the total area.

$$x = r\sqrt{1 - \frac{z^2}{r^2}} \tag{B.7}$$

Symmetry can also apply to the case of $z > 0$, where only the top right quarter is considered. The area of one quadrant of the circle is equivalent to a quarter of the total area. Integrate over z from 0 to a to get the total area of the quadrant.

$$\frac{1}{4}A = \int_0^a r\sqrt{1 - \frac{z^2}{r^2}}\ dz \tag{B.8}$$

Let $sint = \frac{z}{r}$ where $dz = r\,cos\theta\ d\theta$. Limits $z = 0$ transforms to $\theta = 0$ and $z = a$ becomes $\theta = \frac{\pi}{2}$.

$$\begin{aligned} \frac{1}{4}A &= \int_0^{\frac{\pi}{2}} r\sqrt{1 - sin^2\theta}\ r\,cos\theta\ d\theta \\ &= \int_0^{\frac{\pi}{2}} r^2\,cos\theta\sqrt{1 - sin^2\theta}\ d\theta \end{aligned} \tag{B.9}$$

Using the trigonometric identity $\sqrt{1 - sin^2\theta} = cos\theta$, since θ varies from 0 to $\frac{\pi}{2}$:

$$\frac{1}{4}\,A = \int_0^{\frac{\pi}{2}} r^2\,cos^2\theta\;d\theta \tag{B.10}$$

Use trigonometric identity $cos^2\theta = \frac{cos2\theta+1}{2}$ to linearize the integrand.

$$\frac{1}{4}\,A = \int_0^{\frac{\pi}{2}} r^2\,\frac{cos2\theta + 1}{2}\;d\theta \tag{B.11}$$

Evaluate the integral to determine the area of a quadrant and solve for area of the circle:

$$\begin{aligned}\frac{1}{4}\,A &= \frac{1}{2}\,r^2\left[\frac{1}{2}\,sin2\theta + \theta\right]_0^{\frac{\pi}{2}} \\ A &= \frac{4}{2}\,r^2\left[\frac{1}{2}\,sin2\frac{\pi}{2} + \frac{\pi}{2} - \frac{1}{2}\,sin2(0) - 0\right] \\ &= 2\,r^2\left(\frac{\pi}{2}\right) \\ A &= \pi\,r^2\end{aligned} \tag{B.12}$$

To generalise the expression for partial areas of the circle segmented in the z-direction, tranformed into the θ-direction, $\frac{\partial A}{\partial \theta}$, the following expression is used:

$$A = 2\,r^2\left[\frac{1}{2}\,sin2\theta + \theta\right]_{\theta_1}^{\theta_2} \qquad \theta_1, \theta_2 = \left[-\frac{\pi}{2} : \frac{\pi}{2}\right] \tag{B.13}$$

B.2.4 Horizontal - Constant Volume

$$V_j = A_j \times L \tag{B.14}$$

Constant volume segmentation for a tank in the horizontal orientation would require determining a constant area of a circle and multiplying by length L of the tank, as shown in *Equation B.14*. The area of a circle is obtained by solving of *Equation B.13* between different values of θ. In the example shown in *Figure B.3*, the area of the circle has been divided into 8 equal segments. *Figure B.3 (a)* shows the area of a semi-circle of θ in the range [0:$\pm\frac{\pi}{2}$]; by symmetry the positive and negative values of θ produce the same area.

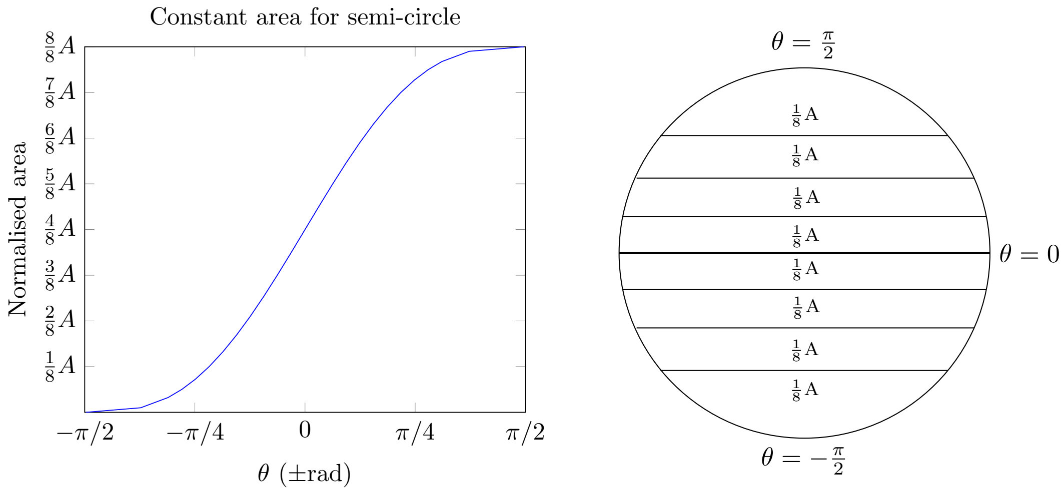

(a) (b)

Figure B.3: Constant area segmentation for a circle (a) Normalised area for semi-circle [0:$\frac{\pi}{2}$] or [0:-$\frac{\pi}{2}$] (b) Segmentation in 8 equal layers.

Table B.1: Residential tariff structures for City Power in 2019/2020 (City Power, 2020).

Parameter	**Summer (c/kWh)**	**Winter (c/kWh)**
Prepaid (0 – 350)	139.42	139.42
Prepaid (351 – 500)	159.92	159.92
Prepaid (> 500)	182.23	182.23
Metered (0 – 350)	134.08	134.08
Metered (501 – 1 000)	153.87	153.87
ToU Peak	162.57	374.01
ToU Standard	128.60	153.21
ToU Off-peak	101.17	108.11

B.2.5 Deferrable Loads and ToU

For the context of responsive loads on the grid, the ToU tariff presents an opportunity for smart-metered residential consumers to save in electricity costs by participating with deferrable loads. *Table B.1* presents the residential tariff structures for prepaid and metered households in comparison to the ToU tariffs. Notable is the peak winter tariff (374.01 c/kWh) is over double the average user rate in the range of 160 c/kWh. A 50 ℓ shower with a primary heat replacement duration of 1-hour, with the correct intelligent controls to defer a load to off peak tariff could save the end-user roughly 74 c per shower, or R135/season, where the season is considered for winter. A poorly timed shower without intelligent controls to defer the load would result in an additional 214 c per shower, or R390/season.

The ToU structure as presented severely decentivises usage during peak times in winter. Implementation of the multi-node model in the aggregated system would provide insight on the effectiveness of these tariffs in conjunction with smart load capabilities.

Appendix C

Model Design Decisions

This appendix covers the some finer details with regard to design decisions for the model. The total number of layers is discussed in *Section C.1*. The calculation of layer parameter is discussed in more detail in *Section C.2*. And finally, the parameters effects are briefly discussed in *Section C.3*.

C.1 Total Number of Layers

The total number of layers chosen in the simulation is related to the number of equi-distant sensors in the tank. For this work, multiples of eight are used, as eight temperature sensors were used (to produce initial layer temperatures for the simulations). The effect of total layer numbers will be discussed in this section; the following layouts are considered:

- 8 (8×1) layers,
- 16 (8×2) layers,
- 24 (8×3) layers and
- 32 (8×4) layers (not in this section, but presented in document body).

The layer layouts are based on a fixed height of a layer. The 8-layer and 16-layer structures are shown in *Figure C.1*, which include the element layers and thermostat layers used. The 24-layer and 32-layer structures were omitted due to the large number of layers represented, however, the 16-layer structure provides the base

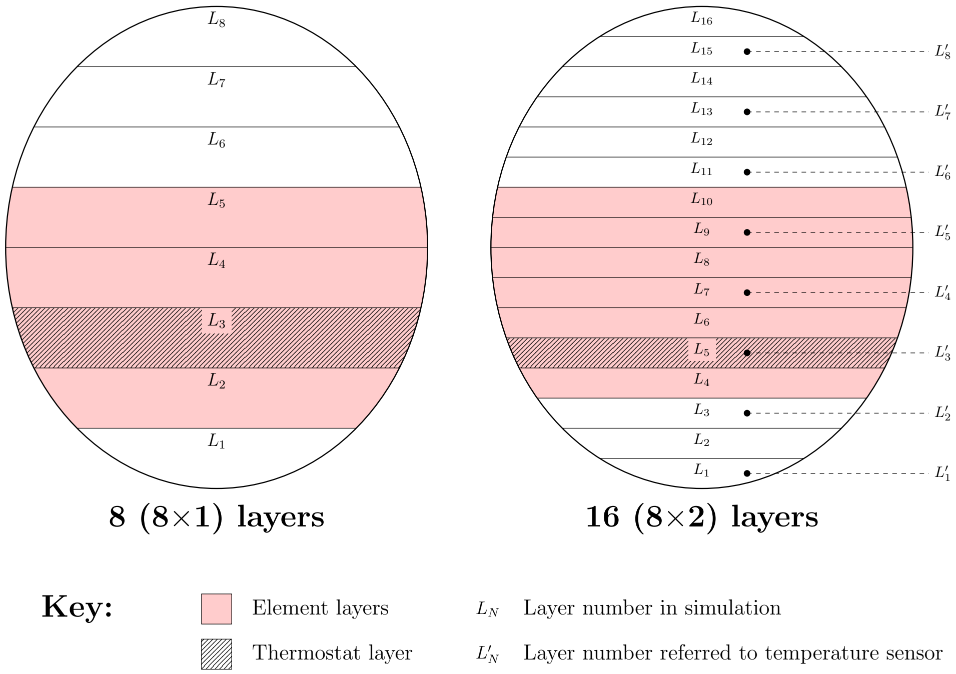

Figure C.1: Examples of total number of layers for simulations 8 layers (left) and 16 layers (right), which include element layers and thermostat layers.

comparison for the structures. The layers used in the simulations are denoted L_N and the referred layer number matching the temperature sensor location is denoted L'_N. The referred layer $L_{N'}$ is the temperature reported in the simulation outputs for comparison to measured data.

The 8-layer layout means that each measured temperature sensor matches to a corresponding simulated layer, therefore $L'_N = L_N$. The referred layer, L'_N, is the temperature reported in the simulation ouputs. The element layers are L_2 to L_5, corresponding to heights 0.163875m to 0.32775m in the tank (where layer height is 0.054625m) and the thermostat layer is L_3, (see schematic in *Figure C.1*). The thermostat layer corresponds to a fixed height in the tank.

The 16-layer layout means that for every temperature sensor, an extra layer has been formed and an initial temperature is interpolated (discussed in more detail in *Section C.2.2*). The referred layer reported is $L'_N = L_{2N-1}$. The element layers are L_4 to L_{10} and the thermostat layer is L_5, (see schematic in *Figure C.1*). The thermostat layer corresponds to a fixed height in the tank.

The 24-layer layout means that for every temperature sensor, an extra three layers are formed with initial temperatures interpolated. The referred layer reported is $L'_N = L_{3N-2}$. The element layers are L_5 to L_{13} and the thermostat layer is L_7.

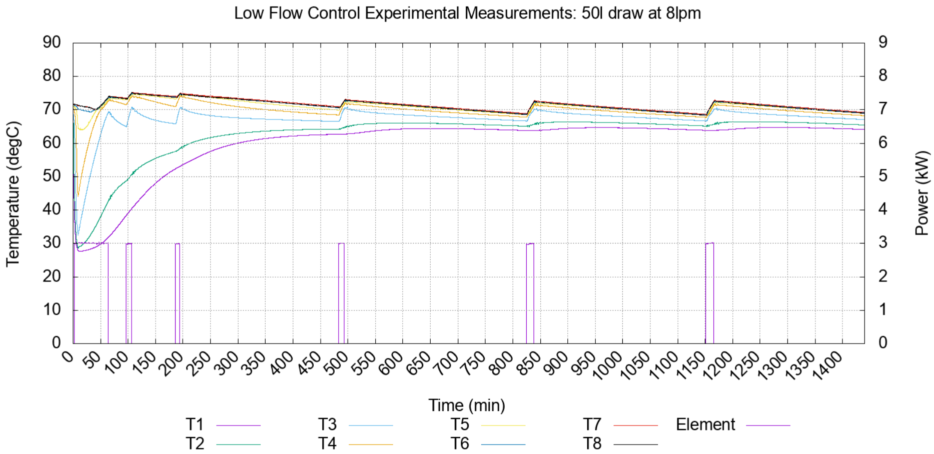

Figure C.2: Measured temperature and element trends for 50l low flow sample 1 (control test).

Element layers for the 24-layer simulation needed to be adjusted to resolve the extra subsequent replacement event. If element layers were not adjusted, the output was identical to the 16-layer simulation. The thermostat layer corresponds to a fixed height in the tank.

The low flow 50 l draw scenario is chosen as the first example used for discussion in *Section C.1.1*. The second scenario chosen is the low flow 100 l draw scenario in *Section C.1.2*, where the flow rate is kept relatively constant and the volume drawn is different.

C.1.1 Simulation Layers: Low Flow 50l Draw Scenario (Control)

The control scenario (presented in *Section 6.2.1*) is used as one of two examples for discussing the choice of total number of layers used in the simulation. The measured temperature and element data is presented in *Figure C.2*. Measured temperatures denoted by T_N are simulated by L'_N. The primary replacement duration is 62.22 min, with two subsequent replacement events occuring at around 100 min and under 200 min. Steady-state events start occuring from around 500 min.

The comparison of simulation outputs based on the total number of layers used are shown in *Figure C.3*. The simulation parameters are fixed to those presented in *Table 5.2*.

The 8-layer simulation, presented in *Figure C.3 (a)*, shows a single primary element

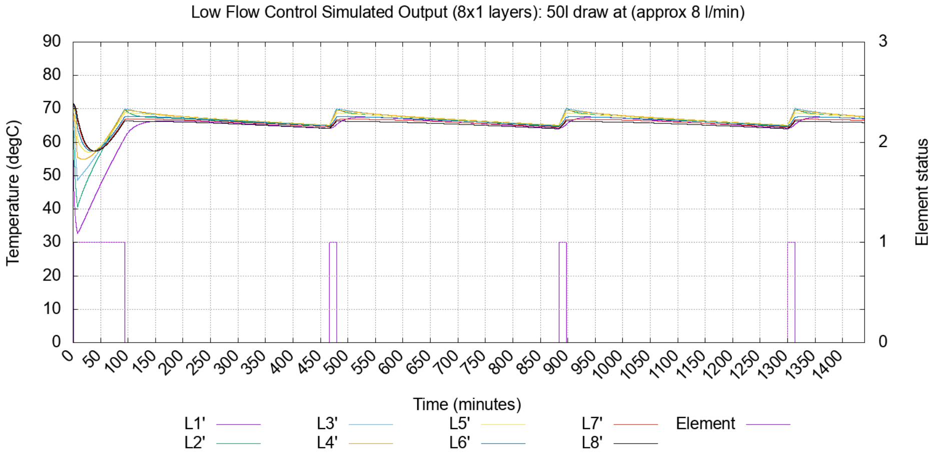

(a) Total of 8 layers (8 × 1).

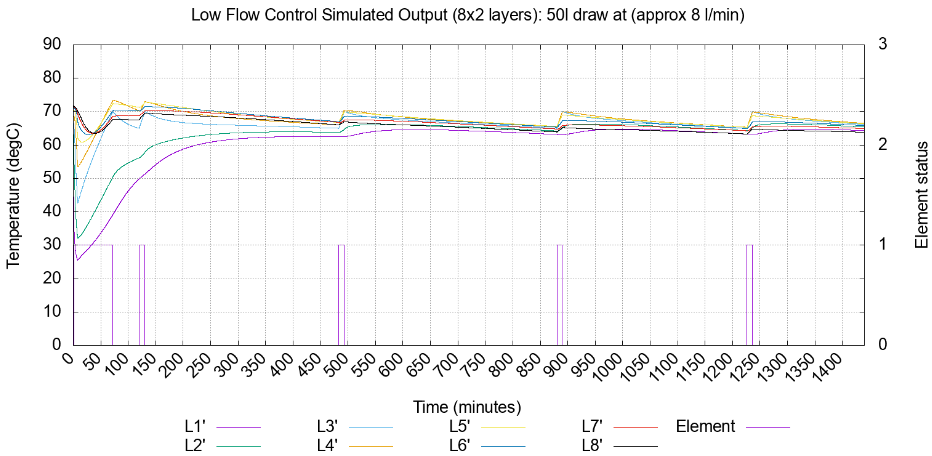

(b) Total of 16 layers (8 × 2).

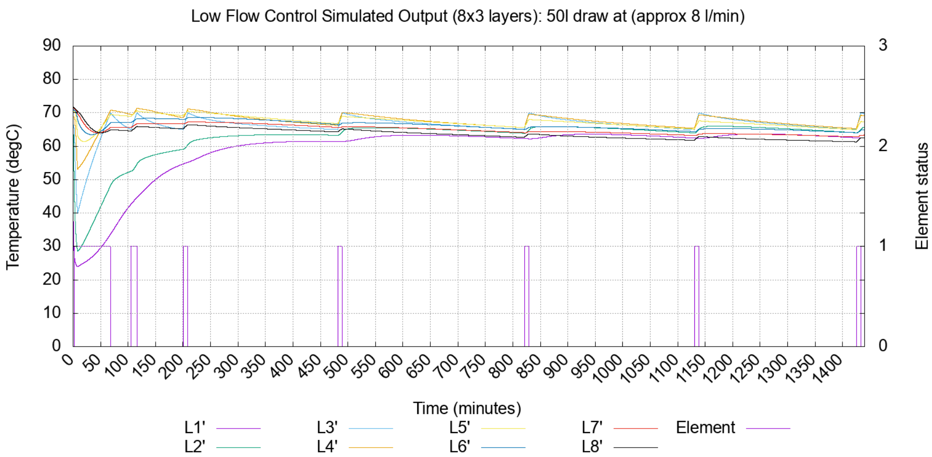

(c) Total of 24 layers (8 × 3).

Figure C.3: Simulated model for 50 l low flow sample 1 using 8, 16 and 24 layers.

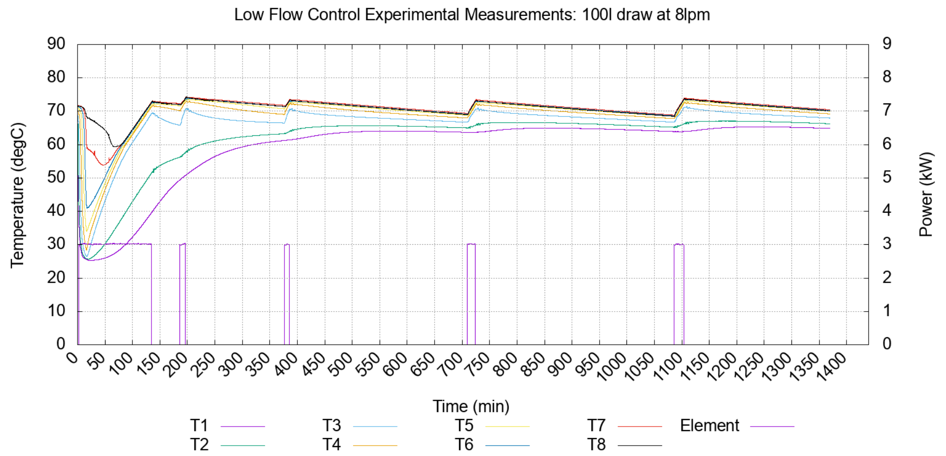

Figure C.4: Measured temperature and element trends for 100l low flow sample 1.

replacement with a large duration (almost 100 min), no subsequent element events and three steady-state events starting around 500 min.

The 16-layer simulation, presented in *Figure C.3 (b)*, shows the primary element replacement with a duration of approximately 60 min, one subsequent element event occurring around 120 min and three steady-state events starting around 500 min.

The 24-layer simulation, presented in *Figure C.3 (c)*, shows the primary element replacement with a duration of approximately 60 min, two subsequent element events occurring around 100 min and 200 min and three steady-state events starting around 500 min.

C.1.2 Simulation Layers: Low Flow 100l Draw Scenario (Control)

The low flow 100 l draw scenario (presented in *Section 6.2.3*) is used as the second of two examples for discussing the choice of total number of layers used in the simulation. The measured temperature and element data is presented in *Figure C.4*. Measured temperatures denoted by T_N are simulated by L'_N. The primary replacement duration is 132.95 min, with two subsequent replacement events occuring at around 200 min and under 400 min. Steady-state events start occuring from around 700 min.

The comparison of simulation outputs based on the total number of layers used are shown in *Figure C.5*. The simulation parameters are fixed to those presented in *Table 5.2*.

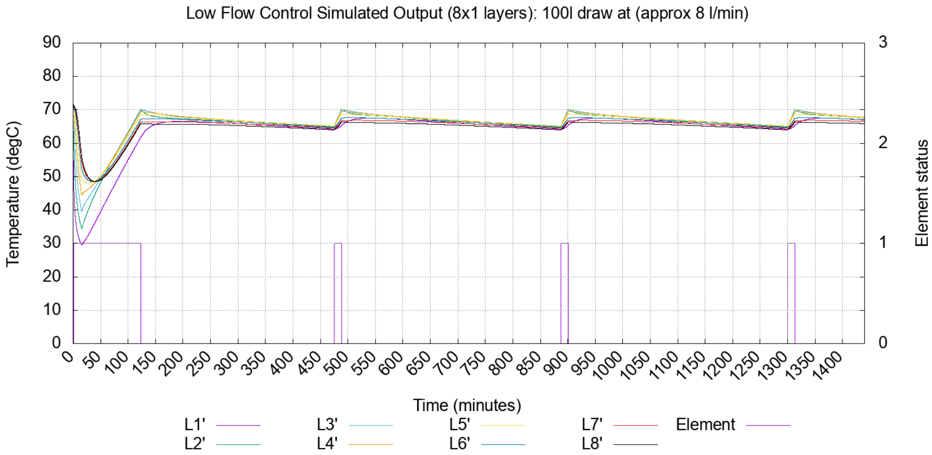

(a) Total of 8 layers (8 × 1).

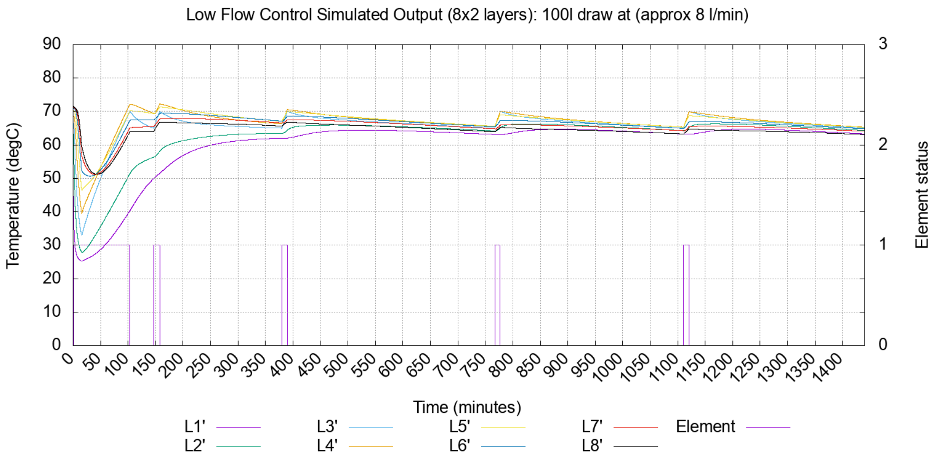

(b) Total of 16 layers (8 × 2).

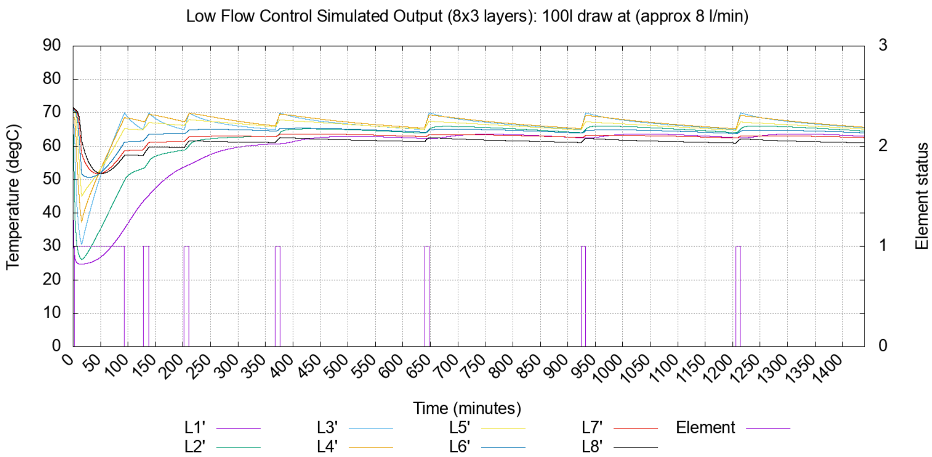

(c) Total of 24 layers (8 × 3).

Figure C.5: Simulated model for 100 l low flow sample 1 using 8, 16 and 24 layers.

The 8-layer simulation, presented in *Figure C.5 (a)*, shows a single primary element replacement with a large duration (around 125 min), no subsequent element events and three steady-state events starting around 500 min.

The 16-layer simulation, presented in *Figure C.5 (b)*, shows the primary element replacement with a duration of approximately 100 min, two subsequent element events occurring around 150 min and 400 min and two steady-state events starting around 800 min. This ouput actually matches the measured outputs quite well.

The 24-layer simulation, presented in *Figure C.5 (c)*, shows the primary element replacement with a duration just below 100 min, three subsequent element events occurring around 130 min, 200 min and 370 min and three steady-state events starting around 650 min.

C.1.3 Discussion

As discussed in *Section 3.2.2*, T_1 and T_2 (or L'_1 and L'_2) remain at lower temperatures during all states of the EWH. Therefore, the simulation results would need to present such patterns in the temperatures produced. The subsequent element replacement events are caused by the fact that L'_1 and L'_2 heat up much slower than the other layers.

The use of the 8-layer simulation structure does not allow for subsequent element events to occur since layer L'_2 is an element layer, and therefore it heats up as quickly as the element supplies power to it. Therefore, this does not allow for the bottom two sensor layers L'_1 and L'_2 to heat up more gradually to produce the subsequent element events (as shown in *Figure C.2*).

By increasing the total number of layers to 16 layers, $L1'$ and L'_2 show better signs of heating up slowly. However, for the 50 l draw test, this only results in one subsequent event, where two subsequent events are required for a match. This works conversely for the 100 l draw test where two subsequent events produced by the simulation results in a good match in output. This output matches better than the 24-layer and 32-layer (discussed in *Section 6.2.3*). However, since the same set of parameters was used and trained using the control scenario, this result is known to be possible, but not within the controlled parameters provided.

Increasing the total number of layers further to 24 layers, $L1'$ and L'_2 show better signs of heating up slowly and therefore allow for the appearance of addition subsequent replacement events. By increasing the number of total layers, the ability to heat specific layers becomes possible and allows for the finer control. The final 32 layers was chosen for this reason.

C.2 Calculation of Layer Parameters

The layer parameters are separated into the physical attributes (volume and boundary areas) and the starting temperatures. Each are treated quite differently. The physical attributes of the layer are determined geometrically; an example of an 8-layer calculation is presented in *Section C.2.1*. If the total number of layers is greater than the number of tank temperature sensors, then interpolation needs to occur, where temperatures in layers not matching to temperature sensors need to be determined. This is discussed in *Section C.2.2*.

C.2.1 Layer Volume and Boundary Areas

As an example, the steps taken to divide the tank into eight layers with equi-distant spacing, denoted L_1 to L_8 is presented to calculate each layer volume and boundary areas. These attributes can be determined geometrically. This set of steps can be expanded for any chosen number of total layers, as required.

By observing the tank in its circular cross-section, the tank can be divided into layers based on height, as shown in *Figure 5.3* in *Section 5.2*. The height of each layer is determined by dividing the total inner diameter D_I by 8, resulting in a layer height y of 54.6 mm, which corresponds well with the sensor height at 55 mm intervals.

For the first layer at height, y, a corresponding chord, x, which intersects the circle can be determined for the segment of the circle. This chord subtends subtends an angle of θ at the center of the circle. This is shown in the circle-face geometry in *Figure C.6*. By symmetry, the circle can by cut along the y-axis through its center point, where only one half of the circle is considered. Triangle OAB' therefore becomes a right-angled triangle, where angle from point O is $\frac{\theta}{2}$ and the hypothenuse is inner radius R_I. Length OB' can be obtained by deducting the layer height y from the radius R_I. Therefore, the *cosine* trigonometric relationship can be used to determine the angle θ, as shown in *Equation C.1*.

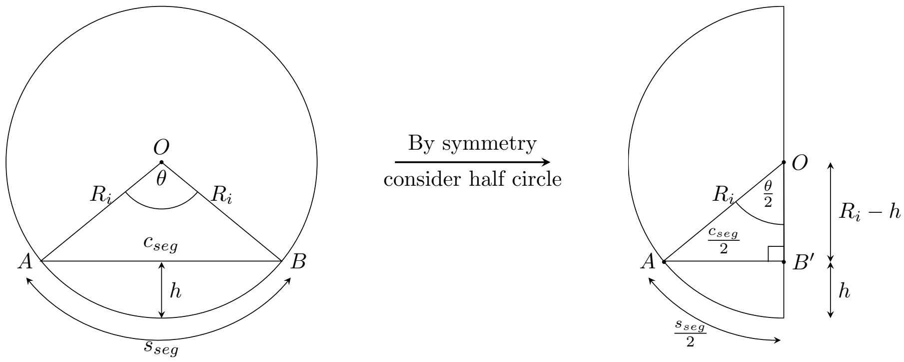

Figure C.6: Circle geometry to find angle θ from segment height y.

$$\begin{aligned} cos\left(\frac{\theta}{2}\right) &= \frac{R_I - h}{R_I} \\ \theta &= 2\,arccos\left(\frac{R_I - h}{R_I}\right) \end{aligned} \tag{C.1}$$

This relationship can be used for layers below the circle center O based on height y, $2y$, $3y$ and $4y$. For layers above circle centre O, it can be seen that by symmetry on the horizontal x-axis layer L_1 and L_8 are the same; similarly, L_2 and L_7, L_3 and L_6, and finally L_4 and L_5. Therefore, the only angles that are used are 83°, 120°, 151° and 180°. The trailing $-/+$ operator in *Table C.1* is used to indicate angles below the center point ($-$) and angles above the center point ($+$).

The area of the circle segment can be found using *Equation C.2*.

$$A_{seg} = \frac{R_I^2}{2}\left(\frac{\pi}{180}\,\theta - sin\theta\right) \tag{C.2}$$

For layers $L_2 - L_4$, the calculated areas are cummulative of layers below, so the areas of lower layers need to be deducted. Layers $L_5 - L_8$ can be determined by symmetry. An example of the cummulative nature of the segment areas is shown in *Equation C.3*.

$$\begin{aligned} A_1 &= \frac{R_I^2}{2}\left(\frac{\pi}{180}\,\theta_1 - sin\theta_1\right) \\ A_2 &= \frac{R_I^2}{2}\left(\frac{\pi}{180}\,\theta_2 - sin\theta_2\right) - A_1 \\ A_3 &= \frac{R_I^2}{2}\left(\frac{\pi}{180}\,\theta_3 - sin\theta_3\right) - A_2 - A_1 \end{aligned} \tag{C.3}$$

Table C.1: Details of volume layers for modeling purposes, where y is the layer height, θ is the angle from the circle center, A_{seg} is the area of the circle segment, V_{seg} is the associated volume, s_{seg} is the segment length and c_{seg} is the chord length.

Volume Layer	y (mm)	θ $(°)$	A_{seg} (mm^2)	V_{seg} (l)	s_{seg} (mm)	c_{seg} (mm)	**Chord Label**
L_1	54.6	83−	10,821	10.82	316	289	c_1
L_2	109.3	120−	18,502	18.50	142	378	c_2
L_3	163.9	151−	22,051	22.05	118	423	c_3
L_4	218.5	180−	23,620	23.62	110	437	c_4
L_5	273.1	180+	23,620	23.62	110	423	c_5
L_6	327.8	151+	22,051	22.05	118	378	c_6
L_7	382.4	120+	18,502	18.50	142	289	c_7
L_8	437.0	83+	10,821	10.82	316	−	−

The volume of each layer can be found by multiplying the area segment by the inner length of the tank L_i as shown in *Equation C.4*. The unit of this volume parameter is calculated as mm^3; this is converted to litres l by multiplying a factor of 10^{-6}.

$$V_{seg} = A_{seg}\, L_i \tag{C.4}$$

To obtain the surface areas of each layer, the segment length of the circle s_{seg} and the chord c_{seg} at each height need to be determined. The segment length s_{seg} can be determined as a function of θ and radius R_I by using *Equation C.5*. The angle θ is converted to radians to obtain a segment s_{seg} unit of mm.

$$s_{seg} = \frac{\pi}{180}\,\theta\, R_I \tag{C.5}$$

As with the segment area A_{seg}, the resulting segment length from *Equation C.5* is the cummulative length, so to obtain the lengths for $L_2 - L_4$ need to subtract lengths of the preceding layers. Segment lengths for $L_5 - L_8$ can be determined by symmetry. The segment lengths are multiplied by the inner length of the tank L_i to obtain a surface area, which will determine the heat-transfer losses to the outer insulation layers and the ambient temperature.

Table C.2: Surface area calculations for each segement s_{seg} and chord c_{seg} with corresponding layer association to each parameter for $N = 8$.

Ref	s_{seg} Label	Surface Area SA_s (m^2)	Affected Layers	c_{seg} Label	Surface Area SA_c (m^2)	Affected Layers
1	s_1	0.316	L_1	c_1	0.289	L_1, L_2
2	s_2	0.142	L_2	c_2	0.378	L_2, L_3
3	s_3	0.118	L_3	c_3	0.423	L_3, L_4
4	s_4	0.110	L_4	c_4	0.437	L_4, L_5
5	s_5	0.110	L_5	c_5	0.423	L_5, L_6
6	s_6	0.118	L_6	c_6	0.378	L_6, L_7
7	s_7	0.142	L_7	c_7	0.286	L_7, L_8
8	s_8	0.316	L_8	–	–	–

The chord c_{seg} at each height is determined from the the half-circle consideration in *Figure C.6*, where the angle from the centre point O is $\frac{\theta}{2}$, the length AB' is $\frac{c_{seg}}{2}$ and the hypothenuse is R_I. Therefore, the *sine* trigonometric relationship can be used as shown in *Equation C.6*.

$$\begin{aligned} \frac{c_{seg}}{2\,R_I} &= sin\left(\frac{\theta}{2}\right) \\ c_{seg} &= 2\,R_I\,sin\left(\frac{\theta}{2}\right) \end{aligned} \tag{C.6}$$

Note that there are only seven chords ($C_1 - C_7$), as they are the lengths between the layers. This length is multiplied by the inner length of the tank L_i to obtain a surface area. This will determine the inter-layer heat-transfer through this surface area.

The final calculated values for segment area A_{seg}, volume V_{seg}, segment length s_{seg} and chord length c_{seg} are provided in *Table C.1.* The resulting parameters for layer surface areas provided in *Table C.2* with corresponding layer associations. Surface areas are determined by multiplying segment and chord lengths with the inner length of the tank z, as shown in *Equation C.7* and *Equation C.8.*

$$SA_s = s_{seg}\,z \tag{C.7}$$

$$SA_c = c_{seg}\, z \tag{C.8}$$

C.2.2 Temperature Interpolation

Interpolation is the prediction of temperatures given a reference in space on two known boundary temperatures. The prediction process used makes the assumption that the temperatures are linearly distributed in space between two known temperatures. Therefore, a gradient can be determined between each sensor temperature which is already equally distributed in space and a relative temperature can be predicted for the in-between layer. For the sake of simplicity, the sensor label is used instead of the sensor height, although the use of height as a reference would be more appropriate.

An example of interpolated points for a set of measured temperatures is shown in *Figure C.7*. This shows the eight original sensor locations with labels 1 to 8, Sensor 1 is located at the bottom of the tank, and Sensor 8 located at the top, as indicated in *Figure 3.2*. This example uses 32 layers for the model, which produces an additional three layers per sensor that need initial temperature values. The x-axis labels under the graph refer to the sensor indices (1-8), and the x-axis labels above the graph refer to the simulation layers (0-32).

Temperature gradients (g) are determined using *Equation C.9*, where ΔT is the difference between two sequential sensors and $\Delta Sensor$ is the difference between two sensor indices and for this case, is always 1 (applies only for fixed sensor spacing).

$$g = \frac{\Delta T}{\Delta Sensor} \tag{C.9}$$

An example of the gradient between Sensor 1 and Sensor 2, denoted g_{12} is shown in *Equation C.10*, where T_1 and T_2 are the measured temperatures from Sensor 1 and Sensor 2 and $\Delta Sensor = 1$.

$$g_{12} = \frac{T_2 - T_1}{1} \tag{C.10}$$

A multiplication factor, f_m is determined to move from eight temperature sensors to 32 temperature layers. This is done by dividing the total number of layers N_{layers}

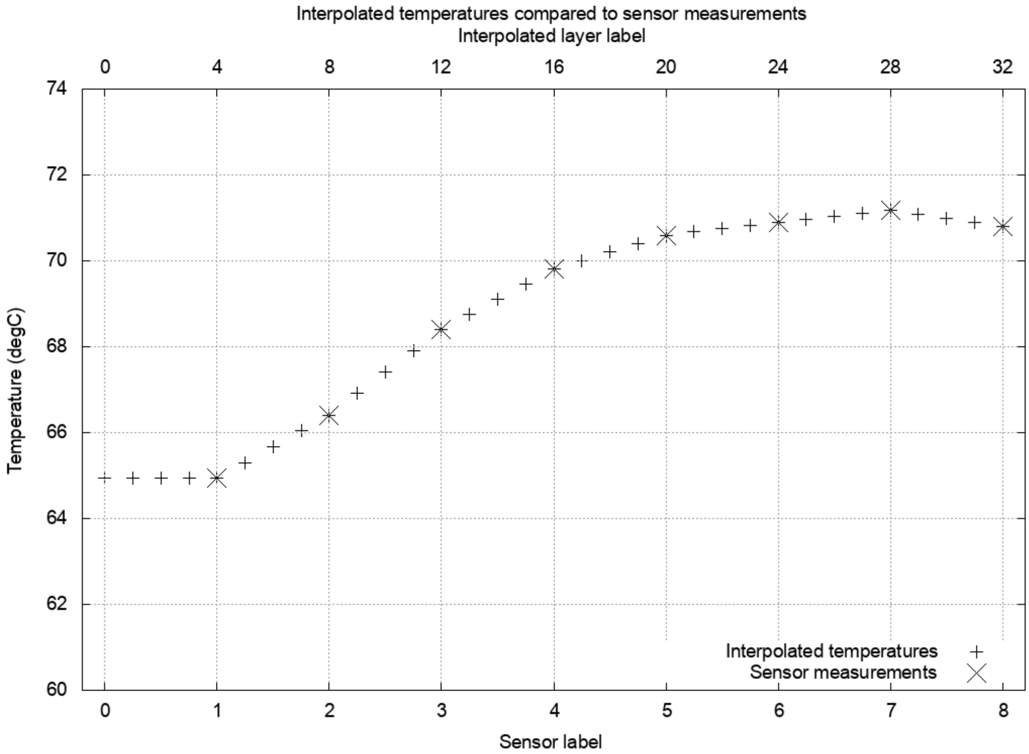

Figure C.7: Interpolation of 32 layer model to infer initial temperatures from eight sensor temperatures.

to the total number of sensors $N_{sensors}$, as shown in *Equation C.11*, resulting in a multiplication factor of 4.

$$f_m = \frac{N_{layers}}{N_{sensors}} \tag{C.11}$$

An index is determined using the ratio, w in *Equation C.12*, where b indicates the index of the interpolated layers and the range of b is $\{0; 1; 1; ...; N_{layers} - 1\}$ and w is the quotient that may result in a whole number or a number with a remainder.

$$w = \frac{b}{f_m} \tag{C.12}$$

The remainder of the quotient w is used to determine the relative location in space of the specified interpolated layer with reference to its bounding sensors. The remainder, r, is determined in *Equation C.13* where the $trunc()$ function truncates the value to the closest integer value to zero; similar to the $floor()$ function used in programming.

$$r = b - f_m trunc\left(\frac{b}{f_m}\right) \tag{C.13}$$

The interpolated temperature in a specific layer, T_b', is determined using *Equation C.14*, where the apostrophe ($'$) indicates that it is an interpolated value. The relevant gradient, g, is chosen by the integer of quotient Q with the minus one term (-1) added to account for arrays that are zero-indexed. The chosen gradient is multiplied by the decimal remainder of w, shown as $\frac{r}{f_m}$. The same index to choose the gradient g is used to choose the reference sensor temperature from T_s.

$$T_b' = g\left[trunc\left(w\right) - 1\right] \times \frac{r}{f_m} + T_s\left[trunc\left(w\right) - 1\right] \tag{C.14}$$

In this case, the first four layers take on the same temperature as Sensor 1. This is due to the lack of extra information at the boundary end. This is the method used in the current model. Other options could include using the gradient between Sensor 1 and Sensor 2 to infer the points between 0 and 1, or shift the duplicated temperature points to Sensor 8 end.

C.3 Parameter Effects

The effects of model parameters are determined using 32 layer segments.

- Insulation coefficient, (U): $\{50; 100; 150; 200\}$
- Conductive coefficient, (h): $\{50; 100; 150; 200\}$
- Upper convective coefficient, (h_h): $\{100; 500; 1000; 20000\}$
- Lower convective coefficient, (h_l): $\{50; 100; 150; 200\}$
- Mixing coefficient, (h_{mix}): $\{0; 100; 500; 1000\}$

Table C.3: Input parameter effects on model output features.

Parameter change	T_{max}	T_{min}	t_{ON_1}	**Subsequent replacement**	**Steady state**
Insulation coefficient, $U \uparrow$	No change	$\downarrow$	No change	Not discernable from ss events	Many more ss events.
Conductive coefficient, $h \uparrow$	No change	No change	No change	Moves closer to first event. Greater separation from ss events	Moves closer together.
Upper convective coefficient, $h_l \uparrow$	Upper layers decrease	$\downarrow$	$\uparrow$	$\uparrow$, move closer to first	No change.
Lower convective coefficient, $h_h \uparrow$	No change	$\downarrow$	$\downarrow$	Increases time between first and subsequent events	No change.
Mixing coefficient, $h_{mix} \uparrow$	$\downarrow$	$\downarrow$	$\downarrow$	Moves closer to first event.	No change.